Impact of the marine biological pump on atmospheric CO_2 uptake in the North Pacific: a study based on basin-wide underway measurements of oxygen/argon gas ratios and pCO_2

Deirdre E. Lockwood

A dissertation
submitted in partial fulfillment of the
requirements for the degree of

Doctor of Philosophy

University of Washington
2013

Reading Committee:
Paul D. Quay, Chair
E. Virginia Armbrust
Steven R. Emerson

Program Authorized to Offer Degree:
School of Oceanography

University of Washington

Abstract

Impact of the marine biological pump on atmospheric CO_2 uptake in the North Pacific: a study based on basin-wide underway measurements of oxygen/argon gas ratios and pCO_2

Deirdre E. Lockwood

Chair of the Supervisory Committee:
Professor Paul D. Quay
School of Oceanography

To predict how the ocean will respond to and feed back on increasing atmospheric CO_2 levels and climate change, we need excellent benchmark measurements of ocean primary productivity and organic carbon export to the deep ocean, known as the biological pump. In this dissertation, the contribution of the biological pump to atmospheric CO_2 uptake in the North Pacific was assessed through high-resolution estimates of net community productivity (*NCP*) and air-sea CO_2 flux. These parameters were determined across the North Pacific on a research cruise and repeated volunteer observation ship transits (2008–2011) by continuous measurement of surface values of the ratio of dissolved oxygen to argon (O_2/Ar) and the partial pressure of CO_2 (pCO_2). These synoptic *NCP* estimates cover a wider spatial extent at greater resolution (~4 km) than any previous shipboard basin-scale estimates in the North Pacific. A general "west high, east low" pattern is found across the basin, with the greatest annual *NCP* in western boundary provinces influenced by the Oyashio and Kuroshio currents (9.1 ± 1.7 and 7.6 ± 3.6 mol C m^{-2} yr^{-1},

respectively) and higher *NCP* in the western transition zone (4.5 ± 3.3 and 3.7 ± 1.7 mol C m^{-2} yr^{-1}) than in the eastern transition zone (2.3 ± 0.9 and 2.8 ± 1.2 mol C m^{-2} yr^{-1}). *NCP* is similar in the subarctic west and east provinces at 4.8 ± 2.1 and 4.5 ± 1.5 mol C m^{-2} yr^{-1}, respectively, in contrast with previous results showing higher *NCP* in the western subarctic gyre than in the Alaska gyre. The impact of biological carbon export and physical supply on the surface dissolved organic carbon (*DIC*) budget was determined based on the difference between climatological air-sea CO_2 flux and O_2/Ar-based estimates of *NCP*. In the western subarctic and the coastal eastern transition zone, removal of *DIC* by *NCP* over the annual cycle is nearly balanced by physical *DIC* supply, yielding a relatively small net annual air-sea CO_2 influx in these regions (0.4–0.7 mol C m^{-2} yr^{-1}). In contrast, in the open-ocean transition zone and the eastern subarctic, removal of *DIC* by annual *NCP* is ~2–3x the rate of physical supply of *DIC*, yielding substantial CO_2 influx (1.4–2.7 mol C m^{-2} yr^{-1}). Thus both biological uptake and physical supply exert significant control on annual atmospheric CO_2 uptake in the North Pacific, and both must be accurately modeled to predict ocean feedbacks on future climate change.

TABLE OF CONTENTS

LIST OF FIGURES

LIST OF TABLES

ACKNOWLEDGMENTS

I heartily thank my advisor, Paul Quay, for his guidance throughout the course of this research. His enthusiasm and energy have fired me up in pursuing challenging questions; I've learned so much from his thoughtful, creative approach to research; and his sense of humor and patience have steered me on a smooth course through graduate school. My committee members Steve Emerson, Ginger Armbrust, and Richard Feely have challenged me and given me wonderful insights. Thanks to Becky Alexander for lending her atmospheric perspective as graduate school representative.

Without Mark Haught and Johnny Stutsman, research technicians and wizards by lab and by sea, none of this work would have gotten out of port. I feel very lucky to have worked with both of them. I'm also grateful for the technical and logistical support provided by members of the Pacific Marine Environmental Laboratory at the National Oceanic and Atmospheric Administration (NOAA), including Richard Feely, Simone Alin, Geoff Lebon, Cathy Cosca, Carrie Wolfe, and Dave Wisegarver.

I thank my collaborators in this research, Hilary Palevsky, Eric Armstrong, Richard Feely, and Maria Kavanaugh. Their hard work, observations and analysis have contributed immensely to this study, and I am grateful to do such interdisciplinary, team-based research in which ideas and data are shared and discussed so readily. Past Quay lab members Laurie Juranek and Dave Munro have also helped me learn the oceanography ropes.

Thanks to the National Science Foundation (NSF), National Oceanic and Atmospheric Administration (NOAA), and the Orient Overseas Container Line (OOCL) for funding this research. I am also very grateful for funding from the NSF Graduate Research Fellowship, the NASA Space Grant Fellowship, and the Egtvedt Fellowship.

Thanks to the captains and crew of the R/V Thomas G. Thompson, and the captains, crew, and ship's agents of the M/V OOCL Tianjin and M/V OOCL Tokyo for their warm hospitality and flexibility at sea. I especially thank those on the OOCL Tianjin and Tokyo for accommodating myself and other researchers amidst the busyness of the shipping life. Thanks to Tracie Watkins Hunt and Su Tipple in UW Oceanography for helping me with myriad travel arrangements.

My parents, Peggy and Charlie Lockwood, have given me steadfast love, support and encouragement throughout my life, cheering me on in whatever I have pursued. My brother, Christopher Lockwood, and his partner, Melissa Tiedge, have also given me wholehearted love, cooked for me, and kept me laughing. My friends in UW Oceanography and beyond have been a great source of support. I especially thank Rebecca Starks and Andy Solomon and family, Jeri Helen, and Tinna Jokulsdottir. I am lucky to have such a supportive and caring family in Washington State, including Matt Distler, Becca Fishaut, Julia and Calla Distler, Elinor Distler, Phillip Ross, Tom Distler, and Phyllis MacCameron. And finally, I thank my husband, Josh Distler, who has helped me in every way imaginable.

Chapter 1

Introduction to the biological pump and atmospheric CO_2 uptake in the North Pacific

1.1 Background

Changes in global climate and ocean chemistry caused by the anthropogenic increase in atmospheric CO_2 concentration are predicted to strongly impact ocean biology and global biogeochemical cycles [Chavez *et al.*, 2011; Doney *et al*., 2009]. Photosynthesis by ocean phytoplankton underpins marine fisheries and biodiversity, and contributes about half of global net primary productivity (NPP, the rate of photosynthetic carbon fixation minus autotrophic respiration), at ~50 Pg C yr^{-1} [Falkowski *et al.*, 1998]. A portion of the carbon fixed by phytoplankton in the surface ocean sinks or is exported to the deep ocean, and this biological pump regulates the concentration of atmospheric CO_2 on geologic timescales [Ducklow et al., 2001].

The ocean is currently a net sink of atmospheric CO_2 at a rate of ~2 Pg C yr^{-1} [Takahashi *et al*., 2002, 2009]. Since the industrial revolution, the ocean has absorbed ~50% of CO_2 that humans have released into the atmosphere through fossil fuel burning and cement production (Sabine et al., 2004). However, this net sink integrates large variation in CO_2 uptake and release in both space and time [Takahashi *et al*., 2002, 2009]. Temporal and spatial variability in surface

ocean pCO_2 is controlled by the temperature-driven solubility of CO_2, the biological pump, and ocean circulation. Although the feedbacks of all three processes on the carbon cycle are predicted to change with rising atmospheric CO_2, global warming and other impacts of climate change [Doney *et al.*, 2009a], the potential impacts on the biological pump are much less well understood [McKinley *et al.*, 2006; Passow and Carlson, 2012].

Understanding the magnitude of the biological pump in the North Pacific is important because atmospheric CO_2 uptake in this region is much higher than the ocean-wide average, especially in the transition zone between the subarctic and subtropical gyres (~30–45° N) [Takahashi *et al.*, 2002, 2009; Figure 1.1]. The physical dynamics and ecology of the North Pacific are also highly responsive to interdecadal and long-term climate variability [Yoo *et al.*, 2008; Dore *et al.*, 2003]. However, global and regional biogeochemical models struggle to replicate seasonal and interannual pCO_2 variability in the North Pacific, especially in the physically dynamic northwest Pacific. They especially have difficulty representing the impact of the biological pump on air-sea CO_2 flux [McKinley *et al.*, 2006].

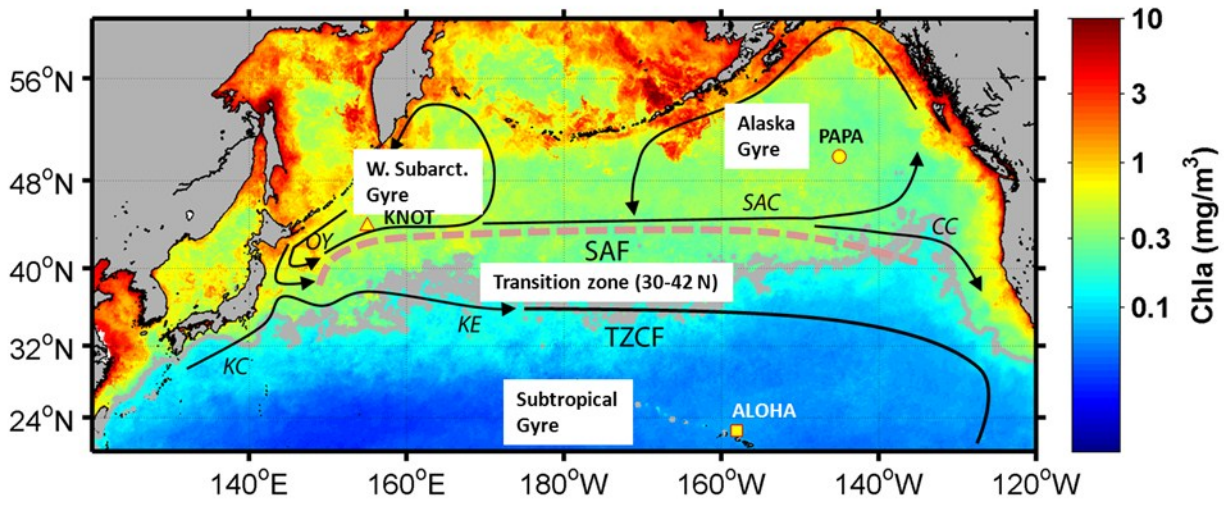

Figure 1.1: General surface circulation of North Pacific (adapted from Chierici *et al*. 2006 and Yasuda, 2003) overlain on satellite chl-a composite for 2009 (MODIS 9-km). Currents (in italics): *OY*, Oyashio Current; *KC*, Kuroshio Current; *KE*, Kuroshio Extension; *SAC*, Subarctic Current; *CC*, California Current. Regions: WSG, Western Subarctic Gyre; AG, Alaska Gyre; SAF, Subarctic Front. Yellow symbols are time series stations: KNOT, triangle; PAPA, circle; ALOHA, square. Gray outline, TZCF.

Studies using global circulation models (GCMs) predict that rising atmospheric CO_2 levels and concomitant climate change will cause a global net decrease in export production [Bopp *et al.*, 2001; Doney, 2006]. At low latitudes (tropics and subtropics), increased stratification caused by rising mean sea surface temperature (*SST*) is predicted to reduce the supply of nutrients to the euphotic zone through vertical mixing, diminishing the strength of the biological pump. In contrast, at higher latitudes, increased stratification in spring and summer is predicted to reduce light limitation on phytoplankton, yielding a longer growing season and increasing the strength of the biological pump [Bopp et al, 2001]. Increasing stratification due to warming ocean SSTs has been correlated with decreasing satellite ocean color-based estimates of *NPP* over the period 1999–2005, with the trend dominated by the subtropical gyres [Behrenfeld *et al.*, 2006]. However, Henson et al. [2010] concluded based on a comparison of satellite- and

model-based estimates of PP that a continuous 40-year record is necessary to distinguish between the effects of natural variability and long-term climate change on ocean PP.

In addition to global warming-driven effects, recent observations of ocean acidification caused by rising atmospheric CO_2 concentrations suggest that photosynthetic calcifying organisms, which form the base of the food chain in many parts of the ocean, may decline in the future [Feely *et al*., 2008; Fabry *et al.*, 2008; Doney *et al.*, 2009]. Changes in abundance of coccolithophorids, an abundant class of phytoplankton that make their shells out of calcium carbonate, would also impact the global carbon cycle, as the ratio of organic carbon to calcium carbonate in sinking particulate matter affects the efficiency of the biological pump [Broecker and Peng, 1982].

Therefore, to predict how long-term climate change will influence marine primary productivity and feed back on the global carbon cycle and climate, we need excellent benchmark measurements of the rates of ocean carbon production and export, and an improved understanding of how the biological pump impacts atmospheric CO_2 uptake. The magnitude of the ocean's biological pump is assumed to be equivalent at steady state to net community productivity (*NCP*), or gross primary productivity (*GPP*) minus community respiration. Thus, at steady state, the rate of *NCP* in the surface ocean is assumed to equal the rate of new production, or production fueled by allochthonous sources of nitrate in the euphotic zone [Eppley and Peterson, 1979] and carbon export production, the rate of organic carbon export from the surface ocean and transfer up the food chain.

Rates of *NCP*, new production, and export production in the ocean have been estimated by a variety of geochemical observational methods, including accumulation of particulate organic matter in sediment traps, mass balances of dissolved gases (O_2, Ar and N_2), NO_3, DIC,

and $\delta^{13}C\text{-}DIC$; $^{234}Th\text{-}^{238}U$ disequilibrium; and bottle incubation of O_2 and ^{15}N uptake [Ducklow *et al.*, 2001]. Global rates have also been estimated by pairing export algorithms derived from field studies [Eppley and Peterson, 1976; Laws, 2000; Dunne *et al*., 2005; Laws *et al.*, 2011] with algorithms that predict *NPP* from satellite-based observations of ocean color and temperature [Behrenfeld and Falkowski, 1997; Behrenfeld *et al.*, 2005; Westberry *et al.*, 2008]. Finally, inverse models have also been used to predict global and regional rates of *NCP* [Schlitzer 2000, 2004; Louanchi and Najjar, 2000; Lee, 2001; Yao and Schlitzer, 2013].

Global estimates of the strength of the biological pump range 8–15 Pg C yr^{-1}, or about 20% of global NPP [Emerson and Hedges, 2008], but they vary widely across ocean regions. *NCP* is negatively correlated with temperature and positively correlated with total primary productivity [Laws, 2000; Dunne *et al*., 2005; Laws *et al.*, 2011], and these trends are influenced by food web structure and nutrient supply [Falkowski *et al.*, 1998]. However, the controls on these rates are not fully established [Passow and Carlson, 2012].

Satellite observations of ocean color paired with algorithms provide unparalleled coverage of the temporal and spatial variability of global phytoplankton biomass, NPP, and NCP [Falkowski *et al*., 1998, McClain et al., 2009]. However, current algorithms predicting depth-integrated NPP from remotely sensed data have been shown to agree only within a factor of two [Carr *et al*., 2006].

To improve the current generation of satellite PP algorithms, we need better groundtruthing of ocean primary productivity on many temporal and spatial scales. In the North Pacific, we have excellent long-term estimates of ocean NPP, NCP and other biogeochemical indices at ocean time series stations PAPA (OSP, 50° N, 145° W) and KNOT (44° N, 155° E) in the northeastern and northwestern subarctic, respectively, and at station ALOHA (22° 45 N, 158°

W) in the subtropical North Pacific (Figure 1.1). However, apart from surveys of the basin by volunteer observation ship [Wong *et al*., 2002; Chierici *et al*., 2006] and satellite-based analyses of nitrate drawdown [Goes *et al.*, 2004, 2004a], there have been few basin-scale, synoptic surveys of *NCP*, so it is unclear how representative these time series are of the basin. To validate synoptic, basin-scale estimates of NCP derived from satellite studies, we need observations that cover large spatial areas on roughly the same time scale as these estimates.

In this dissertation, a high-resolution underway method is applied to determine *NCP in situ* by measuring the the ratio of dissolved O_2 and Ar gases (O_2/Ar) in the surface ocean. The saturation level of the O_2/Ar gas ratio in the mixed layer coupled with air-sea gas exchange rate yields quantitative estimates of NCP (Emerson *et al.*, 1991) that are insensitive to nonbiological gas saturation processes (e.g., warming, bubble injection) because argon is an inert analog of oxygen. The *O_2/Ar*-based estimate of *NCP* integrates over the residence time of oxygen in the mixed layer, on average ~2 weeks in the North Pacific. Thus, it has the potential to capture intermittent, high-productivity events that can be missed by incubation studies, and provides comparable temporal coverage to satellite-based estimates of carbon export.

Recently, continuous underway measurements of *O_2/Ar* using equilibrator inlet mass spectrometry [EIMS; Tortell, 2005; Kaiser *et al*., 2005; Cassar *et al*., 2009] and of *p*CO_2 [Pierrot *et al*., 2009], combined with a wind speed parameterization of gas transfer velocity, have made it possible to make synoptic, basin-scale estimates of *NCP* and air-sea CO_2 flux at kilometer-scale resolution [e.g., Nemcek *et al*. 2008; Guéguen and Tortell, 2008; Stanley *et al*., 2010; Cassar *et al.*, 2011]. Together with collaborators, I used these underway techniques to continuously measure O_2/Ar and pCO_2 on a research cruise and repeated volunteer observation ship crossings of the North Pacific. These *NCP* estimates cover a wider spatial extent at greater resolution (~4

km) than any previous shipboard basin-scale estimates in the North Pacific. The objectives of this study were (i) to determine spatial and temporal (regional and seasonal) variability in rates of *NCP* and CO_2 flux across the North Pacific basin; (ii) to compare these estimates with previous field and model-based estimates in the region; and (iii) to use oxygen and carbon budgets to estimate the influence of *NCP* on CO_2 flux in this region.

1.2 Overview of research

In Chapter 2, I report high-resolution estimates of NCP and CO_2 flux in the subarctic, transition zone, and subtropical Northeast Pacific derived from underway measurements of O_2/Ar and pCO_2 during a research cruise in August 2008. I compare these estimates to simultaneous underway measurements of chlorophyll and discrete flow cytometric estimates of phytoplankton composition. I determine the correlation of NCP with CO_2 flux and with the abundance of different size classes of phytoplankton. Chapter 2 has already been published in the form presented here [Lockwood *et al.*, 2012].

In this study, *NCP* and CO_2 influx were greatest in the subarctic (45–50° N, 25.8 ± 4.6 and 4.1 ± 0.9 mmol C m^{-2} d^{-1}) and northern transition zone (40–45° N, 17.1 ± 4.4 and 2.1 ± 0.5 mmol C m^{-2} d^{-1}), with mean *NCP* ~6–8x greater than mean CO_2 invasion (error estimates reflect 1 σ confidence intervals). Contrastingly, the southern transition zone (32–40° N) and subtropics (22–32° N) had lower mean *NCP* (5.4 ± 1.8 and 8.1 ± 2.1 mmol C m^{-2} d^{-1}, respectively) and mean CO_2 efflux (3.0 ± 0.5 and 0.1 ± 0.0 mmol C m^{-2} d^{-1}, respectively). In the subarctic and transition zone, *NCP* was highly correlated with surface *chl-a* and CO_2 influx, indicating strong coupling between the biological pump and CO_2 uptake. Meridional trends in our *NCP* estimates in the transition zone and subtropics were similar to those for integrated summertime *NCP* along

the cruise track determined using an upper ocean climatological carbon budget. In the transition zone, we detected high zonal and meridional variability in *NCP* and CO_2 *flux* at <5-km scales, suggesting the impact of frontal dynamics on biogeochemical fluxes in this region, and the need for observations throughout the year to determine its mean annual state.

NCP and CO_2 influx were highly correlated in the subarctic and transition zone with a slope of 2 to 3, indicating the strong coupling between biological uptake and CO_2 influx during summertime in these regions. *NCP* in these regions was also highly correlated with concentrations of microphytoplankton. In contrast, *NCP* and CO_2 influx were not strongly coupled in the subtropics, suggesting that the temperature effect on solubility dominates CO_2 flux during summertime there. In the subtropics, *NCP* was uncorrelated with microphytoplankton and weakly correlated with picophytoplankton.

In Chapter 3, I describe work to estimate NCP and air-sea CO_2 flux using continuous underway measurements of O_2/Ar and pCO_2 on 13 cross-Pacific transits across the North Pacific subarctic and transition zone via volunteer observation ship. I then present a composite annual cycle of NCP in seven provinces of the North Pacific determined using a mixed layer O_2/Ar budget approach that accounts for impacts of horizontal advective transport and vertical entrainment and diffusive mixing. After determining annual NCP in these provinces, I analyze its impact on air-sea CO_2 flux by comparing *NCP* estimates with climatological surface pCO_2. Chapter 3 will be submitted for future publication in a similar form to that presented here.

In this study, I generally found a "west high, east low" pattern of *NCP* across the basin, with the greatest annual *NCP* in the western boundary provinces influenced by the Oyashio and Kuroshio currents (9.1 ± 1.7 and 7.6 ± 3.6 mol C m^{-2} yr^{-1}, respectively) and higher *NCP* in the western transition zone provinces (4.5 ± 3.3 and 3.7 ± 1.7 mol C m^{-2} yr^{-1}) than in the eastern

transition zone provinces (2.3 ± 0.9 and 2.8 ± 1.2 mol C m^{-2} yr^{-1}). *NCP* was similar in the subarctic west and east provinces at 4.8 ± 2.1 and 4.5 ± 1.5 mol C m^{-2} yr^{-1}, respectively, in contrast with previous results showing higher NCP in the Western Subarctic Gyre than in the Alaska Gyre (mainly based on comparison of data from KNOT and OSP).

In provinces with high spatial variability in *NCP*, the Oyashio, Kuroshio, transition zone west, and subarctic east, the *NCP* estimates are 1.5–2x greater than the mean of previous results in the respective regions. This may reflect the ability of the continuous O_2/Ar method to capture intermittent, high-productivity events that could have been missed by previous estimates, most of which are based on discrete snapshots with lower spatial resolution. However, results in the eastern transition zone, where NCP is less spatially variable, were similar to previous results in these regions and at subtropical station ALOHA.

These annual *NCP* estimates based on O_2/Ar measurements were compared with climatological net annual air-sea CO_2 flux to determine (as the residual) net annual supply of *DIC* due to physical processes (F_{physDIC}) in each province. In the western subarctic and the eastern coastal transition zone, removal of *DIC* by *NCP* over the annual cycle is nearly balanced by supply of F_{physDIC} (mainly in winter, most likely due to vertical diffusive mixing and entrainment). The near balance of physical DIC supply and organic carbon export leads to a relatively small net annual CO_2 influx in these regions (0.4–0.7 mol C m^{-2} yr^{-1}). In contrast, in the open ocean transition zone and eastern subarctic, removal of *DIC* by annual *NCP* was 2–3x the rate of supply by F_{physDIC}, leading to substantial CO_2 influx (1.4–2.6 mol C m^{-2} yr^{-1}). These results suggest that the high CO_2 uptake in the North Pacific transition zone is controlled, as has recently been proposed by Ayers and Lozier [2012], by a combination of high biological uptake and lower net physical supply of *DIC* than that in the subarctic.

Chapter 2

High-resolution estimates of net community production and air-sea CO_2 flux in the Northeast Pacific

2.1 Introduction

Surface CO_2 measurements yield a mean global net ocean sink for atmospheric CO_2 of ~2 Pg C yr^{-1}, however there is large variation in oceanic CO_2 uptake and release in both space and time [*Takahashi et al.*, 2009] that is controlled by biological drawdown through primary productivity (*PP*) and export to the deep ocean (the biological pump), temperature-driven solubility of CO_2 (the solubility pump) and ocean circulation. The biological pump has been estimated to export organic carbon globally at 8–15 Pg C yr^{-1} [*Emerson and Hedges, 2008*], but these rates are poorly constrained and vary widely across ocean regions [*Boyd and Trull*, 2007; *Schlitzer*, 2000, 2004]. To predict the response of this sink to future changes in Earth's climate, we must understand how the biological and solubility pumps vary spatially, seasonally and interannually, and what factors determine this variability.

A remarkable feature in the surface CO_2 of the North Pacific is the band of strong mean annual air-sea CO_2 uptake (2–9 mol C m^{-2} yr^{-1}) at ~30–45º N, roughly corresponding to the transition zone between the subtropical and subarctic gyres along the path of the Kuroshio

current and extension [*Takahashi* et al., 2009]. Two prominent basin-wide oceanographic features occupy this region: (1) the physically defined North Pacific transition zone (~30–45º N), a region of confluence and convergence bounded by temperature and salinity fronts [*Roden*, 1991], and (2) the transition zone chlorophyll front (TZCF), a biological hotspot defined by the 0.2 mg m^{-3} chlorophyll isopleth that seasonally migrates from 30–35º N in winter to 40–45º N in summer [*Polovina* et al., 2001].

Given the biological prominence of the TZCF and the enhanced *PP* found at similar convergent fronts [*Longhurst*, 2007; *Mann and Lazier*, 2006], one would expect that *PP* and carbon export contribute substantially to the strong CO_2 uptake in this region, but the magnitude of this contribution is unclear. *Takahashi et al.* [2002, 2009] attribute the sink to the combined effects of the solubility and biological pumps. In contrast, *Ayers and Lozier* [2012] recently modeled CO_2 uptake in the transition zone and concluded that although temperature-driven solubility strongly affects seasonal pCO_2 trends, it controls only ~17% of the annual sink in this region, with the remainder contributed by biological export and geostrophic divergence of DIC.

In this study, we sought to estimate the contribution of the biological pump to carbon uptake in the North Pacific by making high-resolution estimates of carbon export and uptake. The strength of the biological pump is quantified by estimates of *NCP*, which equals gross *PP* (*GPP*) minus community respiration and is equivalent at steady state to the rate of organic carbon export and transfer up the food chain. In the North Pacific, *NCP* is fairly well constrained at two time series stations, Ocean Station P (OSP) in the subarctic NE Pacific (50º N, 145º W) and Station ALOHA in the subtropical NE Pacific (22º 45 N, 158º W) through surface layer budgets of dissolved gases, nutrients, *DIC* and $\delta^{13}C$, and through in situ dissolved gas ratios and ^{234}Th-^{238}U disequilibrium (see Table 2.1). But because there are comparatively fewer estimates

in the rest of the basin and only a few snapshot *NCP* estimates for the transition zone [*Wong et al*., 2002; *Juranek*, 2007; *Howard et al*., 2010; *Juranek et al*., 2012], it is unclear how representative these sites are of the basin as a whole. On a basin-wide scale, *NCP* estimated from climatological seasonal *DIC* drawdown [*Lee et al*., 2001] is high (2–6 mol C m^{-2} yr^{-1}) in the transition zone.

In recent years, fine-scale observations of oceanographic parameters made possible by continuous underway measurements have allowed researchers to better determine rates and controls on ocean biogeochemical processes, including *NCP*. In particular, continuous measurements of the dissolved gases O_2 and Ar using equilibrator inlet mass spectrometry (EIMS) [*Tortell*, 2005; *Kaiser et al.*, 2005; *Cassar et al.*, 2009], combined with a wind speed parameterization of gas exchange, have led to continuous, kilometer-scale estimates of *NCP* [e.g., *Nemcek et al*. 2008, *Guéguen and Tortell*, 2008; *Stanley et al.*, 2010; *Cassar et al.*, 2011].

In this study, we continuously measured surface ocean O_2/Ar, pCO_2 and chl-a and carried out discrete flow cytometry in the subarctic, transition zone and subtropical Northeast Pacific to determine the heterogeneity in the rates of the biological pump and air-sea *CO_2 flux* on a cruise (August–September 2008) that crossed the transition zone three times (Figure 2.1). We compare these results with previous *NCP* estimates at OSP and Station ALOHA and surface CO_2 climatology, and examine the influence of *NCP* on CO_2 uptake in the region.

Table 2.1: Upper ocean NCP in NE Pacific subarctic, transition and subtropical regions

	Annual NCP (mol C m^{-2} yr^{-1})	Daily NCP (mmol C m^{-2} d^{-1})
Subarctic		
OSP	**2.0 ± 0.3** 2.1[a], 1.8[b], 2.1[c], 1.6[d], 2.5[e]	**14 ± 5** 12[a], 8[b], 15[c], 10[d], 17[e], 21[f]
Alaska Gyre (~50–55° N)	3.1[g]	18[g]
Subarctic current (~45–50° N)	2.6[g]	15[g], 25.8 ± 4.6*
Subtropics		
Station ALOHA	**2.7 ± 0.9** 2.7[h], 1.7[i], 4.3[j], 2.4[k], 2.7[l], 2.3[m]	**8 ± 4** 7[h], 5[i], 12[j], 3[k], 7[l], 6[m], 15[n]
20–25º N	2.4[o]	
145–152º W, 22–32° N		8.1 ± 2.1*
Transition zone		
All		**9 ± 5** (8; 3)[q], (21; 13)[r], 11.8 ± 3.2*
Northern (40–45° N)	2.6[p]	15[p], 17.1 ± 4.4*
Southern (32–40° N)	0.9[p]	14[p], 5.4 ± 1.8*

See footnotes for seasonality of daily estimates. Bold values are mean ± s.d. of previous observations cited below. *This study (mean ± s.d.). **Subarctic studies** (mixed layer): [a]*Wong et al*. [2002a], NO_3 mass balance. [b]*Charette et al*. [1999], ^{234}Th-^{238}U disequilibrium and Th/C ratio. [c]*Emerson* [1987], O_2 mass balance. [d]*Emerson* [1991], O_2, Ar and N_2 mass balance. [e]*Emerson and Stump* [2010], in situ O_2 and N_2 mass balance. [f]*Wheeler* [1993], 4-month NO_3 drawdown and $^{15}NO_3$ assimilation. [g]*Wong et al*. [2002]; NO_3 mass balance. *Seasonality of daily estimates*: [a]Daily average over 6 months. [b]August. [g]Daily average over summer NO_3 drawdown (time period varies, defined by NO_3 max – NO_3 min). **Subtropical studies** (euphotic zone or mixed layer designated): [h]*Emerson et al*. [1997], O_2 euphotic zone mass balance. [i]*Hamme and Emerson* [2006], O_2 euphotic zone mass balance. [j]*Emerson et al*. [2008], O_2 euphotic zone mass balance. [k]*Benitez-Nelson et al*. [2001]; ^{234}Th deficiency over 0–150 m, includes total C output. [l]*Quay and Stutsman* [2003], DIC-δ^{13}C mixed layer mass balance. [m]*Keeling et al*. [2004], δ^{13}C-DIC mixed layer mass balance. [n]*Juranek and Quay* [2005], in situ mixed layer O_2/Ar. [o]*Quay et al*. [2009], DIC-δ^{13}C mixed layer mass balance. Seasonality of daily estimates: [h–j,m]Daily average over 12 months. [k]August steady-state POC export rate. [l]Summer average. [n]August. **Transition zone studies** (euphotic zone or mixed layer designated): [p]*Wong et al*. [2002]; NO_3 mixed layer mass balance. [q]*Howard et al.* [2010], euphotic zone O_2/Ar (summer, fall). [r]*Juranek et al*. [2012], mixed layer O_2/Ar (spring, summer).

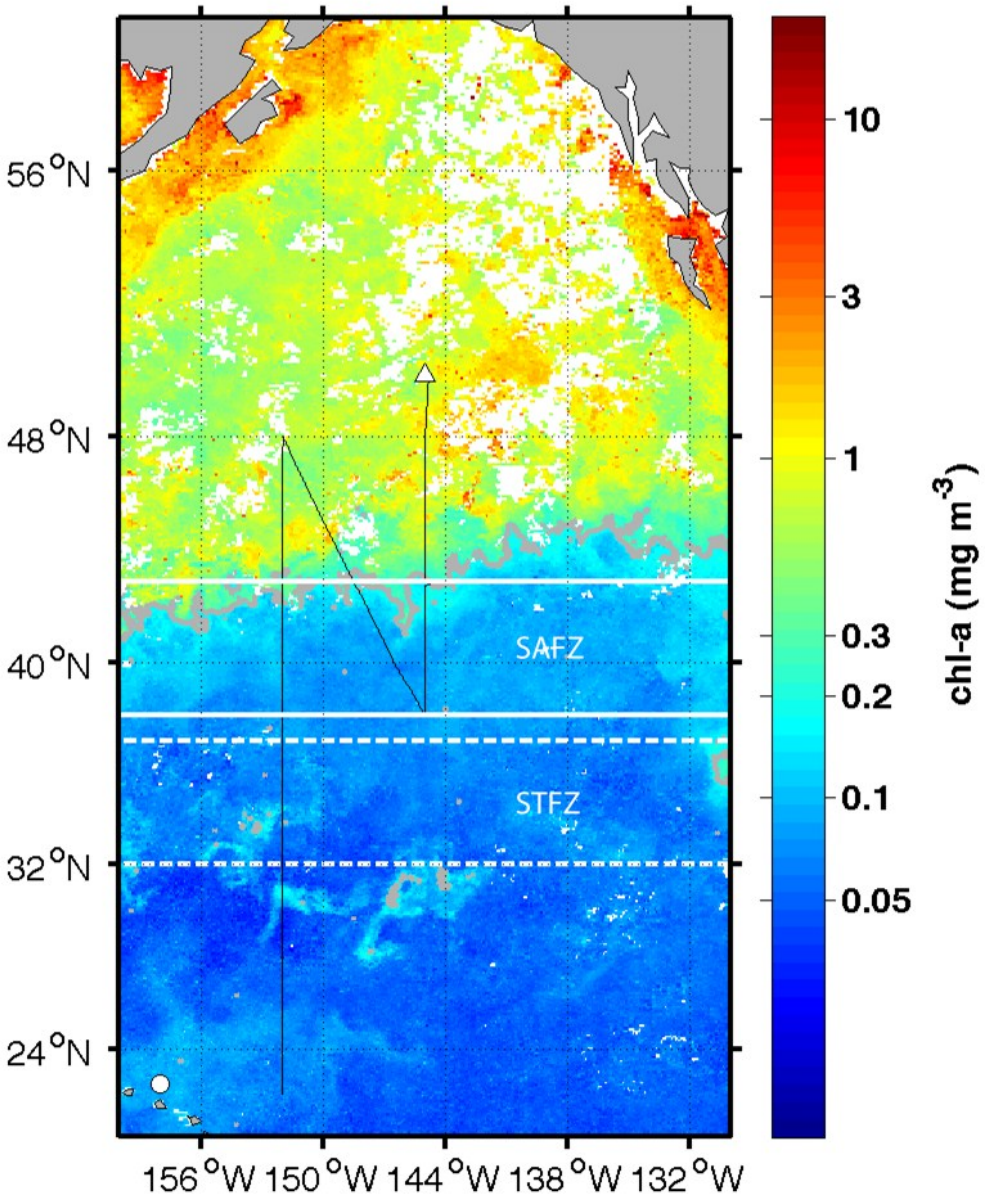

Figure 2.1: Cruise track (black) overlain on SeaWiFS 9-km monthly average chl-a for September 2008. White triangle, Station P; white circle, Station ALOHA. TZCF is highlighted in grey. Solid white lines bound SAFZ; dashed white lines bound STFZ.

2.2 Background

2.2.1 Setting

The main circulation features of the Northeast Pacific are the cyclonic subarctic gyre centered in the Gulf of Alaska (~45–60º N, 160–135º W), the anticyclonic subtropical gyre (~15–35º N, 135 E–135º W), and the transition zone between the two. In the subarctic Alaska gyre, a halocline limits winter mixed layer depths to ~90–120 m and strong seasonal variation in temperature and wind speed leads to stratification in summer, with mixed layers shoaling to ~40 m [*Harrison et al.*, 2004]. In this high nitrate, low chlorophyll (HNLC) region, iron generally limits the growth of large microphytoplankton like diatoms [*Harrison et al*., 1999; *Boyd et al*., 1996], and the phytoplankton community is dominated by small cells <5 μm.

The subtropical gyre is a low-nutrient, low-chlorophyll region with lower seasonal variability in temperature, wind speed, productivity and light than in the subarctic gyre; mixed layer depth ranges from 40 m in summer to 100 m in winter [*Karl et al.*, 1999; *Keeling et al*., 2004]. *Prochlorococcus* is the dominant photoautotroph, but N_2 fixation by other cyanobacteria may provide up to half the nitrogen responsible for export [*Karl et al.*, 1997, 2001].

Between these two gyres, the North Pacific transition zone extends across the basin at ~30–45º N. Confluence of the Kuroshio and Oyashio currents and Ekman convergence set up two frontal regions with strong meridional gradients in temperature and salinity in winter and salinity in summer, the subarctic frontal zone (SAFZ, defined by 33–33.8‰ isohalines, ~40–43º N) and the subtropical frontal zone (STFZ, defined by 34.8–35.2‰ isohalines, ~31–34º N; *Roden*, 1991] (Figure 2.1). On shorter timescales, these frontal zones are associated with highly temporally and spatially variable mesoscale perturbations including meandering fronts, jets and eddies [*Roden*, 1991; *Yuan and Talley*, 1996].

2.2.2 Previous estimates of NCP in the Northeast Pacific

In the Northeast Pacific, most of our understanding of rates of net community productivity (*NCP*) comes from numerous studies at OSP in the subarctic gyre and Station ALOHA in the subtropical gyre, including mass balances of dissolved gases (O_2, Ar and N_2; *Emerson*, 1987; *Emerson et al.*, 1997, 1991; *Hamme and Emerson*, 2006; *Emerson and Stump*, 2010], NO_3 [*Wong et al.*, 2002a] and DIC-$\delta^{13}C$ [*Quay and Stutsman*, 2003; *Keeling et al.*, 2004; *Quay et al.*, 2009]; the in situ O_2/Ar method [*Juranek and Quay*, 2005; *Quay et al.*, 2010], and the ^{234}Th method [*Charette et al.*, 1999; *Benitez-Nelson et al.*, 2001].

Notably, despite different limitations to biological productivity at these two sites, annual *NCP* is similar at 2.0 ± 0.3 mol C m^{-2} yr^{-1} at OSP and 2.7 ± 0.9 mol C m^{-2} yr^{-1} at ALOHA (mean ± s.d. of multiple estimates), within the ±50% uncertainty of the measurements (Table 2.1) [*Emerson et al.*, 2008]. However, at OSP, *NCP* is primarily confined to spring and summer at high daily rates (14 ± 5 mmol C m^{-2} d^{-1}), whereas at ALOHA, daily rates are lower (8 ± 4 mmol C m^{-2} d^{-1}) but *NCP* takes place throughout the year (mean ± s.d. of multiple studies, Table 2.1).

Few studies have examined *NCP* in the transition zone. *Wong et al.* [2002] estimated *NCP* at 2.6 mol C m^{-2} yr^{-1} and 0.9 mol C m^{-2} yr^{-1} based on seasonal NO_3 drawdown in two regions (40–45° N and 35–40° N, respectively). Summertime daily *NCP* for these two provinces was equal at 14–15 mmol C m^{-2} d^{-1}, but the southern region had a much shorter export season. *Juranek* [2007] and *Juranek et al*. [2012] estimated daily *NCP* in the transition zone mixed layer (~32–42º N) of 21 and 13 mmol C m^{-2} d^{-1} in spring and summer, respectively, and *Howard et al*.

[2010] (30–45° N) estimated rates of 8 mmol C m^{-2} d^{-1} in summer and 3 mmol C m^{-2} d^{-1} in fall, based on O_2/Ar measurements (Table 2.1).

2.2.3 O_2/Ar method for estimating NCP

The saturation level of the O_2/Ar gas ratio in the mixed layer coupled with air-sea gas exchange rate yields quantitative estimates of *NCP* that are mostly insensitive to nonbiological gas saturation processes (e.g., warming, bubble injection) because argon is an inert analog of oxygen, as described previously [*Craig and Hayward*, 1987 and *Emerson et al.*, 1991, 1997].

Briefly, the biological O_2 supersaturation, which quantifies the influence of *NCP* on the O_2 budget, is defined as:

$$\frac{\Delta O_2}{Ar} = \frac{\left[\frac{O_2}{Ar}\right]_{\mathrm{msr}}}{\left[\frac{O_2}{Ar}\right]_{\mathrm{sat}}} - 1 \qquad (2.1)$$

where $[O_2/Ar]_{\mathrm{msr}}$ is the measured dissolved O_2/Ar gas ratio, and $[O_2/Ar]_{\mathrm{sat}}$ is the ratio expected at saturation with air (based on temperature and salinity dependence of O_2 and Ar solubility; *Garcia and Gordon*, 1992; *Hamme and Emerson*, 2004]. The percent biological O_2 supersaturation ($\%O_{2bio}$) equals ($\Delta O_2/Ar$)*100.

NCP is calculated using O_2 and Ar mass balances for the mixed layer, typically assuming steady state and negligible physical supply, yielding:

$$NCP = k_{\mathrm{O2}}[O_2]_{\mathrm{sat}}\frac{\Delta O_2}{Ar} \qquad (2.2)$$

where k_{O2} is the gas transfer velocity of O_2 (m d^{-1}) and $[O_2]_{\mathrm{sat}}$ is the concentration of O_2 at saturation (mol m^{-3}) [*Garcia and Gordon*, 1992]. We determined k_{O2} using winds from QuikScat, the *Ho et al*. [2006] wind speed parameterization using a 60-day time-weighting technique [*Reuer et al.*, 2007], and the temperature- and salinity-dependent Schmidt number

[*Wanninkhof*, 1992]. To convert O_2-based *NCP* to C-based *NCP*, we used a ratio of 1.4 O_2: 1 C (export or new production) [*Laws et al.*, 1991]. This estimate of *NCP* integrates over the residence time of O_2 in the mixed layer (i.e., (mixed layer depth)/k_{O2}), which was 8–14 days. The strong vertical stratification and low winds observed during the cruise favored a negligible impact of vertical mixing on the mixed layer O_2 budget.

2.3 Methods

2.3.1 Underway and discrete sampling and cruise track

We continuously measured surface O_2/Ar, pCO_2, temperature, salinity and fluorescence from the underway system of the R/V Thompson (at ~5 m intake) on a cruise between Station P and Honolulu, Hawaii (30 August–15 September 2008; Figure 2.1). Temperature and salinity were measured using the ship's TSG. Underway chl-a was estimated based on continuous fluorometer measurements calibrated with discrete chl-a samples measured using standard methods on a shipboard Turner fluorometer [*Strickland and Parsons*, 1972]. Mixed layer depth was determined using CTD profiles along the ship's cruise track at a resolution of ~1–2° latitude as a density increase of 0.125 kg m^{-3} from the surface value. Concentrations of nitrate, phosphate and silicate were determined on discrete surface samples collected by Niskin using a shipboard autoanalyzer (Technicon AutoAnalyzer II) and standard methods [*UNESCO*, 1994].

2.3.2 Continuous O_2/Ar measurements using EIMS

We continuously measured surface O_2/Ar using an EIMS system similar to that described in *Cassar et al.* [2009]. Water from the ship's underway line was pumped at ~2 L min^{-1} through a coarse filter to screen out particulates into a 1 L graduated cylinder on which the equilibrator

cartridge (Membrana MicroModule G569, 0.75" x 1") was mounted. Water from the graduated cylinder was pumped through a 5 μm filter sock sewed inside a 100 μm filter sock (1.5" x 12", McMaster-Carr), and then through the cartridge at ~100 ml min^{-1}. To prevent biofouling, the coarse filter was cleaned and the sock filter was replaced daily, and the equilibrator cartridge was replaced weekly. All tubing used was Tygon silver (antimicrobial).

Headspace gas from the equilibrator was delivered through an 0.05 mm fused silica capillary to the quadrupole mass spectrometer (Pfeiffer Prisma QMS), which was kept at a constant temperature (40° ± 2° C). Individual ion currents (O_2, Ar) were measured at 1-second intervals, and the ratio of O_2/Ar currents was averaged to a 10-minute timescale. The EIMS system e-folding response time is 7 min [*Cassar et al*., 2009], yielding a spatial resolution of ~2 km at the average ship speed of 10 knots.

EIMS-based O_2/Ar measurements were calibrated using the O_2/Ar of air measured by the EIMS, and O_2/Ar measured by isotope ratio mass spectrometer (IR-MS) on discrete samples collected from either the underway line or surface (5 m) Niskin bottles approximately every 6–8 hours following the collection procedures of *Emerson et al.* [1995] and mass spectrometer procedures of *Juranek and Quay* [2005] in the University of Washington Stable Isotope Lab. The percent error ([s.d./mean]*100) in O_2/Ar of discrete air standards used for IR-MS calibration was 0.2% and that of duplicate samples was 0.1%. The O_2/Ar of discrete samples measured simultaneously on the ship's underway line and from surface Niskins compared well (0.1% error), showing no evidence of O_2 consumption in the underway line.

We estimated error in *NCP* using a Monte-Carlo approach assigning uncertainty in the following terms: kO_2 ± 15% (twice the spread in k_{O2} values predicted by three parameterizations recently validated by *Ho et al.* [2011]: *Nightingale et al.* [2000], *Ho et al.* [2006], and *Sweeney et*

al. [2007]) and $O_2/Ar \pm 0.06$ (s.d. of mean in offset between EIMS and discrete samples). Mean *NCP* percentage error ([s.d./mean]*100) was 18% in the subarctic, 27% in the transition zone and 25% in the subtropics.

2.3.3 Measurements of pCO_2 and estimate of CO_2 flux

We continuously measured the pCO_2 in surface water from the ship's underway line and air from the bow with an automated IR-detection-based underway pCO_2 measuring system that has been described in detail elsewhere [*Feely et al*., 1998; *Pierrot et al*., 2009]. We calculated the air-sea pCO_2 gradient (ΔpCO_2) as $\Delta pCO_2 = pCO_{2SW} - pCO_{2atm}$, where pCO_{2SW} is the calculated pCO_2 of the seawater (after correction for water temperature difference between in situ and the pCO_2 equilibrator) and pCO_{2atm} is the measured atmospheric pCO_2. After correction, the accuracy of the data is within 0.1 μatm for pCO_{2atm} and 2 μatm for pCO_{2SW} [*Pierrot et al.*, 2009], and the equilibrator integration time is 30–45 s. pCO_2 data were averaged to match the 10-minute integration time of the EIMS data.

The air-sea flux of CO_2 is calculated based on ΔpCO_2 and the solubility (k_H) [*Stumm and Morgan*, 1996] and gas transfer velocity of CO_2 (k_{CO2}):

$$CO_2\ flux = k_{CO2}\, k_H\, \Delta pCO_2 \qquad (2.3)$$

Defined in this way, *CO_2 flux* from the atmosphere into the ocean (influx) is negative, and efflux is positive. k_{CO2} was calculated as described above for k_{O2} using the Ho *et al.* [2006] wind speed parameterization with time-weighting [*Reuer et al.*, 2007], and the Schmidt number for CO_2 [*Wanninkhof*, 1992].

2.3.4 Flow cytometry measurements

Cell counts of phytoplankton groups were collected from the flow-through system of the R/V Thompson at various intervals along the ship track or from surface (5 m) Niskins. Samples were preserved in liquid nitrogen and processed later in the lab. Cells were enumerated and classified using a FACS-Caliber flow cytometer [*Sherr et al.*, 2003]. Following the protocol of *Sherr et al*. [2003], prokaryotes were stained with SYBR-green; *Prochlorococcus* counts were subtracted from heterotrophic bacteria counts. We binned data into microphytoplankton (10–60 μm), nanophytoplankton (2–10 μm) and picophytoplankton (1–2 μm); the picophytoplankton fraction was dominated by *Synechococcus* north of the TZCF and *Prochlorococcus* south of it.

2.3.5 Climatological pCO_2, CO_2 flux, alkalinity and DIC

We used a recent climatological surface pCO_2 data set [*Takahashi et al.*, 2009] to compare our pCO_2 measurements with the seasonal cycle of pCO_2 and DIC over our cruise track (section 2.5.3). This data set includes monthly pCO_{2SW}, pCO_{2atm}, SST, salinity and wind speed data at resolution of 4° latitude by 5° longitude, with pCO_2 data normalized to reference year 2000. We calculated climatological monthly *CO_2 flux* using the climatological pCO_{2SW}, pCO_{2atm}, temperature, salinity, wind speed and *Ho et al*. [2006] parameterization of gas transfer velocity and compared it to our continuous *CO_2 flux* estimates in September 2008 (normalized to year 2000).

To estimate the seasonal climatological *DIC* cycle for the region covered on our cruise, we used the climatological temperature and salinity data to calculate monthly alkalinity with the latitude-dependent parameterization of *Lee et al*. [2006], and used these alkalinity values and pCO_2 to calculate monthly *DIC* with the program CO2sys [*Lewis and Wallace*, 1998]. We used

monthly climatological mixed layer depth from *Monterey and Levitus* [1997] at 1° resolution, bin-averaged to the 4° latitude x 5° longitude boxes of the *Takahashi et al.* [2009] data set.

2.4 Results

2.4.1 Regional setting

We categorize our results into three regions: the subarctic (45–50° N), transition zone (32–45° N) and subtropics (22–32° N). Sea surface temperature and salinity generally increased and density decreased from the subarctic to the subtropical gyre, with a local density minimum at ~35° N within the transition zone (Figure 2.2). The strong gradients in surface salinity (and weaker SST gradients) of the SAFZ and STFZ are apparent (Figure 2.2) at ~38–43° N, and ~32–37° N, respectively, extending slightly farther than their climatological positions (40–43° N and 31–34° N, respectively). The strongest surface density gradients were in the northern transition zone (40–45° N) and subtropics (22–24° N) (Figure 2.2). The TZCF (location of the 0.2 mg m^{-3} chl-a isopleth) ranged from 42° to 44° N within the northern transition zone (Figure 2.3), consistent with its climatological late summer position (40–45° N) [*Polovina et al.*, 2001].

Mixed layer was relatively shallow, reflecting late summer conditions; mean depths decreased from 32 m in the subarctic to a local minimum (26 m) in the transition zone, and then increased to 51 m in the subtropics (Figure 2.2). k_{O2} was fairly low (3–5 m d^{-1}), and was highest in the subarctic and northern transition and lowest in the southern transition zone (Figure 2.3). Due to variation in mixed layer depth and k_{O2}, the O_2 residence time in the surface layer increased southward from a mean of 8 days in the subarctic and transition to 14 days in the subtropics.

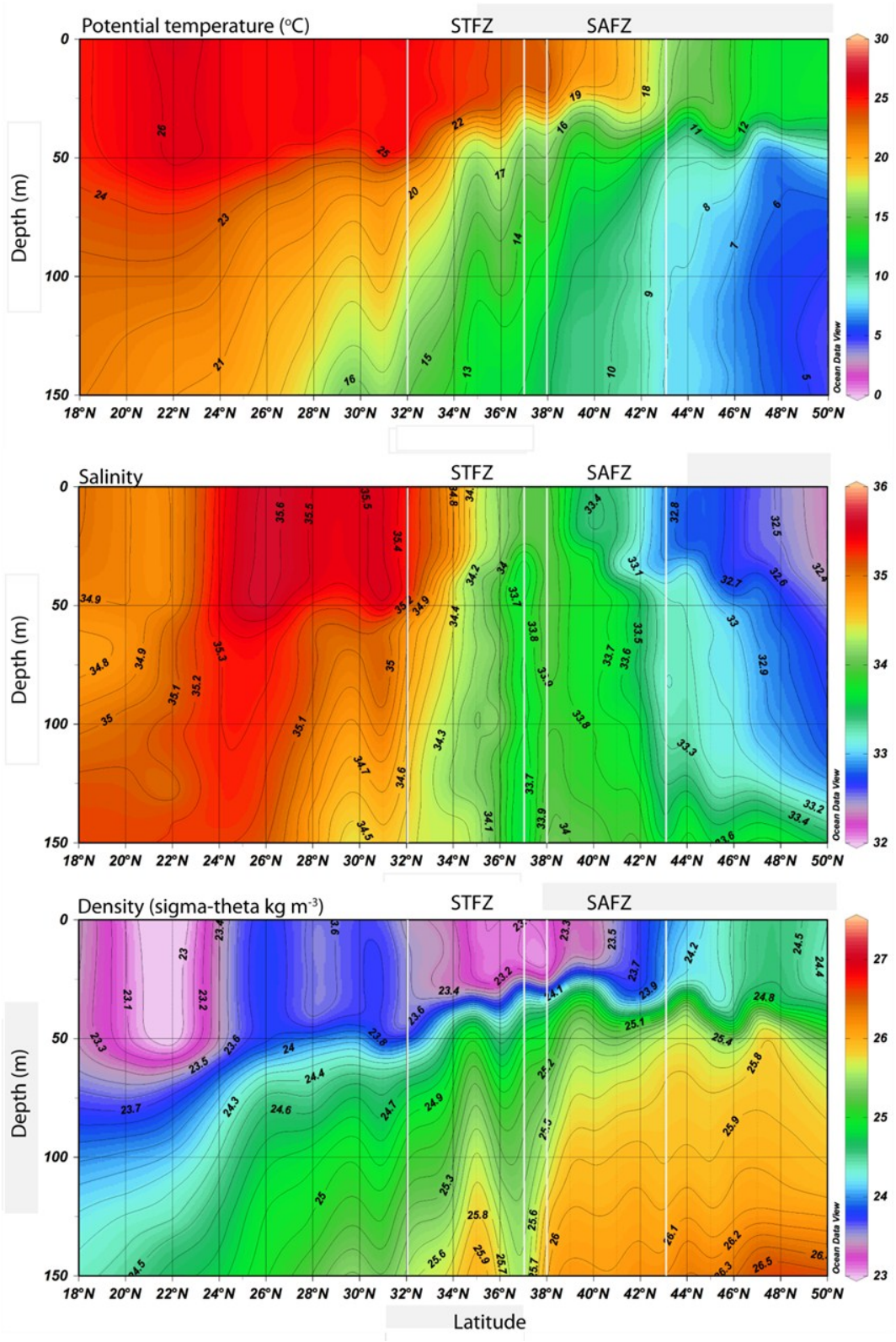

Figure 2.2: Depth sections of potential temperature, salinity and potential density (σ_θ) measured on cruise along 152º W. The SAFZ and STFZ are bounded with white lines.

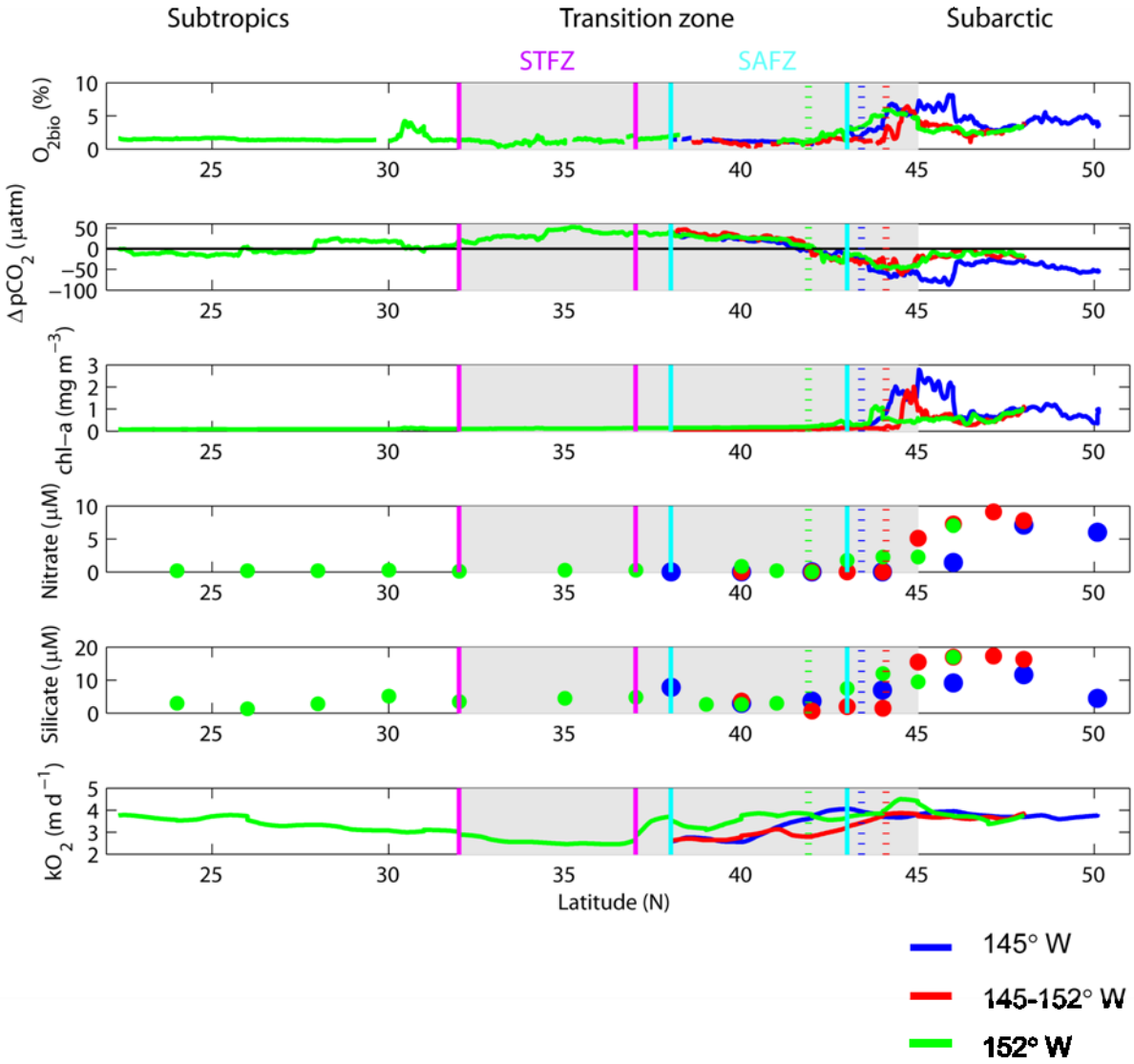

Figure 2.3: Continuous underway measurements of surface $\%O_{2bio}$, ΔpCO_2, *chl-a*, nitrate, silicate and k_{O2} along three legs of cruise track. Blue and magenta lines bound SAFZ and STFZ, respectively. Dotted vertical lines, position of TZCF (colors refer to cruise legs; see key). Transition zone is highlighted in grey.

2.4.2 Subarctic

In the subarctic, we observed high biological O_2 saturation ($\%O_{2bio}$) and *chl-a* and low ΔpCO_2, with high meridional and zonal variability (Figure 2.3). $\%O_{2bio}$ and *chl-a* were highly correlated.

pCO_2 was highly negatively correlated with $\%O_{2bio}$ and *chl-a*, and only weakly correlated with SST (Table 2.2). At the southern edge of the subarctic along 145° W, strong peaks in $\%O_{2bio}$ and *chl-a* were coupled with troughs in ΔpCO_2 (Figure 2.3). Surface nutrient concentrations at OSP (6 μM nitrate and 4 μM silicate, respectively) were lower than typical late summer concentrations of 9 μM nitrate and 14 μM silicate, *Harrison et al*., 2004; Figure 2.3).

NCP and CO_2 influx had similar spatial trends to $\%O_{2bio}$ and ΔpCO_2, and their mean values were highest in the subarctic among cruise regions (25.8 mmol C m^{-2} d^{-1} and 4.1 mmol C m^{-2} d^{-1}, respectively; Figure 2.4). *NCP* was highly correlated with CO_2 influx ($r = 0.89$), with a slope of 2.6 (Table 2.2). Flow cytometry results (Figure 2.4) show high concentrations of all three phytoplankton classes in the subarctic. *NCP* was most highly correlated with concentrations of microphytoplankton ($r = 0.50$) in this region.

Table 2.2: Mean values and correlation statistics for underway measurements

					Correlation coefficient (*r*)								
Region	***NCP*** **(mmol C m^{-2} d^{-1})[a]**	***CO_2 flux*** **(mmol C m^{-2} d^{-1})[a]**	**Climatol. *CO_2 flux* (mmol C m^{-2} d^{-1})[b]**	***Chl-a*** **(μg m^{-3})**	***$\%O_{2bio}$-chl-a***	**$\%O_{2bio}$-*pCO_2***	***SST-pCO_2***	***NCP-CO_2 influx***	***SST-CO_2 flux***	***NCP*-micro**	***NCP*-nano**	***NCP*-pico**	**Slope *NCP*-CO_2 influx**
										***NCP*-f_{micro}**	***NCP*-f_{nano}**	***NCP*-f_{pico}**	
Subarctic (45–50° N)	25.8 ± 4.6 [9.3]	–4.1 ± 0.9 [3.1]	–1.7 ± 0.3	0.8	0.82	–0.81	0.10	0.89	–0.17	0.50	0.17	0.15	2.8
										0.18	–0.08	0.05	
Transition (32–45° N)	11.8 ± 3.2 [11.8]	0.2 ± 0.0 [4.0]	1.5 ± 1.3	0.3	0.85	–0.75	0.87	0.85	0.84	0.89	0.83	0.58	2.4
										0.73	0.07	–0.16	
Northern (40–45° N)	17.1 ± 4.4 [13.7]	–2.1 ± 0.5 [4.0]	1.1 ± 1.0	0.4	0.83	–0.78	0.94	0.84	0.95	0.86	0.73	0.37	2.9
										0.75	0.05	–0.14	
Southern (32–40° N)	5.4 ± 1.8 [2.3]	3.0 ± 0.5 [0.7]	2.6 ± 1.8	0.1	0.54	0.21	0.18	–0.57	0.08*	0.68	0.21	–0.32	–1.6
										0.40	0.31	–0.33	
Subtropics (22–32° N)													
All data	8.1 ± 2.1 [2.6]	0.1 ± 0.0 [1.3]	0.8 ± 0.1	0.1	0.86	–0.17	–0.50	0.34	–0.50	0.12	-0.21	0.32	0.7
										0.08	–0.28	0.19	
Bloom region (30–31.2° N)	12.3	0.5	--	0.1	0.97	–0.69	–0.79	0.71	–0.79	0.74	-0.26	0.50	3.3
										–0.11	–0.57	0.52	

[a]Values for *NCP* and *CO_2 flux* are mean ± error of 1 σ (regional s.d. is in brackets). Negative *CO_2 flux* represents oceanic CO_2 uptake. Correlation coefficient (*r*) is shown between two parameters listed at top of each column. All correlations were significant ($P < 0.001$ for all cells except cell marked with an asterisk, $P < 0.02$). Micro, microphytoplankton; nano, nanophytoplankton; pico, picophytoplankton; f_{micro}, f_{nano} and f_{pico} are the respective fractions of total cell count made up by these phytoplankton classes. [b]Climatological *CO_2 flux* is presented for comparison, aligned with climatological boxes that most closely correspond to it: subarctic, 46–50° N; transition, 30–46° N; northern transition, 38–46° N; southern transition, 30–38° N; subtropics, 22–30° N.

2.4.3 Transition zone

The transition zone represented a shift from the high-chl-a, high-%O_{2bio}, low-pCO_2, high-nutrient conditions of the subarctic to opposite conditions in the subtropics. At the boundary between the northern transition zone and subarctic, in the vicinity of the TZCF, we observed coincident peaks in %O_{2bio} and *chl-a* and troughs in ΔpCO_2, with high zonal variability (Figure 2.3). In the southern transition zone (32–40° N), %O_{2bio} and chl-a decreased. At ~42° N, pCO_2 shifted from undersaturated values to the north to supersaturated values to the south, and remained supersaturated in the southern transition zone.

Throughout the transition zone, *chl-a* and %O_{2bio} were positively correlated ($r = 0.85$), and pCO_2 and %O_{2bio} were negatively correlated ($r = –0.75$), similarly to the subarctic. But in contrast with the subarctic, pCO_2 was positively correlated with SST ($r = 0.87$; Table 2.2). Surface nitrate and silicate declined from the subarctic to northern transition zone; nitrate approached the detection limit at the TZCF and remained <1 μM in the southern transition zone.

From the northern to the southern transition zone, *NCP* declined (mean 17.1 and 5.4 mmol C m^{-2} d^{-1}, respectively), and *CO_2 flux* varied from an influx to an efflux (Figure 2.4 and Table 2.2). Meridional and zonal (145–152° W) variability in fluxes were high in the northern transition zone. Throughout the transition zone, *NCP* and CO_2 influx were correlated with a similar r (0.85) and slope (2.4) to that in the subarctic (Table 2.2).

Throughout the transition zone, *NCP* was highly correlated with microphytoplankton and nanoplankton ($r = 0.89$ and 0.83, respectively), and less strongly correlated with picophytoplankton ($r = 0.58$). NCP was also highly correlated with the fraction of total cell count made up by microphytoplankton ($r = 0.72$). In the northern transition zone, high abundance of micro- and nanophytoplankton coincided with high *NCP* and CO_2 uptake (Figure 2.4).

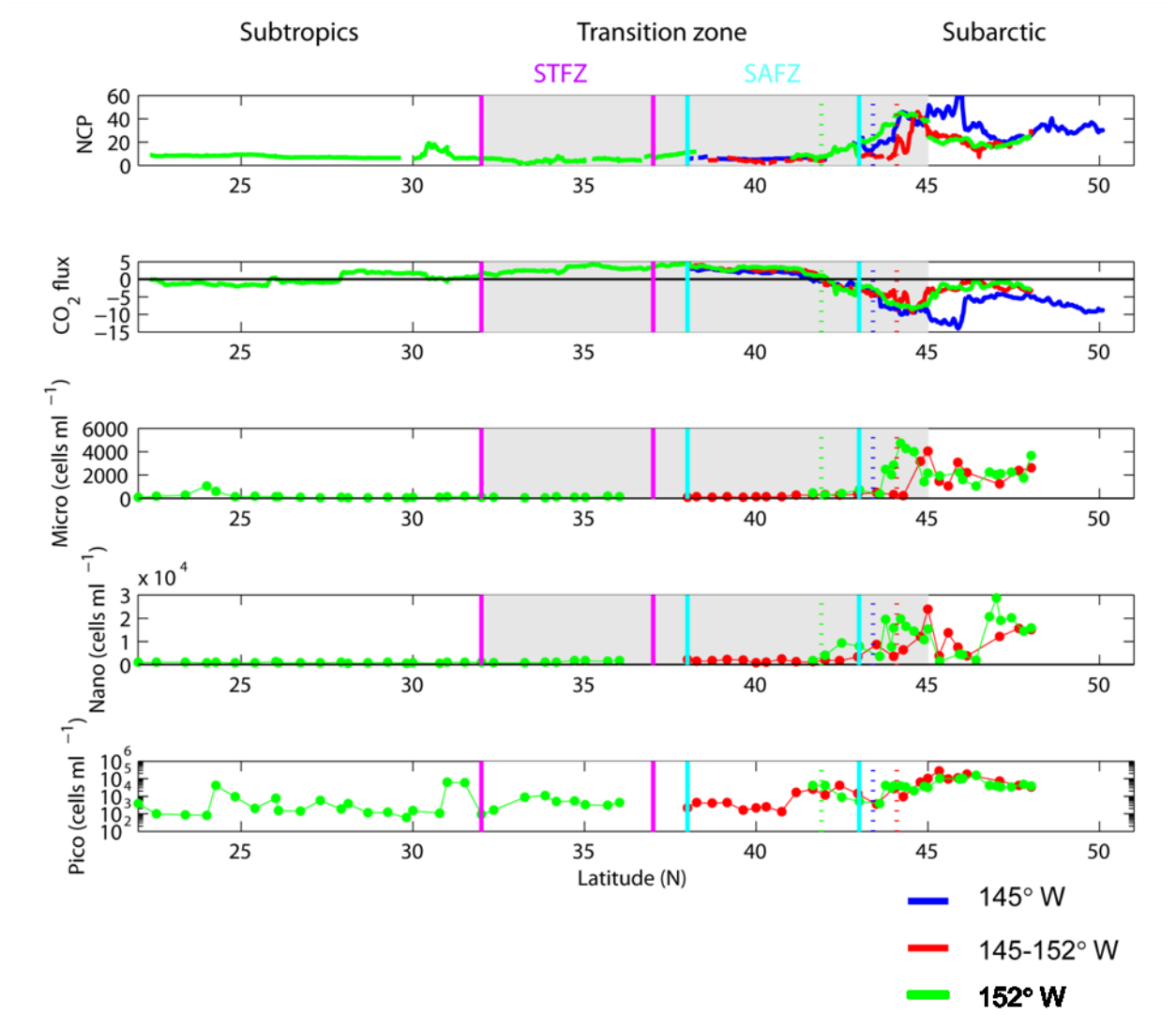

Figure 2.4: Continuous estimates of *NCP* and *CO_2 flux* and flow cytometry–derived concentrations of microphytoplankton (10–60 µm), nanophytoplankton (2–10 µm) and picophytoplankton (1–2 µm) along legs of cruise track. Units of *NCP* and *CO_2 flux* are mmol C m^{-2} d^{-1}; negative *CO_2 flux* represents oceanic CO_2 uptake. Picophytoplankton represent *Synechococcus* north of the TZCF and *Prochlorococcus* south of it. Blue and magenta lines bound SAFZ and STFZ, respectively. Dotted vertical lines, position of TZCF (colors refer to cruise legs; see key). Transition zone is highlighted in grey.

2.4.4 Subtropics

In the subtropics, $\%O_{2bio}$, chl-a, and nutrients were low, similar to conditions in the southern transition zone, with the exception of a small peak in $\%O_{2bio}$ at 30.5° N. ΔpCO_2 generally decreased southward from a maximum in the southern transition zone. Throughout the subtropics, chl-a was highly correlated with $\%O_{2bio}$ ($r = 0.86$). pCO_2 was weakly negatively correlated with both $\%O_{2bio}$ and SST (Table 2.2). Surface nitrate was below detection limit throughout most of the subtropics, and surface silicate averaged 3 µM.

Mean *NCP* in the subtropics (8.1 mmol C m^{-2} d^{-1}; Figure 2.4) was slightly higher than that in the southern transition zone. Mean *CO_2 flux* was close to zero, and CO_2 influx was weakly correlated with *NCP* (Figure 2.4 and Table 2.2). *NCP* was weakly correlated with picophytoplankton (*Prochlorococcus*) throughout the subtropics (Table 2.2). A peak in *NCP* at ~30.5° N of 22 mmol C m^{-2} d^{-1} corresponded to a small CO_2 influx. In the region of this peak (30–31.2° N), *NCP* was highly correlated with *chl-a* ($r = 0.97$) and CO_2 influx ($r = 0.69$), and the *NCP*:CO_2 influx slope (3.3) was similar to that observed in the subarctic and northern transition zone (Table 2.2).

2.5 Discussion

2.5.1 Rates of NCP and CO_2 uptake

In the subarctic, *NCP* (25.8 ± 4.6 mmol C m^{-2} d^{-1}) and CO_2 influx (4.1 ± 0.9 mmol C m^2 m^{-2} d^{-1}) reached their highest mean values along the cruise track. These values were ~2x higher than the mean of previous estimates of *NCP* and climatological CO_2 influx for this region (Table 2.1 and *Takahashi et al.*, 2009; Table 2.2). Mean *chl-a* (0.8 mg m^{-3}) was almost twice as high as usual for September based on the SeaWiFS 9-km *chl-a* time series for 1997–2010 (Figure 2.5),

reflecting a phytoplankton bloom in this region. This bloom was most likely stimulated by iron deposited with volcanic ash in the early August 2008 eruption of the Aleutian island volcano Kasatochi [*Hamme et al.*, 2010; *Langmann et al.*, 2010].

The high *NCP* and CO_2 influx in the subarctic estimated during our cruise were consistent with bloom conditions, although there is evidence that we sampled during a declining stage of this bloom. SeaWiFS *chl-a* in our cruise region declined from August to September and onward (Figure 2.5). At OSP, our O_2/Ar-based *NCP* on 30 August (30 mmol C m^{-2} d^{-1}) was lower than O_2/Ar-based *NCP* (43 mmol C m^{-2} d^{-1}) estimated on 21 August [*Hamme et al.*, 2010].

In the subtropics, mean *NCP* (8.1 ± 2.1 mmol C m^{-2} d^{-1}) was very similar to that previously observed at ALOHA (8 ± 4 mmol C m^{-2} d^{-1}; Table 2.1), indicating that observations at this station are generally representative of the NE Pacific subtropical region. *CO_2 flux* showed a weak efflux (0.1 ± 0.0 mmol C m^{-2} d^{-1}), ~8x lower than climatological September CO_2 efflux (Table 2.2). *Chl-a* in the subtropics (0.1 mg m^{-3}) was similar to typical September values from the SeaWiFS time series (Figure 2.5).

Although *NCP* in the subtropics was ~3x lower than in the subarctic during our cruise, we observed a peak in *NCP* at 30–31° N, 152° W (Figure 2.4) associated with the late summer bloom that has been previously observed in this region (~30° N, 130–160° W) and that can last up to 3–4 months [*Wilson et al.*, 2008]. This recurrent bloom has been attributed both to N_2 fixation by unicellular cyanobacteria and endosymbionts, and to *Rhizosolenia* diatom mats that can vertically migrate into the nitracline through ballasting [*Wilson*, 2003; *Wilson et al.*, 2008]. *NCP* estimates at 30–31° N peaked at 19 mmol C m^{-2} d^{-1}, ~2x the mean subtropical rate.

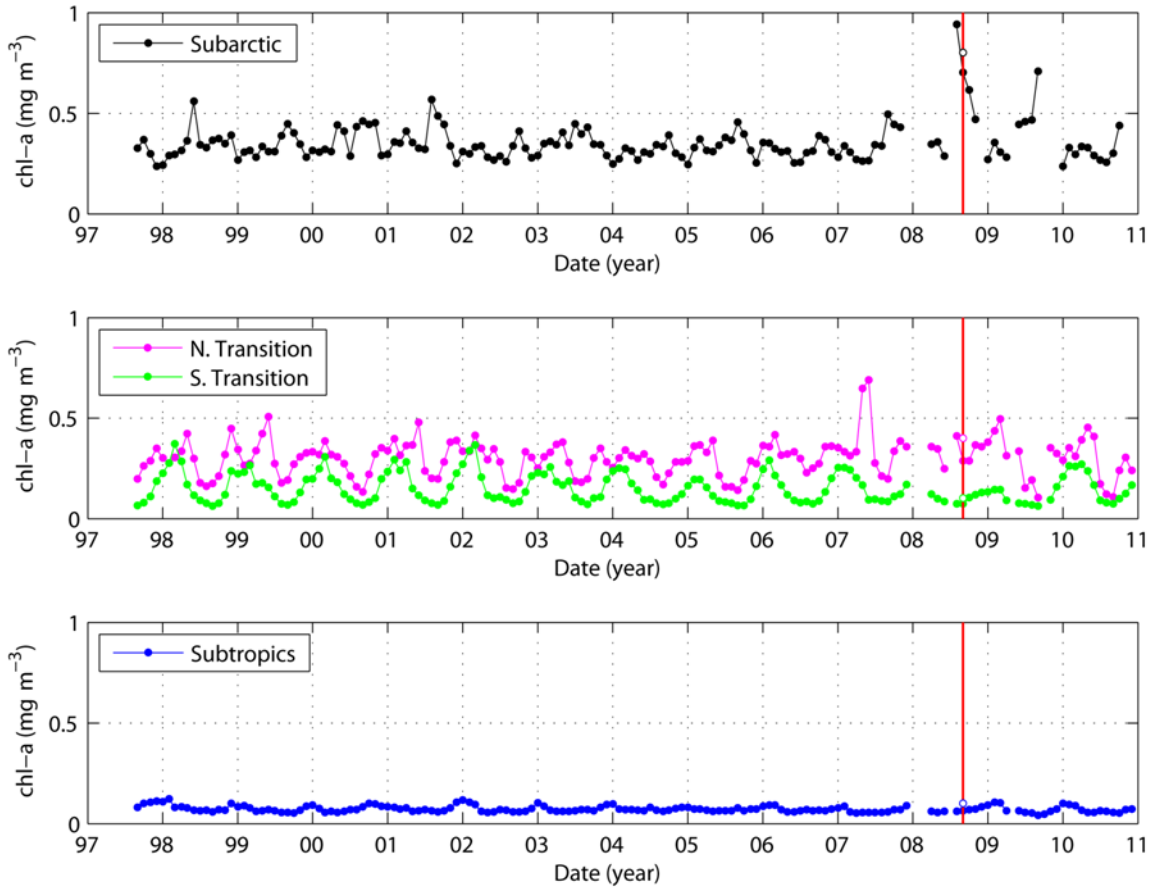

Figure 2.5: Time series of monthly satellite-based SeaWiFS 9-km *chl-a* (1997–2010) averaged over cruise regions (longitude 145–155° W, latitudes 45–50° N for subarctic, 40–45° N for northern transition, 32–40° N for southern transition, 22–30° N for subtropics). Grid lines mark beginning of each year. Red line marks month of cruise and open circles show mean *chl-a* measured on cruise. Figure made using data from NASA Giovanni.

The transition zone (32–45° N) had mean *NCP* intermediate between the subarctic and subtropics (11.8 ± 3.2 mmol C m^{-2} d^{-1}; Table 2.2), and within the range of previous *NCP* estimates in both the subarctic and transition zone (Table 2.1). Notably, *NCP* in the transition zone had much higher spatial variability than in the subarctic or subtropics, with regional s.d. of 11.8, equivalent to the mean (Table 2.2). It had mean CO_2 efflux (0.2 ± 0.0 mmol C m^{-2} d^{-1}) that was ~7x lower than September climatological efflux (Table 2.2).

In the northern transition zone, mean *NCP* (17.1 ± 4.4 mmol C m^{-2} d^{-1}) was similar to a previous estimate in this region (Table 2.1) and on the high end of previous summertime *NCP* estimates in the subarctic. Both meridional and zonal (145–152° W) *NCP* variability were high in this region (regional s.d. = 13.7, Table 2.2). CO_2 influx (2.1 ± 0.5 mmol C m^{-2} d^{-1}) here was greater than climatological September estimates, which show a mean efflux of 1.1 ± 1.0 mmol C m^{-2} d^{-1} (Table 2.2); this discrepancy could be attributable to the anomalous bloom conditions in the subarctic, or to interannual variability in the frontal dynamics of the transition region. Based on the SeaWiFS time series (Figure 2.5) *chl-a* was not anomalously high during our cruise in either of these regions, as it was in the subarctic. In the southern transition zone, *NCP* at 5.4 ± 1.8 mmol C m^{-2} d^{-1} was similar to previous estimates at ALOHA, and mean CO_2 efflux was 3.0 ± 0.5 mmol C m^{-2} d^{-1}, similar to the September climatological value in this region (Table 2.2).

Compared with a wealth of *NCP* estimates at OSP in the subarctic and ALOHA in the subtropics, we have only a few snapshots of *NCP* in the transition zone. Based on our results and previous studies, *NCP* in the northern transition zone resembles the subarctic, with comparably high summertime daily *NCP* rates (Table 2.1) and a strong link between *NCP* and CO_2 uptake. We observed the highest spatial variability in *NCP* and *CO_2 flux* in this region, and it has high interannual variability in satellite *chl-a* (Figure 2.5). Frontal dynamics in this region likely play a role in this temporal and spatial biological patchiness, as we discuss further below. In contrast, the southern transition zone resembles the subtropical gyre, with lower daily *NCP* rates that peak in spring, lower spatial variability and a summertime CO_2 efflux.

2.5.2 Impact of NCP on CO_2 uptake

Through the high spatial resolution of our measurements, we observed several regions in which *NCP* and CO_2 influx were highly coupled, demonstrating a link between the biological pump and atmospheric CO_2 uptake on a ~2-week timescale. In the subarctic, we observed this high correlation during the decline of the anomalous bloom (including micro- and nanophytoplankton) described above, most likely stimulated by volcanic deposition of iron. This could be characteristic of the "event-driven, mass sedimentation carbon pump" described by *Karl et al*. [2003] in which perturbations such as pulsed delivery of iron lead to blooms and aggregation of large phytoplankton like diatoms, resulting in rapid, efficient export events. These results indicate that intermittent iron supply in this region (through volcanic events, eddy transport from the continental shelf or atmospheric deposition) would lead to a stronger carbon sink on short-term (seasonal) timescales.

Throughout the transition zone, we observed similarly high correlation between *NCP* and CO_2 influx. *NCP* was highly correlated with concentrations of micro- and nanoplankton, which were abundant in the northern transition zone, and was highly correlated with the fraction of total cell count comprising microphytoplankton. The SAFZ, STFZ and TZCF have been found to be associated with high *PP*, *NCP* and abundance of microphytoplankton by other researchers [*Leonard et al.*, 2001; *Juranek*, 2007, *Howard et al.*, 2010, *Juranek et al.*, 2012].

Frontal dynamics may play a role in the biological patchiness observed in the transition zone due to (i) mesoscale perturbations associated with frontal zones, leading to dynamic upwelling [*Roden et al.*, 1991; *Olson*, 1994] that can bring nutrients to the surface and stimulate phytoplankton growth [*Strass*, 1992; *Denman*, 1995]; (ii) variations in Ekman convergence and resulting nutrient supply at the TZCF [*Ayers and Lozier*, 2010]; and (iii) convergence of biomass

(phytoplankton) at the TZCF [*Polovina et al.*, 2001], as has been observed at similar convergent fronts [*Mann and Lazier*, 2006; *Franks*, 1992; *Olson et al.*, 1994].

In the subtropics, phytoplankton abundance (*chl-a*) and $\%O_{2bio}$ were highly correlated as in the subarctic (Figure 2.3), but there was a much lower correlation between *NCP* and CO_2 influx (Table 2.2; $r = 0.20$ versus $r = 0.89$ in the subarctic). This probably results from the strong influence of temperature on the summertime CO_2 *flux* in this region, yielding a weaker link between *NCP* and CO_2 uptake. The dominance of picophytoplankton over nano- and microphytoplankton in the subtropics (Figure 2.3) may also lead to less efficient export.

We observed a peak in *NCP* at ~30° N, 130–160° W, where recurrent late summer phytoplankton blooms have been observed. In this region (30–31.2° N), *NCP* was highly correlated with *chl-a* and CO_2 influx, and the slope of this correlation was similar to that observed in the subarctic and transition zone (Table 2.2). At this location, microphytoplankton and picophytoplankton (*Prochlorococcus*) dominated, and their abundances were highly correlated with *NCP* ($r = 0.70$ and 0.45, respectively).

2.5.3 Impact of NCP on CO_2 uptake over annual cycle

Our snapshot observations demonstrate the strong link between *NCP* and CO_2 uptake in the subarctic and transition zone. However, our larger goal is to put these estimates in the context of determining the impact of *NCP* on annual CO_2 uptake in the North Pacific. To do this, we made two box model calculations to examine the seasonal cycle of pCO_2 and *DIC* in our cruise region using a climatological surface pCO_2 data set in boxes of 4° latitude x 5° longitude [*Takahashi et al.*, 2009; see Methods, section 2.3.6]. We first examined the seasonal cycle of pCO_2 in a simplified "abiotic" system in which only temperature and gas exchange influence pCO_2 and

CO_2 flux. Second, we used a simplified *DIC* mass balance approach to compare the annual climatological *CO_2 flux* with the contribution of *NCP* and physical input of *DIC*.

2.5.3.1 Abiotic pCO_2 model

A simplified mass balance of DIC in the mixed layer can be written as:

$$\frac{dDIC}{dt} = \frac{1}{h} FCO_{2\,(in)} + J_{\text{phys}} + J_{\text{ncp}} \quad (2.4)$$

where $FCO_{2(in)}$ is the sea-air flux of CO_2 ($k\text{CO}_2 * k_H(p\text{CO}_{2\text{atm}} - p\text{CO}_{2\text{SW}})$), with positive $FCO_{2(in)}$ defined as into the ocean (note this is the opposite of the sign convention in equation (2.3) and our results), h is the mixed layer depth, J_{phys} is the physical input of *DIC* due to advection, diffusion and entrainment (with supply of DIC defined as positive and removal as negative), and J_{ncp} is the export of carbon due to *NCP* (with respiratory source of *DIC* defined as positive and biological uptake of *DIC* as negative). The annual cycle of $FCO_{2(in)}$ is mainly controlled by seasonal changes in surface ocean $p\text{CO}_2$ with a secondary effect of variation in $k\text{CO}_2$ due to seasonal wind speed variation.

To separate the influence of temperature on $p\text{CO}_2$ from the biological and physical effects, we described seasonal changes in $p\text{CO}_2$ in an "abiotic" ocean in which only warming or cooling and air-sea gas exchange influenced seasonal changes in *DIC* and $p\text{CO}_2$. In this case, the *DIC* mass balance simplifies to:

$$\frac{dDIC}{dt} = \frac{1}{h} FCO_{2\,(in)} = \frac{1}{h}\, kCO_2\, k_H \left(p\text{CO}_{2\text{atm}} - p\text{CO}_{2\text{SW}}\right) \quad (2.5)$$

We initialized this abiotic model with the 1 March climatological $p\text{CO}_{2\text{SW}}$ and *DIC*. We calculated the initial $FCO_{2(in)}$ based on the 1 March climatological $p\text{CO}_{2\text{SW}}$, $p\text{CO}_{2\text{atm}}$, k_H and $k\text{CO}_2$. We distributed this $FCO_{2(in)}$ over a daily time step and recalculated d*DIC*/d*t* and $p\text{CO}_{2\text{SW}}$ based on thermodynamic equilibrium (using climatological daily-interpolated values of *h*,

alkalinity, pCO_{2atm}, temperature, salinity, k_H and kCO_2; see Methods for details), and repeated the process for each subsequent daily time step. In the region of our study, the mixed layer generally begins to shoal in March, and therefore we assume that any influence of entrainment on *DIC* is negligible until late summer or early fall, when the mixed layer begins to deepen again.

The observed (climatological) pCO_2 peaks in summer in all boxes in our cruise region along 152° W, yielding a summertime CO_2 efflux in all regions (Figure 2.6). In the abiotic model, however, the estimated summertime increase in pCO_2 (and thus CO_2 efflux) is greater than the observed pCO_2 in all boxes. Biological (J_{ncp}) and physical (J_{phys}; equation (2.4)) input or removal of *DIC* must be responsible for the difference in annual cycles of the predicted abiotic and observed pCO_2. In spring and summer in the subarctic and transition zone, when the mixed layer is shoaling or stable and wind speeds are low, removal of *DIC* by J_{ncp} is much greater than net removal by J_{phys} [*Ayers and Lozier*, 2012], and is the dominant cause of the observed pCO_2 (pCO_{2SW}) being less than the abiotic pCO_2 (pCO_{2abio}). In the subtropics in spring and summer, based on studies at ALOHA, J_{ncp} is the only term removing *DIC*, because J_{phys} is a net *DIC* source [*Keeling et al*., 2004; *Quay and Stutsman*, 2003]. In contrast, in fall and winter, when the mixed layer is deepening, addition of *DIC* through positive J_{phys} outweighs removal of *DIC* by J_{ncp} in the subarctic, transition zone and subtropics [*Ayers and Lozier*, 2012; *Keeling et al*., 2004], and causes pCO_{2SW} to be greater than pCO_{2abio}.

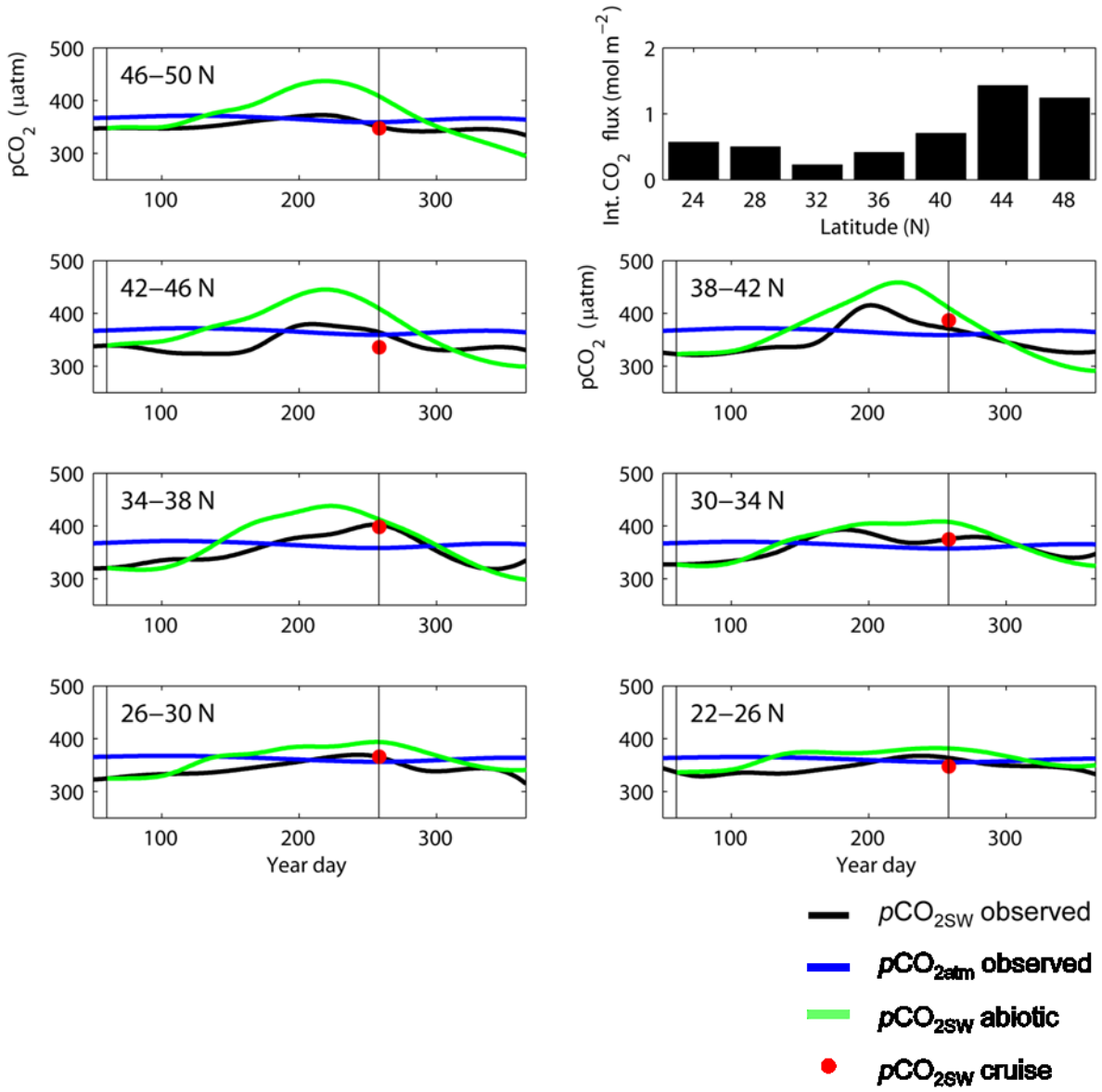

Figure 2.6: Abiotic model of annual pCO_2 cycle in cruise region along 152º W. Observed (climatological) ocean and atmosphere pCO_2, black and blue lines, respectively. Modeled abiotic pCO_2, green line. Red dot, pCO_2 measured on cruise in this study (September) normalized to year 2000 pCO_2 for consistency with climatological data [*Takahashi et al*., 2009]. Black vertical lines bound spring-summer period (1 March–15 September). Top right graph, integrated CO_2 flux due to difference between abiotic and observed pCO_2 (for period when abiotic pCO_2 is greater than observed pCO_2 in each box).

We calculated the integrated CO_2 flux resulting from the difference between pCO_{2abio} and pCO_{2SW} by summing daily CO_2 flux = $k_{CO2}\, k_H\, (pCO_{2abio} - pCO_{2SW})$ for the period in each box

when pCO_{2abio} is greater than pCO_{2SW}, typically March–September. The trends in this integrated flux along the cruise track largely correspond to the trends in *NCP* and $FCO_{2(in)}$ we observed on our cruise (Figure 2.6). The integrated flux is greatest in the subarctic (46–50° N) and northern transition zone (38–46° N), implying high summer drawdown of pCO_2 by *NCP* (assuming J_{phys} is small), in agreement with our cruise observations of high *NCP* and strong coupling of *NCP* and CO_2 uptake in these regions. The integrated flux is lower in the southern transition zone (30–38° N) and subtropics (22–30° N), in agreement with our cruise observations in these regions of lower *NCP*, CO_2 efflux, and little coupling between *NCP* and $FCO_{2(in)}$. pCO_{2SW} is lower than pCO_{2abio} for the longest interval (>240 days) in the subtropics, as a result of a long growing season, and in the subarctic and northern transition zone (which has both a spring and a fall bloom, *Longhurst*, 2007).

2.5.3.2 DIC mass balance

We next used a simplified version of the *DIC* mass balance approach of *Lee et al.* [2007] to compare the annual climatological $FCO_{2(in)}$ with the contribution of *NCP*. Rearranging the *DIC* mass balance (equation (2.4)), the magnitude of *DIC* drawdown plus CO_2 invasion must be the net result of *NCP* plus physical supply:

$$J_{\mathrm{ncp}} + J_{\mathrm{phys}} = \frac{dDIC}{dt} - \frac{1}{h} FCO_{2(in)} \tag{2.6}$$

We again initialized the model with the 1 March value of pCO_2 and climatological *DIC*. We calculated daily $FCO_{2(in)}$ and salinity-normalized d*DIC*/d*t* using daily-interpolated data described above and solved for $J_{ncp} + J_{phys}$. Initially, we assumed $J_{phys} = 0$ during the well-stratified spring-summer season (when observed pCO_2 is less than abiotic pCO_2, typically March–September) to obtain an estimate of J_{ncp}. This would result in an upper-boundary estimate

for NCP in the transition zone (where J_{phys} removes a small amount of *DIC* in spring-summer; *Ayers and Lozier*, 2012) and a minimum estimate of *NCP* in the subtropics (where J_{phys} is positive in spring-summer; *Keeling et al*., 2004). We integrated this estimate of summer *NCP* by integrating the values of $J_{ncp} + J_{phys}$ for the period 1 March–15 September (Figure 2.7).

To obtain the observed summertime pCO_2 decrease (if $J_{phys} = 0$) requires mean daily *NCP* in the subarctic and northern transition zone of 10 and 13 mmol C m^{-2} d^{-1}, respectively (Table 2.3). These values are slightly lower but within the range of uncertainty of previous field estimates for these regions (Table 2.1). Our cruise-based *NCP* estimate was more than 2x than the model estimate in the subarctic (26 mmol C m^{-2} d^{-1}), likely reflecting the anomalous conditions there during our cruise, and 31% greater in the northern transition zone.

In the southern transition zone and subtropics, modeled summer *NCP* was about half that in the subarctic and northern transition zone, at 5–6 mmol C m^{-2} d^{-1}, similar to our cruise estimates of 5–8 mmol C m^{-2} d^{-1} and within the uncertainty of previous field estimates of *NCP* in these regions (Tables 2.1 and 2.3). The ~2x lower summer *NCP* in the subtropics compared to the northern transition zone is similar to the meridional trends in *NCP* estimated from our cruise observations. This suggests that our O_2/Ar-based *NCP* in the transition zone and subtropics during September 2008 may be representative of the climatological *NCP* during the spring-summer growing season. Modeled *NCP* in the subtropics (5 mmol C m^{-2} d^{-1} versus our cruise-based estimate of 8 mmol C m^{-2} d^{-1}) is probably underestimated because physical supply of *DIC* in the subtropics is positive during the summer, as has been shown at ALOHA [*Keeling et al.*, 2004; *Quay and Stutsman*, 2003]. In support of this, the stability ($\Delta\sigma/\Delta z$) in the upper water column in the subtropics and southern transition zone was much less than that in the subarctic

during our late summer cruise (Figure 2.2).

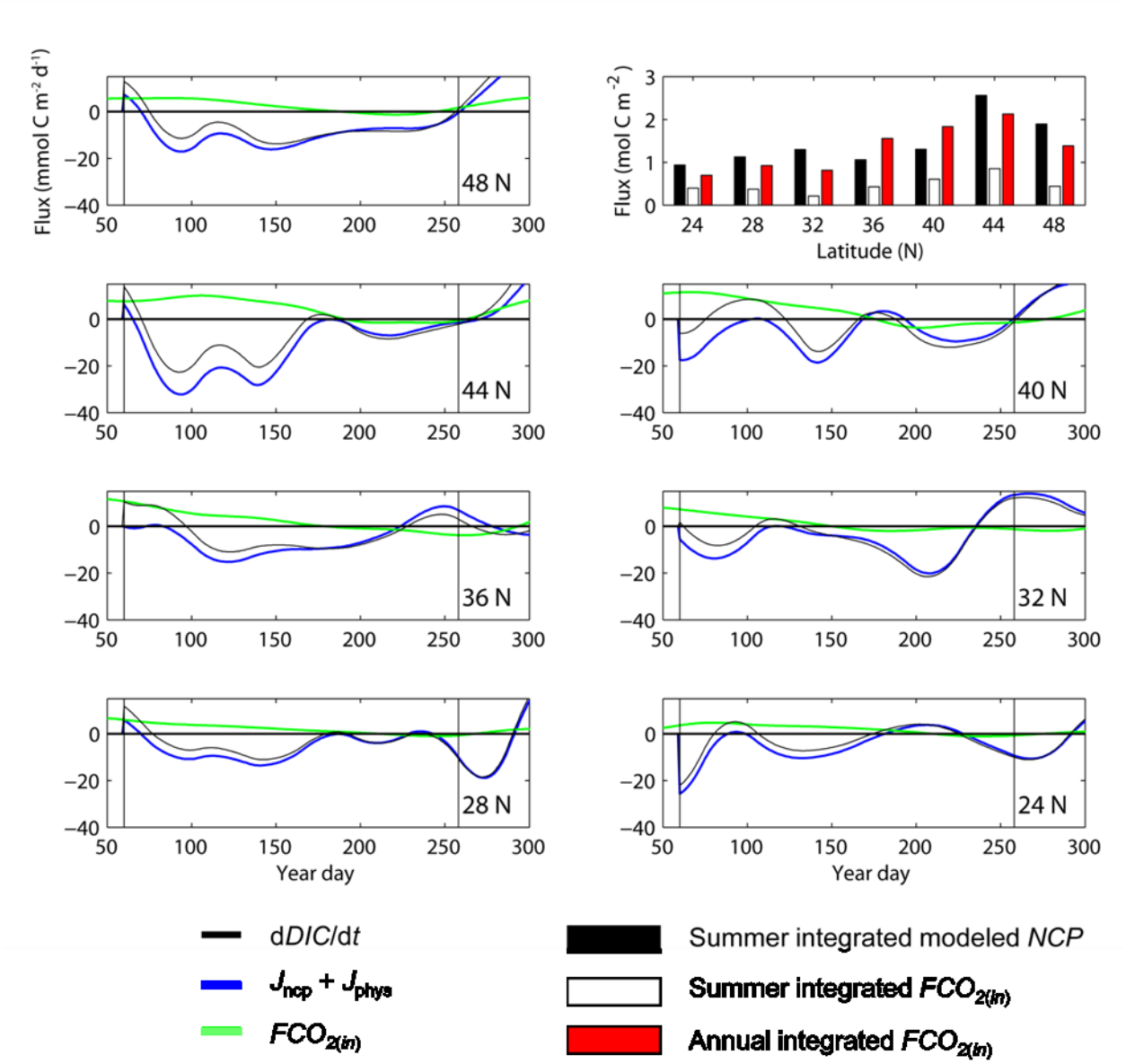

Figure 2.7: Model of climatological pCO_2 and *DIC* seasonal cycle, distinguishing influence of $FCO_{2(in)}$ and *NCP* plus physical inputs ($J_{ncp} + J_{phys}$) on seasonal changes in DIC (d*DIC*/d*t*). Black vertical lines bound spring-summer period (1 March–15 September) over which summer *NCP* and $FCO_{2(in)}$ (top right) were integrated.

Integrated annual climatological $FCO_{2(in)}$ was similar in magnitude to modeled summer-integrated *NCP* along the cruise track, peaking in the northern transition zone at 2.0 mol C m^{-2} yr^{-1}, slightly lower in the subarctic and southern transition zone (1.2–1.4 mol C m^{-2} yr^{-1}), and lowest in the subtropics at 0.8 mol C m^{-2} yr^{-1} (Figure 2.7 and Table 2.3). On average, the magnitude of summer-integrated *NCP* balances annual-integrated $FCO_{2(in)}$ across the cruise track, with ratios of summer *NCP* to annual $FCO_{2(in)}$ of 0.7–1.4 across all regions (Table 2.3). Some carbon exported through *NCP* during summer could be remineralized and returned to the mixed layer in winter, as has been observed in the North Atlantic [*Körtzinger et al*., 2008]; this would lower O_2/Ar-based *NCP* and CO_2 uptake. However, winter mixed layer depths in the NE Pacific are much lower than in the North Atlantic, so the effect may not be as pronounced there.

We conclude that *NCP* exerts a significant control on the high CO_2 uptake in the NE Pacific, with the remainder of annual CO_2 uptake impacted by surface cooling and physical processes. It is difficult to directly estimate the contribution of *NCP* to annual CO_2 uptake, because the response time of CO_2 gas exchange with respect to changes in temperature and DIC is relatively sluggish (~1 year) [*Broecker and Peng*, 1982]. Therefore, *NCP* that takes place in summer likely drives uptake of CO_2 in fall or winter.

Table 2.3: Results of model of climatological pCO_2 and *DIC* seasonal cycle

Latitude (N) along 152° W	Summer-integrated modeled *NCP* (mol C m^{-2})*	Daily average summer modeled *NCP* (mmol m^{-2} d^{-1})	Summer-integrated $FCO_{2(in)}$ (mol C m^{-2})*	Annual-integrated $FCO_{2(in)}$ (mol C m^{-2} yr^{-1})	Summer-integrated modeled *NCP* / Annual-integrated $FCO_{2(in)}$
46–50°	1.9	9.5	0.4	1.4	1.4
42–46°	2.6	13.1	0.9	2.1	1.2
38–42°	1.3	6.5	0.6	1.8	0.7
34–38°	1.1	5.5	0.4	1.6	0.7
30–34°	1.3	6.5	0.2	0.8	1.6
24–30°	1.1	5.5	0.4	0.9	1.2
22–24°	0.9	4.5	0.4	0.7	1.3
Subarctic	1.9	9.5	0.4	1.4	1.4
N. Transition	2.0	10.1	0.8	2.0	1.0
S. Transition	1.2	6.0	0.3	1.2	1.2
Subtropics	1	5.0	0.4	0.8	1.3

*Summer-integrated modeled *NCP* and $FCO_{2(in)}$ are integrated for the period 1 March–15 September. In model, positive $FCO_{2(in)}$ represents influx into ocean. Regions were defined as described in Table 2.2.

2.5.4 Conclusions

Mean *NCP* and CO_2 influx along our cruise track were greatest in the subarctic (25.8 ± 4.6 and 4.1 ± 0.9 mmol C m^{-2} d^{-1}, respectively) and the northern transition zone (17.1 ± 4.4 and 2.1 ± 0.5 mmol C m^{-2} d^{-1}, respectively). In the subarctic, our observations of *NCP* were ~2x the mean of previous summer observations, reflecting the influence of an anomalous phytoplankton bloom. In the transition zone, we detected high zonal and meridional variability in *NCP* and *CO_2 flux* at <5-km scales, suggesting the impact of frontal dynamics on biogeochemical fluxes in this region, and the need for observations throughout the year to determine its mean annual state. In the southern transition zone and subtropics, *NCP* (5.4 ± 1.8 and 8.1 ± 2.1 mmol C m^{-2} d^{-1}, respectively) was about 2–3x lower than in the subarctic and northern transition zone, and CO_2 had mean efflux (3.0 ± 0.5 and 0.1 ± 0.0 mmol C m^{-2} d^{-1}, respectively).

NCP and CO_2 influx were highly correlated in the subarctic and transition zone with a slope of 2 to 3, indicating the strong coupling between biological uptake and CO_2 influx during summertime in these regions. *NCP* in these regions was also highly correlated with concentrations of microphytoplankton. In contrast, *NCP* and CO_2 influx were not strongly coupled in the subtropics, suggesting that the temperature effect on solubility dominates CO_2 flux during summertime there. In the subtropics, *NCP* was uncorrelated with microphytoplankton and weakly correlated with picophytoplankton, potentially indicating the lower efficiency of a picophytoplankton-dominated biological pump.

Our analysis and modeling of the climatological *DIC* and pCO_2 cycles in the transition zone and subtropics yielded a similar meridional pattern in integrated summertime *NCP* and *CO_2 flux* as we found during our cruise in September 2008. *NCP* in the northern transition zone was ~2–3x that in the southern transition zone and subtropics, suggesting that our snapshot

estimates in these regions are representative of the seasonal influence of *NCP* on CO_2 influx. Based on our model of the climatological seasonal *DIC* and pCO_2 cycle in the Northeast Pacific, we conclude that summertime *NCP* is similar in magnitude to the annual atmospheric CO_2 uptake in the NE Pacific, indicating that *NCP* has a significant impact on CO_2 uptake in this region. More continuous observations of the temporal and spatial variability of the biological pump in this region and more sophisticated physical modeling would improve our ability to distinguish the magnitude of the influences of temperature, biological uptake, and physical dynamics in this region of high CO_2 uptake.

Chapter 3

Impact of net community productivity on air-sea CO_2 uptake in the North Pacific based on basin-wide underway measurements of O_2/Ar and pCO_2

3.1 Introduction

A major unknown in ocean biogeochemistry is how ocean biology will respond to changes in the Earth system. Marine phytoplankton not only support global fisheries and biodiversity, but affect the concentration of atmospheric carbon dioxide by fixing carbon via photosynthesis and exporting it to the deep ocean. To predict the ocean's response to increasing atmospheric CO_2 and global warming, we need excellent benchmark measurements of the spatial and temporal variability of ocean primary productivity and the magnitude of organic carbon export to the deep ocean, known as the biological pump, and an improved understanding of the controls on these processes [Falkowski *et al.*, 1998; Chavez *et al.*, 2011].

The magnitude of the ocean's biological pump is equivalent at steady state to net community productivity (*NCP*), or gross primary productivity (GPP) minus community respiration. *NCP* has been estimated through field-based surface layer budgets of dissolved gases (O_2, Ar and N_2), NO_3, DIC, and $d^{13}C$-DIC; the in situ O_2/Ar method; the ^{234}Th-^{238}U disequilibrium method; and ^{15}N and ^{13}C uptake (see Table 3.1), inverse modeling [Najjar and Keeling, 2000; Louanchi and Najjar, 2000; Schlitzer, 2004; Lee, 2006], and satellite-based

estimates of NPP [Behrenfeld and Falkowski, 1997; Behrenfeld *et al.*, 2005; Westberry *et al.*, 2008] paired with export algorithms [Eppley and Peterson; Laws, 2000; Dunne *et al.* 2005; Falkowski *et al.*. 1998]. Globally estimates of *NCP* range 8–15 Pg C yr^{-1} [Emerson and Hedges, 2008]. However, there is large spatial and temporal variation in these rates, and an incomplete understanding of the controls on them. Satellite-based estimates of primary productivity (PP) have been found to agree only within a factor of two [Carr *et al.*, 2006], indicating that more groundtruthing of these estimates is needed.

Understanding the magnitude of the biological pump in the North Pacific is important because atmospheric CO_2 uptake in this region is much higher than the ocean-wide average, especially in the transition zone between the subarctic and subtropical gyres (30–45° N) [Takahashi *et al.*, 2002, 2009]. The physical dynamics and ecology of the North Pacific are also highly responsive to interdecadal and long-term climate variability [Yoo *et al.*, 2008; Dore *et al.*, 2003]. However, global and regional biogeochemical models struggle to replicate seasonal and interannual pCO_2 variability in the North Pacific, especially in the physically dynamic northwest Pacific. They especially have difficulty representing the impact of the biological pump on air-sea CO_2 flux [McKinley *et al.*, 2006].

It is unclear how much *NCP* contributes to the high CO_2 uptake in the transition zone. Lee [2001] found high *NCP* in this region based on seasonal *DIC* drawdown. Takahashi *et al.* [2002] attribute the large CO_2 sink to a combination of temperature's influence on the solubility effect on CO_2 (due to the cooling of subtropical waters as they move northward) and biological uptake. In contrast, Ayers and Lozier [2012] recently modeled CO_2 uptake in the transition zone and concluded that although temperature-driven solubility strongly affects seasonal pCO_2 trends,

it controls only ~17% of the annual sink in this region, with the remainder contributed by biological export and geostrophic divergence of *DIC*.

NCP has been studied thoroughly at three time series locations in the North Pacific, Station P in the subarctic NE Pacific (50° N, 145° W), Station ALOHA (22° 45 N, 158° W) in the subtropical NE Pacific, and Station KNOT (44° N, 155° E) in the subarctic NW Pacific [Table 3.1]. Studies at these sites have found higher *NCP* in the NW versus the NE subarctic Pacific [Harrison *et al*., 2004] and roughly equivalent *NCP* in the subarctic and subtropical NE Pacific [Emerson *et al*., 2008; Emerson and Stump, 2010]. However, apart from surveys of the basin by volunteer observation ship [Wong *et al*., 2002; Chierici *et al*., 2006] and satellite-based analyses [Goes *et al.*, 2004, 2004a], there have been few basin-scale, synoptic surveys of *NCP*, so it is unclear how representative these time series are of the basin.

Recently, continuous underway measurements of O_2/Ar using equilibrator inlet mass spectrometry [EIMS; Tortell, 2005; Kaiser *et al*., 2005; Cassar *et al*., 2009] and of pCO_2 [Pierrot *et al*., 2009], combined with a wind speed parameterization of gas transfer velocity, have made it possible to make synoptic, basin-scale estimates of *NCP* and air-sea CO_2 flux at kilometer-scale resolution [e.g., Nemcek *et al*. 2008; Guéguen and Tortell, 2008; Stanley *et al*., 2010; Cassar *et al.*, 2011]. The O_2/Ar-based estimate of *NCP* integrates over the residence time of oxygen in the mixed layer, on average ~2 weeks in the North Pacific, providing comparable spatial and temporal coverage to satellite-based estimates of carbon export.

Table 3.1: Upper ocean *NCP* in North Pacific subarctic, transition, and subtropical regions

Region	Annual NCP (mol C m^{-2} yr^{-1})	Daily NCP (mmol C m^{-2} d^{-1})		
		Winter	*Spring-summer*	*Fall*
Western subarctic				
KNOT (44° N, 155° E)	3.2[a]	6[b], 2[k]	9[b], 28[c], 21–50[d], 5–28[k]	7[b],10[k]
Other WSG observations: *Shipboard*	3.2[a], 2.9–3.4[e], 5.4[f], (6.3; 3)[g], 2.6[l], 4.8 ± 2.1*	3[k]; 0*	(18; 22)[c], 15–18[e]; (39; 15)[g], 3–47[k], 6–10[s], (7 ± 4; 29 ± 14)*	4–7[k], 4[m], 16 ± 7*
Satellite	2.6–5.8[t]			
Inverse models	3.7[h]			
Oyashio region observations: *Shipboard*	6.9[g], 9.1 ± 1.7*	0*	45[g], 9–102[i], 10–36[k], (8 ± 1; 64 ± 10)*	26 ± 5*
Inverse models	6.1[h]			
Eastern subarctic				
OSP (50° N, 145° W)	2.0 ± 0.3[j]		14 ± 5[j]	
Other eastern subarctic observations *Shipboard*	1.9[f], (3.1; 2.6)[g], 2–2.7[u], 4.5 ± 1.5*	10 ± 3*	(18; 15)[g], (4 ± 1; 21 ± 7)*	2–3[m]; 26[p]; 13 ± 4*
Satellite	0.8–2.5[t]			
Western transition zone				
Kuroshio region observations	2.7[g], 1.9[l], 4.5 ± 3.3*	2–14[k], 0*	17[g], 23–87[i], 15[r]; (17 ± 5; 21 ± 8)*	5–16[k]; 13 ± 3*
Other western transition zone observations	2.6[g], 3.7 ± 1.7*	3–8[k], 0*	15[g], 12[k], (10 ± 3; 18 ± 7)*	4[k]; 11 ± 3*
Eastern transition zone				
Eastern transition zone observations	2.6[g], 3.5–4[u], (2.3 ± 0.6; 2.8 ± 1.1)*	(7 ± 2; 5 ± 2)*	13–21[n], 8[o], (Spring, [5 ± 1; 7 ± 3]; Summer, 6 ± 3)*	3[o]; 12[p], (8 ± 3; 13 ± 5)*
Subtropics				
ALOHA (22.45° N, 158° W)	2.7 ± 0.9[j]		3–15[j]; 12-month average: 5–12[j]	
Other subtropical observations	2.4[q], 2.5–3.5[u]	6 ± 5*	2 ± 2*	8[p]

Table 3.1 continued. Details of studies are in footnotes, including reference, method, depth criterion, and spatial coverage. Asterisks indicate results from this study.

[a]Andreev *et al*. [2002]; *DIC* mass balance; 100 m. 50° N, 165–170° E.
[b]Harada and Shibamoto [2002]; ^{234}Th; 100m.
[c]Kawakami *et al*. [2007]; seasonal NO_3 drawdown; 100 m. In WSG, K1 (51° N, 165° E) and K2 (47° N, 160° E), respectively.
[d]Tsurushima [2002]; seasonal nutrient drawdown; 100 m; higher in spring.
[e]Midorikawa *et al*. [2002]; seasonal *DIC* drawdown; 100 m. In WSG, 48° N, 165° E.
[f]Chierici *et al*. [2006]; 50 m; *DIC* mass balance. In WSG, 45-51° N, 155–165° E. In Eastern subarctic, Alaska gyre.
[g]Wong *et al*. [2002]; seasonal nitrate drawdown. In WSG, ~45–55° N, 140–170° E and 45–55° N, 170–190°, respectively. In Oyashio, 42–45° N, 140–160° E. In Kuroshio, 35–42° N, 140–160° E. In TZW, 40–42° N, 160–220°. In eastern subarctic, Alaska gyre and subarctic current, respectively.
[h]Sasai and Ikeda [2003]; *DIC* model.
[i]Sugiura and Tsunogai [2005]; *DIC* budget; 25 m (ML); summer; highest subarctic values at Oyashio front; highest transition values at Kuroshio front. In Oyashio, 42–44° N, 155° E. In Kuroshio, 34–42°N, 155° E.
[j]Mean ± s.d. and ranges derived from various studies cited in Lockwood *et al*. [2012].
[k]Kawakami *et al*, 2004; ^{234}Th; 75–150 m. In WSG, 45–50° N, 156–170° E. In Kuroshio, 35–40° N, 140–160° E. In TZW, 40° N, 165–170° E.
[l]Kawakami and Honda, 2007. ^{234}Th. In WSG, K2 (47° N, 160° E). In Kuroshio, 39° N, 160° E (K3).
[m]Kawakami *et al* 2010. ^{234}Th. 100 m. In WSG, 46–51° N, 160–170° E. In ESG, 46–50° N, 145–175° W.
[n]Juranek *et al*. [2012], mixed layer O_2/Ar budget.
[o]Howard *et al*. [2010], euphotic zone O_2/Ar budget.
[p]Lockwood *et al*. [2012], mixed layer continuous O_2/Ar budget.
[q]Quay *et al*. [2009], *DIC*-d^{13}C mixed layer mass balance. 20–25° N.
[r]Tsuda *et al*. [2002] (in Japanese); data as cited in Honda [2003]. 50 m. A-line.
[s]Elskens *et al*. [2008]. ^{13}C and ^{15}N uptake. 50 m. 47° N, 161° E.
[t]Goes *et al*. [2004]. Spatial coverage includes both subarctic and transition zone.
[u]Sonnerup *et al*. [2013]. Depth-integrated in situ oxygen utilization rates. In Eastern subarctic, 45–48° N, 152° W; in Eastern transition zone, 30–40° N, 152° W; in Subtropics, 20–30° N, 152° W.
*This study (mean ± uncertainty). In eastern transition zone, values are for transition zone east (TZE) and transition zone coastal (TZC) provinces, respectively.

In this study, we made 13 surveys of the North Pacific using volunteer observation ships during 2008–2011. Our objectives in this study were: (i) to determine spatial and temporal (regional and seasonal) variability in rates of *NCP* and CO_2 flux across the North Pacific basin; (ii) to compare these estimates with previous field and model-based estimates in the region; and (iii) to use oxygen and carbon budgets to estimate the influence of *NCP* on CO_2 flux in this region.

In this paper, we present the results of O_2/Ar-based *NCP*, CO_2 flux, and other indices from our 13 cruises according to season in sections 3.4.1–3.4.4. In section 3.4.5, we construct a composite annual cycle of *NCP* in eight provinces of the North Pacific and determine the influence of physical processes on the O_2 and O_2/Ar budgets and *NCP* estimates based on our climatological box models of O_2 and O_2/Ar in the mixed layer (described in section 3.3.4). In section 3.4.6 we calculate integrated annual *NCP* in each province using our corrected estimates. Finally, in section 3.4.7, we estimate the influence of *NCP* on annual air-sea CO_2 flux in these provinces.

3.2 Background

3.2.1 Setting

The North Pacific consists of subarctic and subtropical regions, with a transition region in between (~30–45° N; Figure 3.1). In the subarctic North Pacific, two large anticyclonic gyres circulate, the western subarctic gyre (WSG, ~140–170° E) and the Alaska gyre (AG, ~130–170° W; Figure 3.1). The WSG is bounded to the west by the Oyashio current, which flows south along the east coast of Hokkaido and then curves eastward. The subarctic current, flowing eastward across the basin at 40–45° N, forms the southern boundary of the WSG and AG.

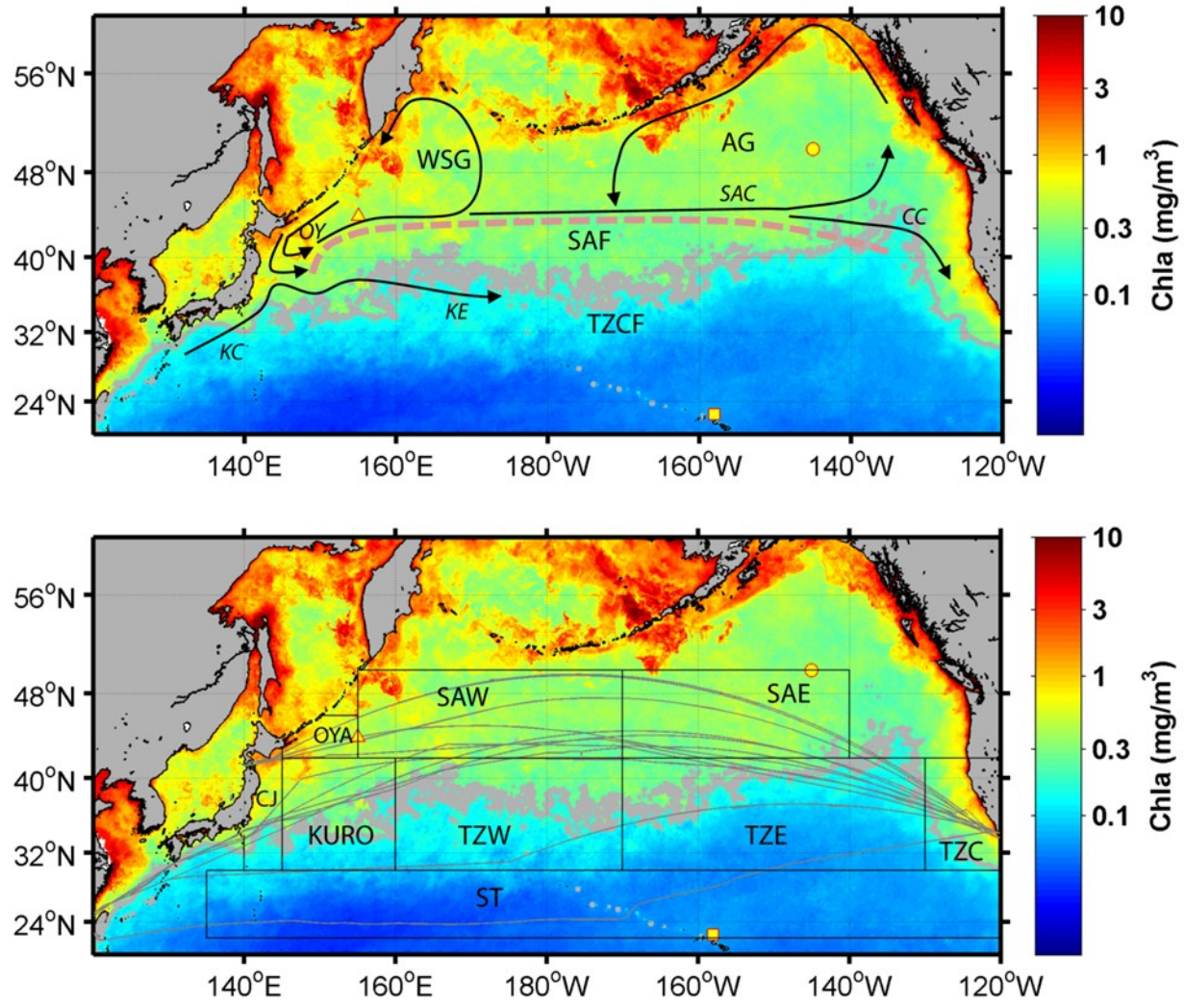

Figure 3.1: Top, general surface circulation of North Pacific (adapted from Chierici *et al*. 2006 and Yasuda, 2003) overlain on satellite chl-a composite for 2009 (MODIS 9-km). Currents (in italics): *OY*, Oyashio Current; *KC*, Kuroshio Current; *KE*, Kuroshio Extension; *SAC*, Subarctic Current; *CC*, California Current. Regions: WSG, Western Subarctic Gyre; AG, Alaska Gyre; SAF, Subarctic Front. Yellow symbols are time series stations: KNOT, triangle; OSP, circle; HOT, square. Gray outline, TZCF. Bottom, cruise tracks and provinces overlain on satellite chl-a composite for 2009. Provinces: OYA, Oyashio; KURO, Kuroshio; SAW, subarctic west; SAE, subarctic east; TZW, transition zone west, TZE, transition zone east; TZC, transition zone coastal; ST, subtropics. Time series stations are as in top panel. Gray outline, TZCF.

In comparing the western and eastern subarctic gyres, a "west high, east low" (WHEL) paradigm has been used to describe trends in physical dynamics, nutrients and new production across the basin. The western subarctic has a much larger seasonal amplitude in *SST*, pCO_2, *DIC*,

nutrients and mixed layer depth (*MLD*) than the eastern subarctic [Harrison *et al*., 1999, 2004; Goes *et al*., 2004, 2004a, Takahashi *et al*. 2002, 2009; Wong *et al*., 2002]. *NCP* in the western North Pacific is ~2x greater than that in the eastern basin based on shipboard and satellite observations [Honda *et al.*, 2003; Goes *et al*, 2004; Kawakami *et al*., 2007; Table 3.1] and sediment trap data [Honda, 2002]. This has been attributed to a combination of (i) higher wind speeds in the west leading to deeper winter MLDs and hence greater vertical supply of nutrients to the mixed layer in winter [Goes *et al*., 2004, 2004a; Glover *et al.*, 1994] and (ii) higher supply of the micronutrient iron due to dust from the Asian continent [Duce and Tindale, 1991; Suzuki *et al.*, 2002]. However, nitrate is never fully drawn down during the growing season across the entire subarctic Pacific [Goes *et al*., 2004], and both the WSG and AG are high nitrate low chlorophyll regions where PP is iron limited [Harrison *et al*., 2004].

Despite greater *NCP* in the western versus eastern basin, annual net primary production (NPP, or GPP minus autotrophic respiration) based on ^{13}C uptake incubations at Station KNOT has been found to be ~2x lower than at OSP and at subtropical stations HOT and BATS (Honda [2003]; Imai *et al*. [2002]). At KNOT, NPP peaks in spring but declines in summer, possibly due to iron limitation [Harrison *et al*., 2004]. Diatoms are plentiful in this spring bloom, with succession of picoeukaryotes and Synechococcus in summer (Liu *et al.*, 2004). In contrast, there is no spring bloom in the AG, and phytoplankton are dominated by small cells of <5 μm [Harrison *et al*., 2004]. Wong *et al*. [2002] found evidence through nutrient ratios of higher phytoplankton composition by diatoms in the WSG versus the ESG.

The subarctic is delineated from the transition zone by the subarctic front, with high meridional change in salinity and temperature (salinity 33–33.8; Roden, 1991; Yuan and Talley, 1996). In the western transition zone east of Japan, the Oyashio and Kuroshio currents converge,

forming a dynamic interfrontal region of mesoscale eddies (cold-core and warm-core rings, 35–40° N, 140–160° E; Yasuda, 2003) with strong influence on PP in this region, including large spring diatom blooms [Kusakabe *et al*. 2002; Isada *et al.*, 2009]. This region also has some of the deepest winter MLDs in the North Pacific (>200 m, Ohno, 2009).

Within the transition zone, the transition zone chlorophyll front (TZCF) is a seasonally migrating, basin-wide feature of sharp northward increase in chlorophyll thought to result from the convergence of cold, high-chlorophyll, nutrient-rich subarctic water sinking under warm, stratified subtropical water low in chlorophyll and nutrients [*Polovina et al.*, 2001; Figure 3.1]. Defined by the 0.2 mg m^{-3} chlorophyll isopleth, its position shifts seasonally from 30–35º N in winter to 40–45º N in summer, and is considered a biological hotspot because it attracts populations of zooplankton, jellyfish, loggerhead turtles, albacore tuna and flying squid that seasonally migrate to follow the meridional location of the front [*Polovina et al.*, 2001].

Several hypotheses have attempted to explain the seasonal migration of the TZCF. *Polovina et al*. [2001] hypothesize that the convergent frontal dynamics of the transition zone concentrate biomass and allow buoyant organisms to regulate their position. Modeling studies have explained its migration through seasonal changes in vertical mixing and nutrient supply [*Glover et al.*, 1994; *Chai et al.*, 2003]. In contrast, others have found that wintertime position of the TZCF corresponds to the region of maximum wind stress curl [*Bograd et al., 2004*] and the southernmost extent of Ekman convergence of nitrate flux, suggesting that its location is controlled by lateral delivery of nutrients, as the nitracline is too deep in this region to impact nutrient supply by vertical mixing [*Ayers and Lozier*, 2010].

The subtropical gyre is a low-nutrient, low-chlorophyll region with lower seasonal variability in temperature, wind speed, productivity and light than in the subarctic gyre; mixed

layer depth ranges from 40 m in summer to 100 m in winter [Karl, 1999; Keeling *et al.*, 2004]. Prochlorococcus is the dominant photoautotroph, but N_2 fixation by other cyanobacteria may provide up to half the nitrogen responsible for export [Karl *et al.*, 1997, 2001].

3.2.2 Previous estimates of NCP in the North Pacific

NCP in the North Pacific has been estimated by shipboard observations including mass balances of dissolved gases (O_2, Ar and N_2), NO_3, DIC, and $\delta^{13}C\text{-}DIC$; the in situ O_2/Ar method; the ^{234}Th method; and ^{15}N and ^{13}C uptake (results and studies cited in Table 3.1), as well as by satellite-based estimates [Falkowski *et al*., 1998, Goes *et al*., 2004; Westberry *et al.*, 2012] and inverse models [Schlitzer 2000, 2004; Louanchi and Najjar, 2000; Lee, 2001; Sasai and Ikeda, 2003]. Observational estimates of *NCP* in the western subarctic Pacific are generally higher and more spatially variable than in the eastern subarctic, with especially high *NCP* along the western boundary of the basin (e.g., Oyashio region (OYA), Table 3.1). Satellite studies [Goes *et al.*, 2004; Table 3.1] and most modeling studies cited above show a similar trend, although Schlitzer *et al*. [2004] found higher *NCP* in the eastern subarctic Pacific due to high rates along the northwestern coast of North America.

At KNOT (44° N, 155° E), annual *NCP* has been estimated at 3.2 mol C m^{-2} yr^{-1}, with seasonal rates of 2–50 mmol C m^{-2} d^{-1} that peak in spring and are lowest in winter (Table 3.1). However, because KNOT is on the southwestern edge of the WSG, it may not be representative of the gyre [Harrison *et al*.; Goes *et al*., 2004]. Elsewhere in the WSG, observational estimates of *NCP* range 2.6–6.3 mol C m^{-2} yr^{-1} with a similar seasonal pattern to that at KNOT (Table 3.1). Especially high *NCP* has been estimated in the region influenced by the nutrient-rich

Oyashio current (~42–45° N, 140–160° E), with annual *NCP* of 6.1–6.9 mol C m^{-2} yr^{-1} and spring-summer rates of 9–102 mmol C m^{-2} d^{-1} (Table 3.1).

In contrast, estimates of annual *NCP* in the eastern subarctic Pacific are substantially lower. At OSP (50° N, 145° W), various studies have estimated annual *NCP* at 2.0 ± 0.3 mol C m^{-2} yr^{-1} and spring-summer rates of 14 ± 5 mmol C m^{-2} d^{-1} (Table 3.1). Elsewhere in the eastern subarctic Pacific, *NCP* rates are similar at 2–3 mol C m^{-2} yr^{-1}.

There are fewer observations in the transition zone. In the western transition zone, the Kuroshio region east of Japan (KURO) has higher daily rates (2–87 mmol C m^{-2} d^{-1}, with highest values in spring-summer and lowest in winter) than in the rest of the western transition zone (3–15 mmol C m^{-2} d^{-1}), but annual *NCP* is similar in both regions at 2–3 mol C m^{-2} yr^{-1} (Table 3.1). Annual and daily *NCP* rates in the eastern transition zone are similar to the western transition zone at ~3 mol C m^{-2} yr^{-1} and 3–21 mmol C m^{-2} d^{-1}, respectively (Table 3.1). In a larger region of the western North Pacific that includes both the western transition zone and subtropics (5–45° N, 130–190° lon), Feely *et al.* [2004] found very high rates of apparent oxygen utilization (4.5 μmol O_2 kg^{-1} yr^{-1}) compared with other regions of the North Pacific, implying a higher export flux of carbon. They calculated a organic carbon remineralization rate of 3.1 μmol C kg^{-1} yr^{-1} in this region as opposed to 2.6 μmol C kg^{-1} yr^{-1} in the corresponding region in the eastern basin.

In the subtropics, annual *NCP* rates are similar at 2–3 mol C m^{-2} yr^{-1} to those in the transition zone and eastern subarctic. At ALOHA in the eastern subtropics, annual *NCP* is 2.7 ± 0.9. Spring-summer rates are lower than in the subarctic at 3–15 mmol C m^{-2} d^{-1}, but daily rates are relatively constant over the annual cycle at 5–12 mmol C m^{-2} d^{-1} (Table 3.1).

3.2.3 Previous estimates of the influence of NCP on air-sea CO_2 flux in the North Pacific

Previous investigations of the processes controlling the oceanic sink for atmospheric CO_2 have examined the impacts of temperature (through CO_2 solubility) and biological (through NCP) and physical effects (through DIC supply) on air-sea CO_2 flux. Takahashi *et al*. [2002] attributed the strong atmospheric CO_2 sink in the North Pacific to a combination of temperature effects (caused by warm subtropical water moving northward and cooling, increasing its capacity to absorb CO_2) and biological uptake through *NCP*.

However, recently Ayers and Lozier [2012] reframed this approach to make a distinction between processes controlling seasonal variation in surface ocean pCO_2 (as studied by Takahashi *et al*., 2002) and processes controlling the net annual oceanic sink for atmospheric CO_2. Based on a mixed layer *DIC* budget, Ayers and Lozier estimated that over the annual cycle in the North Pacific transition zone, the net annual effect of temperature on the CO_2 sink is relatively minor (~17%), because the summer warming–induced pCO_2 increase is nearly balanced by a winter cooling–induced pCO_2 decrease in this region. They found that the main processes controlling the net annual atmospheric CO_2 sink in the North Pacific transition zone are *NCP* and geostrophic divergence of DIC, which make equal contributions to decreasing mixed layer pCO_2 over the annual cycle (–111 μatm yr^{-1} and –113 μatm yr^{-1}, respectively).

When Ayers and Lozier's results are separated into biological (*NCP*) and physical terms, the supply of *DIC* due to Ekman transport, vertical advection (entrainment) and mixing outweighs the removal of *DIC* by geostrophic transport and yields a net physical supply of 59 μatm pCO_2 in the mixed layer over the annual cycle. This pCO_2 increase is equivalent the net annual increase of pCO_2 due to air-sea CO_2 flux calculated by Ayers and Lozier in this region

(61 μatm yr^{-1}). Therefore, the analysis yields annual ratios of *NCP*:physical supply:CO_2 influx for the *DIC* budget in the North Pacific transition zone of –2:1:1.

A DIC modeling analysis over the North Pacific subarctic and transition zone (30–55º N, 130° E–120° W) by Sasai and Ikeda [2003] found a net annual *NCP*:physical supply:CO_2 influx ratio of –3:2:1. In the subarctic North Pacific, where annual CO_2 influx is lower than in the North Pacific transition zone, Chierici *et al*. [2006] found (through a pCO_2 modeling analysis) ratios of NCP:air-sea CO_2 influx of about –5:1 in the Western subarctic gyre and –2:1 in the Alaska gyre. In the subtropical North Pacific at Station ALOHA, using a mixed layer DIC-$\partial^{13}C$ budget approach, Quay and Stutsman [2003] and Keeling *et al*. [2004] found annual *NCP*:physical supply:CO_2 influx ratios of –3:2:1 and –2:1:1, respectively.

In summary, throughout the North Pacific, previous estimates suggest that *NCP* annually removes CO_2 at 2–5x the rate of atmospheric CO_2 influx. In the subarctic, where atmospheric CO_2 influx is relatively low at ≤1 mol C m^{-2} yr^{-1} (Takahashi et al., 2009), NCP:CO_2 influx ratios are largest at –2:1 to –5:1. In the transition zone, where atmospheric CO_2 influx is generally highest (~2–3 mol C m^{-2} yr^{-1}) *NCP*:CO_2 influx ratios are lower at –2 to –3:1. In the subtropics, where atmospheric CO_2 influx is low at ≤1 mol C m^{-2} yr^{-1}, the NCP:CO_2 influx ratio is similar to that found in the transition zone (–2 to –3:1). One can view annual air-sea CO_2 flux in a region as a result of the imbalance between two opposing processes, *DIC* supply by physical processes and its removal by *NCP*. In the North Pacific transition zone, this imbalance is greater than in either the subarctic or the subtropical regions.

3.2.4 O_2/Ar method for estimating NCP

The saturation level of the O_2/Ar gas ratio in the mixed layer coupled with air-sea gas exchange rate yields quantitative estimates of *NCP* that are mostly insensitive to nonbiological gas saturation processes (e.g., warming, bubble injection) because argon is an inert analog of oxygen, as described previously [*Craig and Hayward*, 1987; *Emerson et al.*, 1991, 1997].

Briefly, the biological O_2 supersaturation, which quantifies the influence of *NCP* on the O_2 budget, is defined as:

$$\Delta\frac{O_2}{Ar} = \frac{\left[\frac{O_2}{Ar}\right]_{\mathrm{msr}}}{\left[\frac{O_2}{Ar}\right]_{\mathrm{sat}}} - 1 \tag{3.1}$$

where $[O_2/Ar]_{\mathrm{msr}}$ is the measured dissolved O_2/Ar gas ratio, and $[O_2/Ar]_{\mathrm{sat}}$ is the ratio expected at saturation with air (based on temperature and salinity dependence of O_2 and Ar solubility; *Garcia and Gordon*, 1992; *Hamme and Emerson*, 2004]. The percent biological O_2 supersaturation ($\%O_{2bio}$) equals ($\Delta O_2/Ar$)*100.

NCP is calculated using O_2 and Ar mass balances for the mixed layer (see Howard *et al*. [2010] for complete derivation). When assuming steady state and negligible physical supply, this yields:

$$NCP = k_{\mathrm{O2}}[O_2]_{\mathrm{sat}}\frac{\Delta O_2}{Ar} \tag{3.2}$$

where k_{O2} is the gas transfer velocity of O_2 (m d^{-1}) and $[O_2]_{\mathrm{sat}}$ is the concentration of O_2 at saturation (mol m^{-3}) [*Garcia and Gordon*, 1992].

We determined k_{O2} using winds from QuikScat and NCEP (for cruises after 2009), the *Ho et al*. [2006] wind speed parameterization using a 30-day time-weighting technique [*Reuer et al.*, 2007], and the temperature- and salinity-dependent Schmidt number [*Wanninkhof*, 1992]. To convert O_2-based *NCP* to *C*-based *NCP*, we used a ratio of 1.45 O_2: 1 *C* (export or new production) [*Laws et al.*, 1991; Anderson and Sarmiento, 1994]. This estimate of *NCP* integrates

over the residence time of O_2 in the mixed layer (i.e., $(MLD)/k_{O2}$), which varied from ~1 week to ~1 month during our cruises, with longer residence times in winter.

3.3 Methods

3.3.1 Underway and discrete sampling and cruise tracks

We continuously measured surface O_2/Ar, pCO_2, temperature and salinity from the underway system of the Orient Overseas Container Line (OOCL) Tianjin or the OOCL Tokyo on 13 cruises between Hong Kong and Long Beach, California, across the North Pacific in 2008–2011; Figure 3.1). The typical cruise duration was 12 days. Temperature and salinity were measured using a TSG. Concentrations of nitrate, phosphate and silicate were determined on discrete surface samples collected from the underway flow in the University of Washington Marine Chemistry Laboratory using standard methods [*UNESCO*, 1994]. *MLD* was determined using two data sources, the Argo float–based monthly average data from Japan Agency for Marine-Earth Science and Technology (JAMSTEC; http://www.jamstec.go.jp/ARGO/argo_web/MILAGPV/index_e.html; Hosoda *et al.* 2010) and monthly average data from the high-resolution Fleet Numerical Meteorology and Oceanography Center (FNMOC) model available from Oregon State University (http://orca.science.oregonstate.edu/1080.by.2160.monthly.hdf.mld.merge.php). As the JAMSTEC data were not available for large portions of our cruise tracks, we use the FNMOC data when making comparisons among regions.

3.3.2 Continuous O_2/Ar measurements using EIMS

We continuously measured surface O_2/Ar using an EIMS system similar to that described in *Cassar et al.* [2009]. Water from the ship's underway line was pumped at ~2 L min^{-1} through a coarse filter to screen out particulates into a 1 L graduated cylinder on which the equilibrator cartridge (Membrana MicroModule G569, 0.75" x 1") was mounted. Water from the graduated cylinder was pumped through a 5 μm filter sock sewed inside a 100 μm filter sock (1.5" x 12", McMaster-Carr), and then through the cartridge at ~100 ml min^{-1}. To prevent biofouling, the coarse filter was cleaned and the sock filter was replaced daily, and the equilibrator cartridge was replaced weekly. All tubing used was Tygon silver (antimicrobial).

Headspace gas from the equilibrator was delivered through an 0.05 mm fused silica capillary to the quadrupole mass spectrometer (Pfeiffer Prisma QMS), which was kept at a constant temperature (40° ± 2° C). Individual ion currents (O_2, Ar) were measured at 1-second intervals, and the ratio of O_2/Ar currents was averaged to a 10-minute timescale. The EIMS system e-folding response time is 7 min [*Cassar et al*., 2009], yielding a spatial resolution of ~4 km at the average ship speed of 20 knots.

EIMS-based O_2/Ar measurements were calibrated using the O_2/Ar of air measured by the EIMS, and O_2/Ar measured by isotope ratio mass spectrometer (IR-MS) on discrete samples collected from the underway line approximately every 6 hours following the collection procedures of *Emerson et al.* [1995] and mass spectrometer procedures of *Juranek and Quay* [2005] in the University of Washington Stable Isotope Lab. The percent error ([s.d./mean]*100) in O_2/Ar of discrete air standards used for IR-MS calibration was 0.2% and that of duplicate samples was 0.2%.

Both OOCL ships have an anticorrosive system in the sea chest to prevent biofouling. To further prevent biofouling in the underway line, we filled the Tygon lines between the intake and

sampling area with bleach for 2–4 hours at the start of each cruise, then purged them with freshwater and flushed with seawater for at least 1 hour before sampling began. At the end of each cruise, the Tygon lines between the intake and sampling area, as well as all sampling tubing to the pCO_2 and MIMS systems, were flushed and filled with freshwater and remained filled during the time between cruises. The O_2/Ar of discrete samples measured close to the intake (on the inside wall) of the ship's underway line and our sampling location compared well (0.3% error), showing no evidence of O_2 consumption in the underway line.

We estimated error in *NCP* using a Monte-Carlo approach assigning uncertainty in the following terms: $k_{O2} \pm 15\%$ (twice the spread in k_{O2} values predicted by three parameterizations recently validated by *Ho et al.* [2011]: *Nightingale et al.* [2000], *Ho et al.* [2006], and *Sweeney et al.* [2007]) and $O_2/Ar \pm 0.1\%$ (mean in offset between EIMS and discrete samples). Mean *NCP* percentage error ([s.d./mean]*100) varied regionally; it was highest in the subtropics (ST, 81%), SAW (49%) and TZC (40%), and was <35% elsewhere (see Table 3.5).

3.3.3 Measurements of pCO_2 and estimate of CO_2 flux

We continuously measured the pCO_2 in surface water from the ship's underway line and air from the bow with an automated IR-detection-based underway pCO_2 measuring system that has been described in detail elsewhere [*Feely et al*., 1998; *Pierrot et al*., 2009]. We calculated the air-sea pCO_2 gradient (ΔpCO_2) as $\Delta pCO_2 = pCO_{2SW} - pCO_{2atm}$, where pCO_{2SW} is the calculated pCO_2 of the seawater (after correction for water temperature difference between in situ and the pCO_2 equilibrator) and pCO_{2atm} is the measured atmospheric pCO_2. After correction, the accuracy of the data is within 0.1 μatm for pCO_{2atm} and 2 μatm for pCO_{2SW} [*Pierrot et al.*, 2009], and the

equilibrator integration time is 30–45 s. pCO_2 data were averaged to match the 10-minute integration time of the EIMS data.

The air-sea flux of CO_2 is calculated based on ΔpCO_2 and the solubility (k_H) [*Stumm and Morgan*, 1996] and gas transfer velocity of CO_2 (k_{CO2}):

$$CO_2\ flux = k_{CO2}\, k_H\, \Delta pCO_2 \tag{3.3}$$

Defined in this way, *CO_2 flux* from the atmosphere into the ocean (influx) is negative, and efflux is positive. k_{CO2} was calculated as described above for k_{O2} using the Ho *et al.* [2006] wind speed parameterization with time-weighting [*Reuer et al.*, 2007], and the Schmidt number for CO_2 [*Wanninkhof*, 1992].

3.3.4 Climatological box model of O_2 and Ar budgets

To estimate the influence of physical processes (circulation, entrainment, and mixing) on the *O_2/Ar* mixed layer budget, we constructed a mixed layer box model based on data from the 1º latitude x 1º longitude monthly climatology of World Ocean Atlas 2009 [Garcia *et al.* 2010] including O_2, $\%O_{2sat}$, temperature and salinity at standard depth levels. We determined mixed layer values of these parameters by averaging samples within the monthly climatological mixed layer (based on monthly climatology of MLD in density with a variable density criterion, de Boyer Montegut, 2004, 2007; Mignot *et al.*, 2007; Table 3.2).

Table 3.2: Data sources for climatological O_2 and O_2/Ar box models

Parameter	Data source	Spatial resolution (latitude x longitude)	Temporal resolution	Websites and references
O_2 (μmol kg^{-1}), %O_{2sat}, temperature (°C), and salinity	World Ocean Atlas 2009	1° x 1° (at standard depths)	Monthly climatology	http://www.nodc.noaa.gov/OC5/WOA09/woa09data.html Garcia *et al*. [2010]
Ekman transport (kg m^{-1} s^{-1}) and D_{Ek} (m)	FNMOC wind and Ekman transport data, from 6-hr pressure	1° x 1°	Monthly climatology 1997–2012	http://coastwatch.pfeg.noaa.gov/erddap/griddap/erdlasFnWPr.html
Geostrophic velocity (m s^{-1})	Ssalto/Duacs, distributed by Aviso, delayed-time	1/3° x 1/3°, regridded to 1° x 1°	Monthly climatology 1993–2007	http://www.aviso.oceanobs.com/en/data/products/sea-surface-height-products/global.html
Wind speed (m s^{-1}) and SST (°C)	SCOW (Scatterometer climatology of ocean winds) from QuikScat data	1/4° x 1/4°, regridded to 1° x 1°	Monthly climatology 1999–2009	http://cioss.coas.oregonstate.edu/scow/ Risien and Chelton [2008]
Mixed layer depth (m)	deBoyer Montégut MLD in density with a variable threshold criterion (equivalent to a 0.2° C decrease), level 3 gridded	2° x 2°	Monthly climatology	http://www.ifremer.fr/cerweb/deboyer/mld/Surface_Mixed_Layer_Depth.php de Boyer Montégut *et al*. [2002, 2007]; Mignot *et al*. [2007]

The mass balance of O_2 in the mixed layer is described by:

$$\partial O_{2ML}/\partial t = F_{Gasex} + F_{Ek} + F_{Geo} + F_{Ent} + F_{Vdiff} + F_{Bub} + F_{NOP} \quad (3.4)$$

where F_{Gasex} is the flux of oxygen due to gas exchange, F_{Ek} is the convergence of O_2 in the mixed layer due to horizontal Ekman transport, F_{Geo} is the convergence of O_2 in the mixed layer due to geostrophic transport, F_{Ent} is the flux of O_2 due to entrainment, F_{Vdiff} is the flux due to vertical diffusive mixing at the base of the mixed layer, F_{Bub} is the flux of oxygen due to bubble entrainment from breaking waves, and F_{NOP} is the flux of oxygen due to net oxygen production (via *NCP*). We assumed that F_{Bub} was negligible, as it is a small term in most regions, and current parameterizations have large uncertainty [Stanley *et al*., 2009]; however, it has been found to be a significant term in the O_2 mass balance in the subtropics (at ALOHA) [Emerson *et al.*, 1995] and in wintertime in the Alaska gyre (at OSP) and when wind speeds are high and O_2 supersaturation is low [Emerson and Stump, 2010]. We parameterized the remaining terms as follows:

$$F_{Gasex} = \frac{1}{h} k_{O2}(O_{2sat} - O_{2ML}) \quad (3.5)$$

where h is the climatological MLD and k_{O2} was calculated with the Ho *et al*. [2006] parameterization based on the monthly Scatterometer Climatology of Ocean Winds (SCOW) derived from QuikScat data (Table 3.2; Risien and Chelton, 2008) and the Schmidt number for O_2 calculated from the monthly SST climatology of the SCOW data set.

The convergence of O_2 in the mixed layer due to horizontal Ekman transport was calculated as:

$$F_{Ek} = (-\nabla \cdot \boldsymbol{u_{HEk}} O_{2ML}) \quad (3.6)$$

where and ∇ is the divergence operator, defined horizontally for the concentration of any species C as:

$$\nabla \cdot \boldsymbol{u}C = u\frac{\partial C}{\partial x} + v\frac{\partial C}{dy} \quad (3.7)$$

Northward and eastward horizontal Ekman velocity (u_{HEk} and v_{HEk}, respectively) were calculated based on a monthly 1º latitude x 1º longitude climatology of Ekman transports (kg m^{-1} s^{-1}) derived from FNMOC synoptic surface pressure analyses at six-hour intervals (Table 3.2), and horizontal gradients in O_2 were determined from the World Ocean Atlas climatological data. We calculated the depth of the Ekman layer (D_{Ek}) using $D_{Ek} = \frac{7.6}{\sqrt{sin|\varphi|}} u_{10}$ where φ is latitude in radians and u_{10} is wind speed at 10 m above the surface (using corresponding FNMOC data). In cases where the climatological $MLD < D_{\mathrm{Ek}}$, we considered only the transport in the mixed layer (by multiplying total transport by MLD/D_{Ek}).

The convergence of O_2 in the mixed layer due to horizontal geostrophic transport was similarly calculated as:

$$F_{Geo} = (-\nabla \cdot \boldsymbol{u_{Geo}} O_{2ML}) \quad (3.8)$$

Northward and eastward horizontal geostrophic velocity (u_{Geo} and v_{Geo}, respectively) were calculated based on a monthly 1/3° latitude x 1/3° longitude climatology derived from Ssalto/*Duacs* gridded absolute geostrophic velocities (regridded to 1° latitude x 1° longitude; Table 3.2).

The entrainment of O_2 in the mixed layer was calculated as:

$$F_{Ent} = \frac{1}{h} \, \Xi \, \frac{\partial h}{\partial t} \, (O_{2\mathrm{TC}} - O_{2\mathrm{ML}}) \tag{3.9}$$

where $O_{2\mathrm{TC}}$, representing O_2 in the thermocline, was assigned the value of O_2 in the first depth interval below the climatological *MLD* (on average 25 m below the *MLD*). $\partial h/\partial t$ was calculated based on the monthly change in climatological *MLD*; Ξ indicates that $F_{\mathrm{ent}} = 0$ when the mixed layer is shoaling ($\partial h/\partial t < 0$).

The supply of O_2 to the mixed layer due to vertical diffusive mixing was calculated as:

$$F_{Vdiff} = \frac{1}{h} \, K_z \left(\frac{\partial O_2}{\partial z}\right)_{TC} \tag{3.10}$$

where $\partial O_2/\partial z$ is the gradient between the deepest O_2 measurement in the climatological ML and O_{2TC}, and K_z is the vertical diffusivity coefficient. In the region influenced by the Kuroshio current (30–40° N, 140–175° E), we assumed $K_z = 3 \times 10^{-3}$ m^2 s^{-1} in winter and $K_z = 3 \times 10^{-4}$ m^2 s^{-1} during the rest of the year based on estimates from a heat flux balance study at the Kuroshio Extension Observatory mooring (32.4° N, 144.6° E) [Cronin *et al.*, 2013]. As Cronin *et al*. [2013] estimated wintertime K_z of up to 3×10^{-2} m^2 s^{-1} in this region, we assume our value is conservative (and assign uncertainty of 50% to F_{Vdiff}; see below). Elsewhere in the basin, we

assumed K_z of 3 x 10^{-5} m^2 s^{-1} based on an ocean-wide average of previous studies [Ayers and Lozier, 2012].

We set up a corresponding mass balance for *Ar* in the mixed layer by assuming *Ar* in the mixed layer and at the depth interval below it was at equilibrium with the atmosphere (based on the temperature and salinity of the mixed layer derived from the World Ocean Atlas data set and the solubility relationship of Hamme and Emerson [2004]). As *Ar* has no biological sources or sinks, there is no term for *NCP* in the mass balance:

$$\frac{\partial Ar}{\partial t} = \frac{1}{h} k_{Ar}(Ar_{sat} - Ar_{ML}) + (-\nabla \cdot \boldsymbol{u_{HEk}} Ar_{ML}) + (-\nabla \cdot \boldsymbol{u_{Geo}} Ar_{ML}) + \frac{1}{h} \Xi \frac{\partial h}{\partial t} (Ar_{\mathrm{TC}} - Ar_{\mathrm{ML}}) + \frac{1}{h} K_z \left(\frac{\partial Ar}{\partial z}\right)_{tc} \quad (3.11)$$

To obtain an O_2/Ar budget for comparison with our cruise estimates, we multiplied the *Ar* mass balance (equation (3.11)) by $O_{2\mathrm{sat}}/Ar_{\mathrm{sat}}$, and then subtracted this from the O_2 budget (equation (3.4)). Assuming that the solubilities of the two gases are equal, and assuming steady state conditions, this gives a budget in terms of O_2/Ar (for a full derivation of this approach, see Howard *et al*. [2010]). We refer to the sum of all physical supply terms ($F_{\mathrm{Ek}} + F_{\mathrm{Geo}} + F_{\mathrm{Ent}} + F_{\mathrm{Vdiff}}$) as F_{physO2} for the O_2 model and F_{physO2Ar} for the O_2/Ar model.

To determine the uncertainty in our estimates of F_{physO2} and F_{physO2Ar}, we assumed 25% and 22% error in the mean for F_{Ek} and F_{Geo}, respectively, based on a previous modeling study [Ayers and Lozier, 2012], and 50% error in the mean for F_{Vdiff} (M. Cronin, personal communication). For F_{Ent}, we assumed percentage error equal to (s.d./mean)*100 of climatological *MLD* values in each province; this ranged 12–30% regionally, with the largest error in the coastal provinces (TZC and CJAP).

We also tested how sensitive the O_2/Ar model was to our assumption that Ar was at atmospheric equilibrium. Examining available data sets at KNOT and HOT (hosted on the website of Roberta Hamme; http://web.uvic.ca/~rhamme/download.html), we found that in the western subarctic at KNOT, the saturation state of Ar ($\%Ar_{sat}$) in the mixed layer ranges from –1% to +4% over the annual cycle, and is correlated with temperature (T), which ranges 2–15 °C over the year ($\%Ar_{sat} = 0.3165(T) – 1.2194$ for T in °C; $R^2 = 0.57$). At the first depth measurement below the mixed layer at KNOT (representing the depth used in our model to calculate F_{ent} and F_{Vdiff}), $\%Ar_{sat}$ was also correlated with temperature, with a greater slope and R^2 than in the mixed layer ($\%Ar_{sat} = 0.692T – 1.5882$; $R^2 = 0.95$). In contrast, at subtropical station HOT, where temperature in the mixed layer has a much smaller annual range (23–26 °C), $\%Ar_{sat}$ ranged only –0.1% to 0.7% and was not significantly correlated with temperature.

Thus, for a more realistic Ar model, we also calculated Ar_{ML} (and at the depth level below the mixed layer) based on the relationships of temperature and saturation state found at KNOT. We applied this relationship in our model in the region north of 40° N, and assumed Ar_{ML} (and at the depth level below the mixed layer) to be at atmospheric equilibrium elsewhere. Using this modified model to correct NOP_U for physical inputs did not yield substantially different NOP_C from that obtained using the original model in which we assumed Ar was at saturation (regional average differences were 4–19%). Thus for simplicity we present the results of the original model in which we assumed Ar was at saturation.

3.4 Results and Discussion

3.4.1 Cruise regions

We determined regional mean values of our cruise data by averaging all values for each cruise within the provinces defined in Figure 3.1. In the subarctic, we consider three provinces, the region off Hokkaido influenced by the Oyashio current (OYA, 42–46° N, 145–155° E), the Subarctic West (SAW, 42–50° N, 155–190°, which includes the southern part of the WSG and the central subarctic Pacific) and the Subarctic East (SAE, 42–50° N, 190–220°, which includes the southern part of the AG). In the transition zone, we consider the coastal region east of Japan (CJ, 30–45° N, 140–145° E), the open ocean region influenced by the Kuroshio current (KURO, 30–42° N, 145–160° E), the Transition Zone West (TZW, 30–42° N, 160–190°), the Transition Zone East (TZE, 30–42° N, 190–230° lon), and the coastal transition zone off California (TZC, 30–42° N, 230–240°). We classify the subtropics (ST) as 20–30° N, 135–240° lon.

In sections 3.4.2–3.4.4 below, we present our cruise results of *NCP* derived from equation (3.2), which assumes that the O_2/Ar budget is not influenced by physical inputs (circulation, entrainment and mixing). As physical inputs likely influence the budget (especially in fall and winter), we refer to these values below as uncorrected net oxygen production, or NOP_U, in units of mmol O_2 m^{-2} d^{-1}. Then, in section 3.4.5, we use the physical terms of our climatological O_2/Ar budget to correct these values for the influence of physical processes and derive a corrected *NOP* (NOP_C). We then convert this NOP_C to *NCP* in carbon units using a photosynthesis quotient (1.45; Anderson and Sarmiento, 1994).

3.4.2 Winter cruises

In winter, *SST*, salinity, density and *MLD* in the subarctic and transition zone were much more spatially variable in the western basin than in the east, with sharp gradients indicating frontal features and/or eddies (Figure 3.2). In contrast, these indices were much less variable in the

subtropics, where *SST* and salinity were substantially higher. *MLD* was generally greater in the western subarctic and transition zone (most regional means >100 m) than in the corresponding eastern regions and the subtropics (most regional means ≤80 m; Table 3.3.1). *MLD* derived from Argo floats indicated very high values (>300 m) in the western boundary provinces (CJ and OYA) in February. k_{O2} was especially high (>10 m d^{-1}) in KURO and TZW in January, and in CJ in February, but otherwise was generally ~4–8 m d^{-1} across the basin.

In the western basin (subarctic and transition zone), biological O_2 was generally undersaturated, with the greatest undersaturation at 140°–160° E (CJ, OYA and KURO; Figure 3.3 and Table 3.3.1). This led to substantially negative uncorrected *NOP* (NOP_U) at mean regional rates of –31 to –105 mmol O_2 m^{-2} d^{-1} in these regions (Table 3.3.1). In contrast, biological O_2 was generally supersaturated in the eastern basin (subarctic and transition zone) and in the subtropics, leading to regional mean NOP_U of 1–12 mmol O_2 m^{-2} d^{-1} (Table 3.3.1).

pCO_2 was undersaturated throughout most of the basin in winter, with regions of strong undersaturation in the western transition zone (KURO and TZW; Figure 3.3). Accordingly, regional mean CO_2 influx was greater in these provinces (10–17 mmol C m^{-2} d^{-1}) than in the TZE and SAE (7–10 mmol C m^{-2} d^{-1}; Table 3.3.1). In the subtropics and TZC, pCO_2 was less strongly undersaturated and mean CO_2 influx was small (3–6 mmol C m^{-2} d^{-1}). ΔpCO_2 and CO_2 flux showed similar zonal trends across two cruises that crossed the transition zone a year apart (January 2009 and December 2009; Figure 3.3 and Table 3.3.1).

On both cruises in which we measured nitrate (one in the transition zone and one in the subarctic) nitrate was generally greater in the west than in the east. Nitrate was ~4x times higher in the subarctic than in the transition zone. Nitrate was low or undetectable in CJ, KURO and in the TZE east of ~210–220° lon.

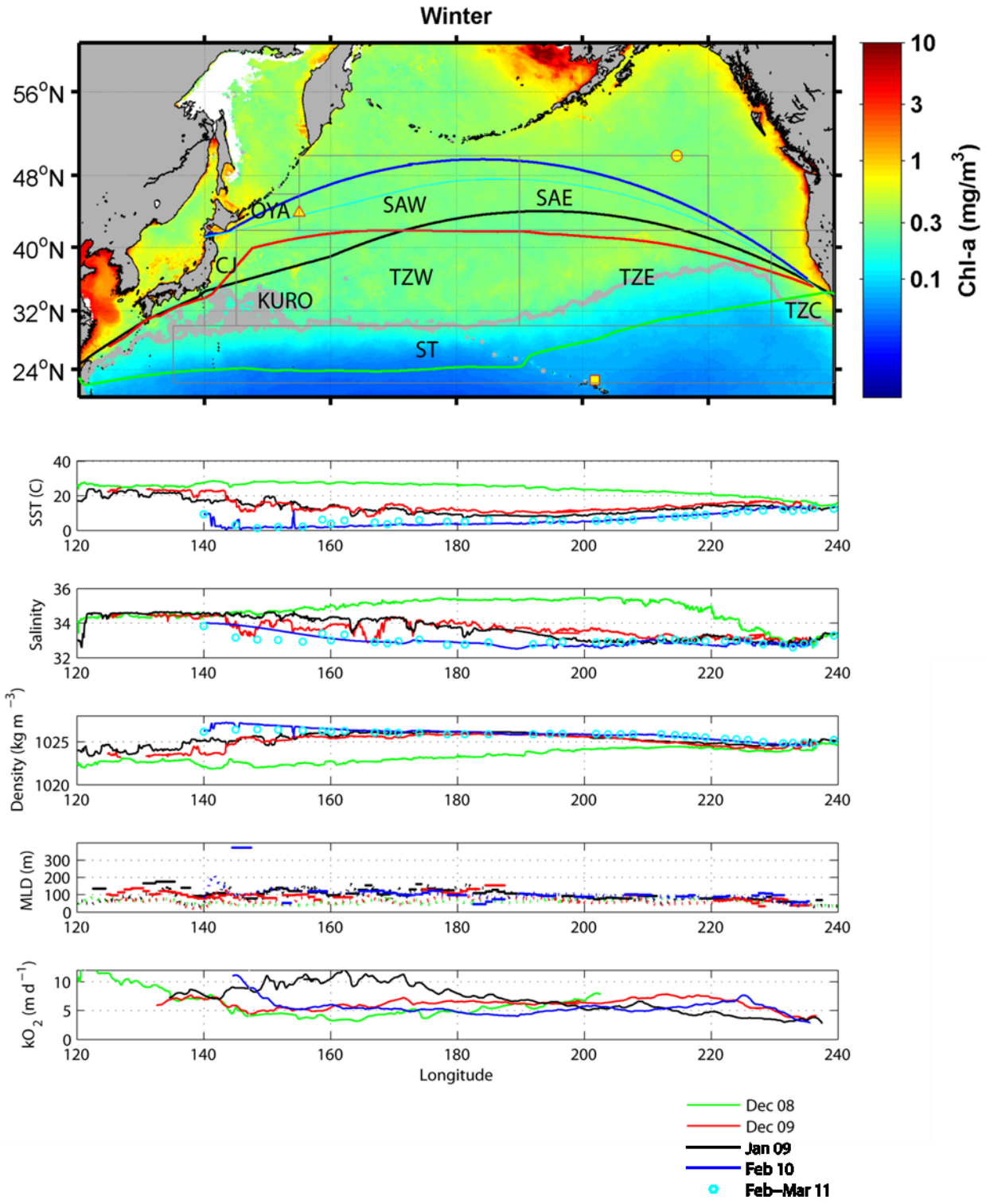

Figure 3.2: Top, winter cruise tracks overlain on climatological winter chl-a (MODIS 9-km). Below, winter SST, salinity, density, MLD, and k_{O2}. For MLD, solid line is from Jamstec (Argo-based) and dashed line is from FNMOC.

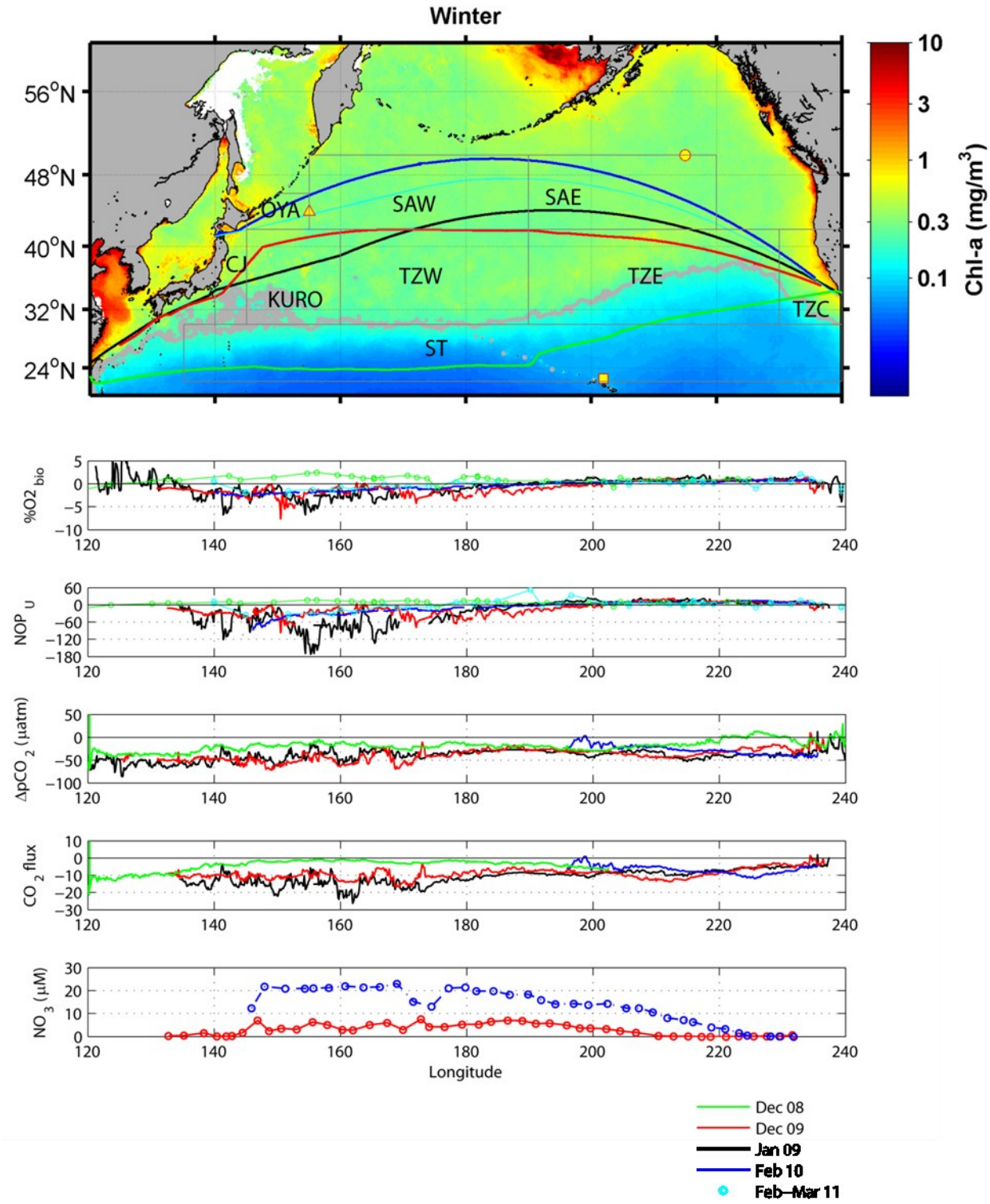

Figure 3.3: Top, winter cruise tracks overlain on climatological winter chl-a (MODIS 9-km). Below, winter $\%O_{2bio}$, uncorrected *NOP* (NOP_U, mmol O_2 m^{-2} d^{-1}), ΔpCO_2, CO_2 flux (mmol C m^{-2} d^{-1}), and nitrate (µM).

Table 3.3.1: Winter cruise results

Regional mean and s.d. of SST (°C), density (kg m^{-3}), MLD (m) from FNMOC (OSU) or gridded Argo data (Argo), k_{O2} (m d^{-1}), NOP_U (mmol O_2 m^{-2} d^{-1}), ΔpCO_2 (µatm), and CO_2 flux (mmol C m^{-2} d^{-1}; negative values indicate flux into the ocean).

	CJ		OYA		SAW		SAE		KURO		TZW		TZE		TZC		ST	
Dec. 2008	*mean*	*s.d.*	*mean*	*s.d.*	*mean*	*s.d.*	*mean*	*s.d.*	*mean*	*s.d.*	*mean*	*s.d.*	*mean*	*s.d.*	*mean*	*s.d.*	*mean*	*s.d.*
SST													20.8	1.3	16.0	1.2	26.0	1.6
Salinity													34.5	0.7	33.1	0.2	35.1	0.4
Density													1024.2	0.2	1024.3	0.4	1023.1	0.7
MLD OSU													74	9	46	10	57	12
MLD Argo																		
k_{O2}																	5.2	1.2
$\%O_{2bio}$													0.8	0.2			1.2	0.8
NOP_U													8	2			10	6
ΔpCO_2													-7	10	-7	10	-20	6
CO_2 flux																	-3	2

	CJ		OYA		SAW		SAE		KURO		TZW		TZE		TZC		ST	
Dec. 2009	*mean*	*s.d.*	*mean*	*s.d.*	*mean*	*s.d.*	*mean*	*s.d.*	*mean*	*s.d.*	*mean*	*s.d.*	*mean*	*s.d.*	*mean*	*s.d.*	*mean*	*s.d.*
SST	20.9	2.6			14.7	0.2			13.2	1.9	11.7	1.6	13.3	2.1	14.5	1.2		
Salinity	34.3	0.2			34.2	0.0			33.7	0.3	33.8	0.3	33.3	0.2	32.9	0.1		
Density	1024.0	0.5			1025.4	0.0			1025.4	0.2	1025.7	0.2	1025.0	0.6	1024.5	0.3		
MLD OSU	65	26			76	2			62	11	72	14	61	10	44	9		
MLD Argo	93	11							93	10	122	23	76	17	54	18		
k_{O2}	6.5	0.7			6.4	0.1			5.1	0.3	6.3	0.4	6.6	0.7	4.0	0.4		
$\%O_{2bio}$	-2.2	0.5			-0.5	0.2			-2.3	1.4	-1.7	0.8	0.3	0.6	0.3	0.8		

NOP_U	-32	5			-9	4			-31	18	-30	15	5	11	3	8		
ΔpCO_2	-51	6			-67	2			-52	9	-38	13	-33	7	-21	10		
CO_2 flux	-10	1			-16	0			-10	2	-10	3	-9	3	-3	2		

	CJ		OYA		SAW		SAE		KURO		TZW		TZE		TZC		ST	
Jan 2009	*mean*	*s.d.*	*mean*	*s.d.*	*mean*	*s.d.*	*mean*	*s.d.*	*mean*	*s.d.*	*mean*	*s.d.*	*mean*	*s.d.*	*mean*	*s.d.*	*mean*	*s.d.*
SST	17.2	0.8			9.1	0.8	9.8	1.5	14.7	2.1	12.1	1.5	13.9	0.6	12.9	0.6		
Salinity	34.5	0.1			33.7	0.2	33.0	0.2	34.4	0.1	34.2	0.2	33.0	0.2	33.0	0.3		
Density	1025.1	0.2			1026.1	0.0	1025.4	0.3	1025.5	0.4	1025.9	0.2	1024.7	0.1	1024.9	0.2		
MLD OSU	104	33			127	14	80	15	109	26	107	25	74	6	42	9		
MLD Argo	105	5			123	15	86	6	114	19	114	18	76	5	62	4		
k_{O2}	7.8	0.7			8.0	1.0	5.8	0.6	9.7	0.8	10.7	0.7	4.0	0.4	3.4	0.2		
$\%O_{2bio}$	-2.6	2.0			-0.9	0.7	0.7	0.4	-2.9	1.4	-2.5	0.9	0.8	0.4	0.4	1.1		
NOP_U	-48	33			-22	18	12	5	-74	39	-74	26	9	4	5	5		
ΔpCO_2	-45	11			-33	5	-36	7	-40	11	-38	9	-41	4	-29	12		
CO_2 flux	-12	3			-12	3	-9	1	-14	4	-16	4	-6	1	-4	1		

	CJ		OYA		SAW		SAE		KURO		TZW		TZE		TZC		ST	
Feb. 2010	*mean*	*s.d.*	*mean*	*s.d.*	*mean*	*s.d.*	*mean*	*s.d.*	*mean*	*s.d.*	*mean*	*s.d.*	*mean*	*s.d.*	*mean*	*s.d.*	*mean*	*s.d.*
SST	4.0	3.3	2.0	1.6	3.0	0.7	6.4	1.7					12.4	0.4	13.1	0.2		
Salinity	34.0	0.0	33.7	0.2	32.9	0.2	32.8	0.1					32.9	0.1	32.7	0.1		
Density	1026.9	0.4	1026.9	0.2	1026.2	0.2	1025.7	0.2					1024.9	0.1	1024.6	0.1		
MLD OSU	144	38	119	13	103	10	91	8					83	4	47	11		
MLD Argo	372	0	272	150	101	24	97	6					104	6	72	19		
k_{O2}	11.1	0.0	7.5	1.9	5.0	0.5	5.3	0.5					6.4	0.8	3.9	0.8		
$\%O_{2bio}$	-2.3	0.3	-2.1	0.2	-1.0	0.5	0.4	0.2					0.7	0.1	0.7	0.1		

***NOP*$_U$**	-105	0	-54	15	-18	10	6	3					12	3	8	1		
ΔpCO_2							-21	8					-39	1	-40	2		
CO_2 flux							-6	2					-10	1	-6	1		

	CJ		**OYA**		**SAW**		**SAE**		**KURO**		**TZW**		**TZE**		**TZC**		**ST**	
Feb-Mar. 2011	*mean*	*s.d.*	*mean*	*s.d.*	*mean*	*s.d.*	*mean*	*s.d.*	*mean*	*s.d.*	*mean*	*s.d.*	*mean*	*s.d.*	*mean*	*s.d.*	*mean*	*s.d.*
SST	9.4	0.0	1.8	0.4	4.9	1.2	7.0	1.4	3.1	0.0			10.9	0.6	12.4	0.5		
Salinity	33.8	0.0	33.0	0.0	33.0	0.2	32.8	0.6	33.2	0.0			32.9	0.1	33.0	0.2		
Density	1026.1	0.0	1026.4	0.0	1026.1	0.2	1025.7	0.4	1026.4	0.0			1025.2	0.2	1024.9	0.2		
%O_{2bio}	0.5	0.3	-1.9	0.5	-0.5	0.7	0.2	0.3	-1.9	0.1			0.2	0.8	0.2	1.2		
***NOP*$_U$**	9	5	-40	11	-10	15	8	14	-35	2			1	8	2	8		

3.4.3 Spring and summer cruises

In spring and summer, as in winter, SST, salinity, density and k_{O2} were more highly spatially variable in the western subarctic and transition zone (especially in KURO) than in the corresponding eastern regions and the subtropics, suggesting the influence of frontal and eddy features in the west (Figure 3.4). In spring, the mixed layer was deepest in the subtropics at ~80 m and shoaled substantially as the cruise crossed the TZCF (April 2009). In summer (July 2011), the mixed layer was quite shallow throughout the western basin and in the TZE (<20 m).

Biological O_2 peaked strongly in spring (May) and summer (July) in the western provinces, with regional mean $\%O_{2\text{bio}}$ of 2–4% (CJ, KURO, and TZW) in May and 8–9% (CJ and OYA) in July (Figure 3.4 and Table 3.3.2). This led to high regional mean NOP_U in these provinces of 33–60 mmol O_2 m^{-2} d^{-1} in May and 108–133 mmol O_2 m^{-2} d^{-1} in July (Table 3.3.2). In the rest of the subarctic, regional mean NOP_U was ~5x greater in SAW than SAE in May (22 and 4 mmol O_2 m^{-2} d^{-1}, respectively), but rates in the two provinces were similar in July at 55 and 44 mmol O_2 m^{-2} d^{-1}, respectively (Table 3.3.2). In the eastern transition zone, biological O_2 was supersaturated in TZE in April and July at ~2%, and NOP_U peaked at ~50 mmol O_2 m^{-2} d^{-1} as the cruise crossed the TZCF (180–200° lon). In contrast, biological O_2 was generally undersaturated in the eastern transition zone in May.

In our one spring cruise with pCO_2 data (April 2009), we found that, similar to our winter results, pCO_2 was more undersaturated in the western basin and subtropics than in the east (TZE) (Figure 3.5 and Table 3.3.2). Accordingly, mean CO_2 influx was greater in the western regions (at ~10 mmol C m^{-2} d^{-1}) than in the east (3–7 mmol C m^{-2} d^{-1}). CO_2 influx showed peaks across the TZCF corresponding to the peaks in NOP_U in this region (180–200° lon). On this cruise, we found low surface nitrate concentrations (<2 μM) throughout the subtropics, western and eastern

transition zones. Surface silicate concentrations were 2–4 μM in the subtropics and western transition zone and 2–6 μM in the eastern transition zone.

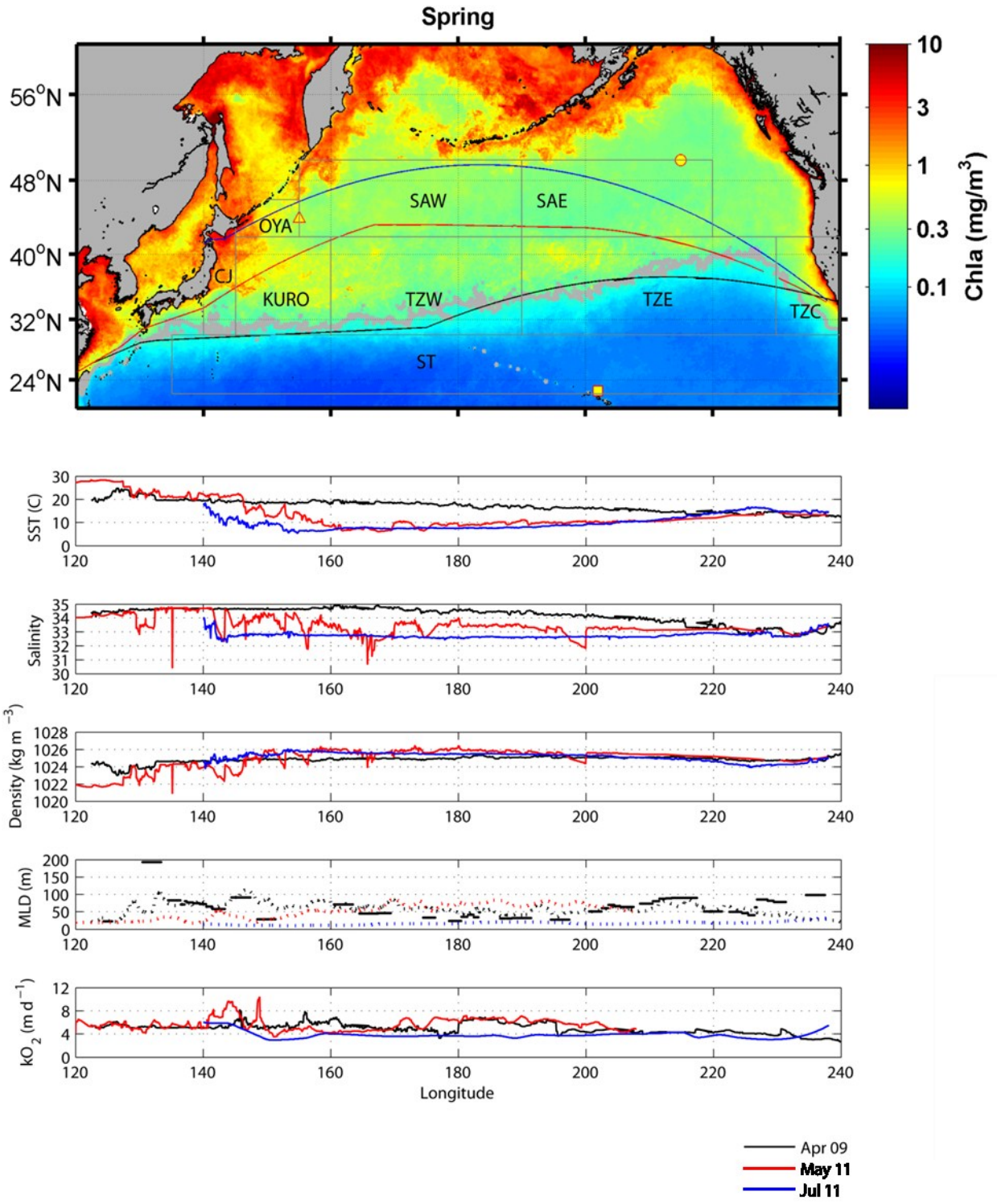

Figure 3.4: Top, spring and summer cruise tracks overlain on climatological spring chl-a (MODIS 9-km). Below, spring and summer SST, salinity, density, MLD, and k_{O2}. For MLD, solid line is from Jamstec (Argo-based) and dashed line is from FNMOC.

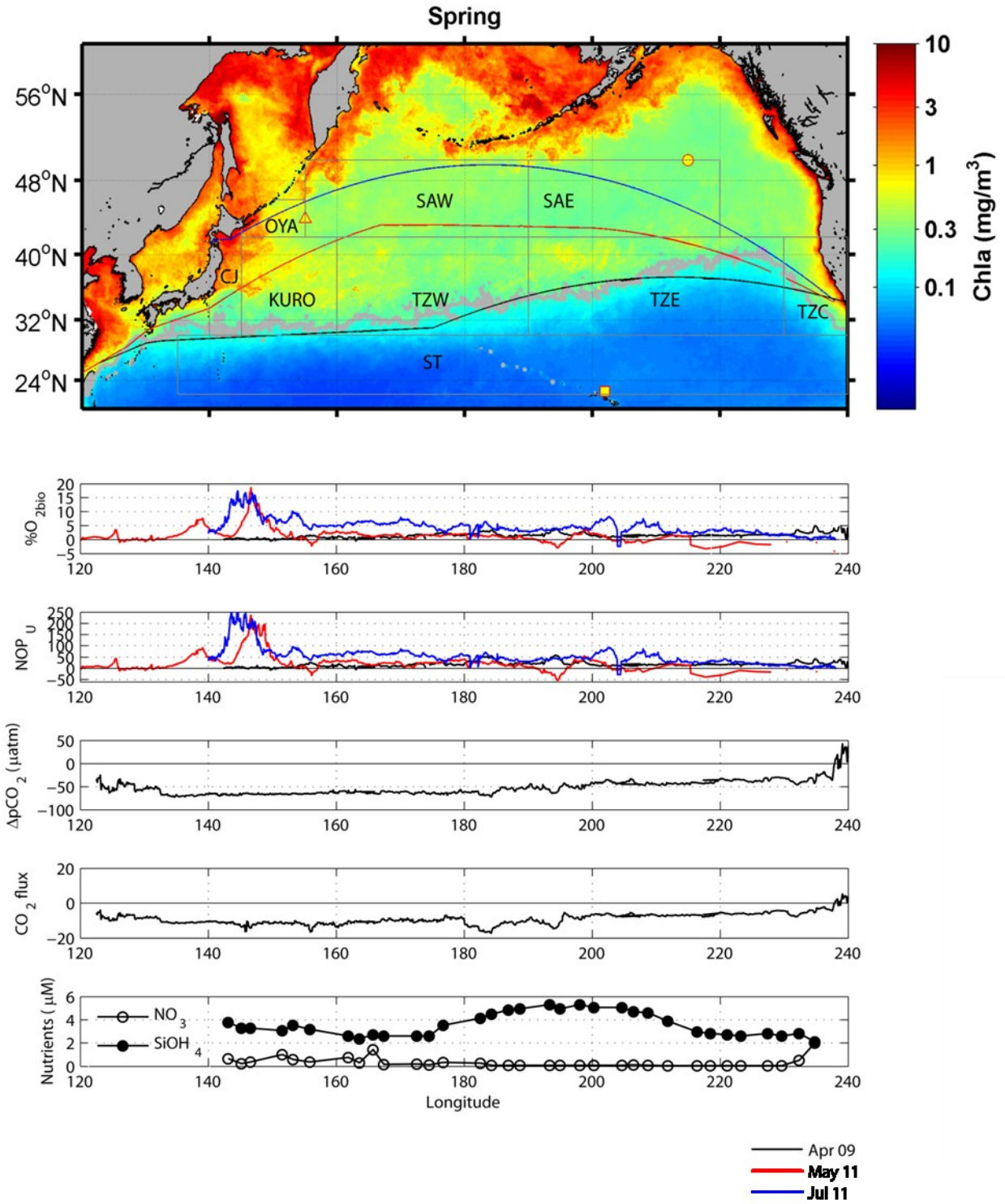

Figure 3.5: Top, spring and summer cruise tracks overlain on climatological spring chl-a (MODIS 9-km). Below, spring and summer $\%O_{2bio}$, uncorrected *NOP* (NOP_U, mmol O_2 m^{-2} d^{-1}), ΔpCO_2, CO_2 flux (mmol C m^{-2} d^{-1}), and nitrate (μM).

Table 3.3.2: Spring and summer cruise results

Regional mean and s.d. of SST (°C), density (kg m^{-3}), MLD (m) from FNMOC (OSU) or gridded Argo data (Argo), k_{O2} (m d^{-1}), NOP_U (mmol O_2 m^{-2} d^{-1}), ΔpCO_2 (μatm), and CO_2 flux (mmol C m^{-2} d^{-1}; negative values indicate flux into the ocean).

	CJ		OYA		SAW		SAE		KURO		TZW		TZE		TZC		ST	
Apr. 2009	*mean*	*s.d.*	*mean*	*s.d.*	*mean*	*s.d.*	*mean*	*s.d.*	*mean*	*s.d.*	*mean*	*s.d.*	*mean*	*s.d.*	*mean*	*s.d.*	*mean*	*s.d.*
SST									18.7	0.4	17.9	0.9	15.1	1.1	12.9	0.6	19.2	0.5
Salinity									34.7	0.0	34.6	0.2	33.8	0.5	33.0	0.3	34.7	0.0
Density									1024.8	0.1	1025.0	0.1	1025.0	0.2	1024.9	0.2	1024.7	0.1
MLD OSU									71	10	57	10	58	11	31	7	80	15
MLD Argo									29	0	43	14	63	21	92	9	72	18
k_{O2}									5.7	0.6	5.4	0.9	4.6	0.6	3.4	0.5	5.4	0.6
$\%O_{2bio}$									0.6	0.5	1.4	0.7	1.6	0.5	2.8	0.9	0.2	0.2
NOP_U									9	7	19	12	19	8	25	7	3	3
ΔpCO_2									-65	2	-62	4	-43	7	-22	23	-67	2
CO_2 flux									-12	1	-11	2	-7	2	-3	3	-12	1

	CJ		OYA		SAW		SAE		KURO		TZW		TZE		TZC		ST	
May 2011	*mean*	*s.d.*	*mean*	*s.d.*	*mean*	*s.d.*	*mean*	*s.d.*	*mean*	*s.d.*	*mean*	*s.d.*	*mean*	*s.d.*	*mean*	*s.d.*	*mean*	*s.d.*
SST	21.6	0.5			8.6	1.4	10.2	0.4	13.8	3.5	8.2	0.7	12.2	1.1	13.5	0.4		
Salinity	33.9	0.8			33.2	0.5	33.1	0.4	33.7	0.5	33.4	0.1	33.2	0.1	33.1	0.3		
Density	1023.5	0.6			1025.8	0.3	1025.4	0.3	1025.2	0.8	1026.0	0.0	1025.1	0.2	1024.9	0.3		
MLD OSU																		
MLD Argo	42	11			68	10	68	8	38	11	50	1						
k_{O2}	7.4	1.4			5.8	0.9	5.6	0.7	5.2	1.3	4.3	0.1						
$\%O_{2bio}$	2.3	1.0			1.4	0.6	0.2	1.5	4.2	4.6	2.6	0.2	-1.2	1.7	-2.0	1.9		

***NOP*$_U$**	37	16			22	9	4	24	60	68	32	2	-12	20	-11	4		

	CJ		**OYA**		**SAW**		**SAE**		**KURO**		**TZW**		**TZE**		**TZC**		**ST**	
Jul. 11	*mean*	*s.d.*	*mean*	*s.d.*	*mean*	*s.d.*	*mean*	*s.d.*	*mean*	*s.d.*	*mean*	*s.d.*	*mean*	*s.d.*	*mean*	*s.d.*	*mean*	*s.d.*
SST	12.8	2.6	8.7	1.6	7.4	0.4	10.4	1.7					15.9	0.5	14.7	0.3		
Salinity	32.9	0.5	32.8	0.1	32.7	0.1	32.7	0.1					32.8	0.1	33.0	0.3		
Density	1024.8	0.3	1025.5	0.3	1025.5	0.1	1025.1	0.2					1024.1	0.1	1024.5	0.3		
MLD OSU																		
MLD Argo	14	1	11	0	15	3	18	2					19	1	26	3		
***k*$_{O2}$**	5.8	0.1	3.7	0.8	3.7	0.2	3.9	0.2					3.2	0.1	3.9	0.7		
%O$_{2bio}$	8.3	4.8	9.5	3.2	4.9	1.2	3.9	1.7					2.2	0.6	0.8	0.5		
***NOP*$_U$**	133	78	108	57	54	14	44	19					18	5	8	4		

3.4.4 Fall cruises

In fall, we continued to see the consistent pattern of higher spatial variability in *SST*, salinity and *MLD* in the western basin than in the eastern part, with sharp spatial gradients suggesting frontal features and/or eddies (Figure 3.6). *MLD* and k_{O2} increased from early (September) to late fall (November). In the west in late fall, *MLD* and k_{O2} were greatest in the transition zone (KURO) and lower in the subarctic (OYA) (Figure 3.6 and Table 3.3.3). *MLD* in the TZE (~40–80 m) was generally shallower than in the TZW.

Biological O_2 was generally supersaturated across the basin in fall (Figure 3.7). It was greatest and most variable in the western subarctic (OYA and SAW), with mean values of 2–5%. In the western transition zone (KURO and TZW) it was closer to equilibrium and showed regions of undersaturation. In the eastern subarctic and transition zone, biological O_2 was consistently supersaturated at 1–3% (Figure 3.7 and Table 3.3.3). NOP_U showed a similar pattern to $\%O_{2bio}$, with highest variability and mean values in the OYA and SAW regions (regional cruise means of 23–26 and 10–26 mmol O_2 m^{-2} d^{-1}, respectively), and lowest values (including negative values) in the TZW. In the SAE and TZE, NOP_U was similar among all cruises.

On all fall cruises, pCO_2 was more undersaturated in the western basin than in the east, approaching saturation east of 140° W (Figure 3.7 and Table 3.3.3). ΔpCO_2 showed similar values in the NW subarctic and transition zone (–40–100 μtam) on November cruises in different years. CO_2 flux showed a similar pattern to ΔpCO_2, with mean uptake of 12 mmol C m^{-2} d^{-1} in the west and 6 mmol C m^{-2} d^{-1} in the east.

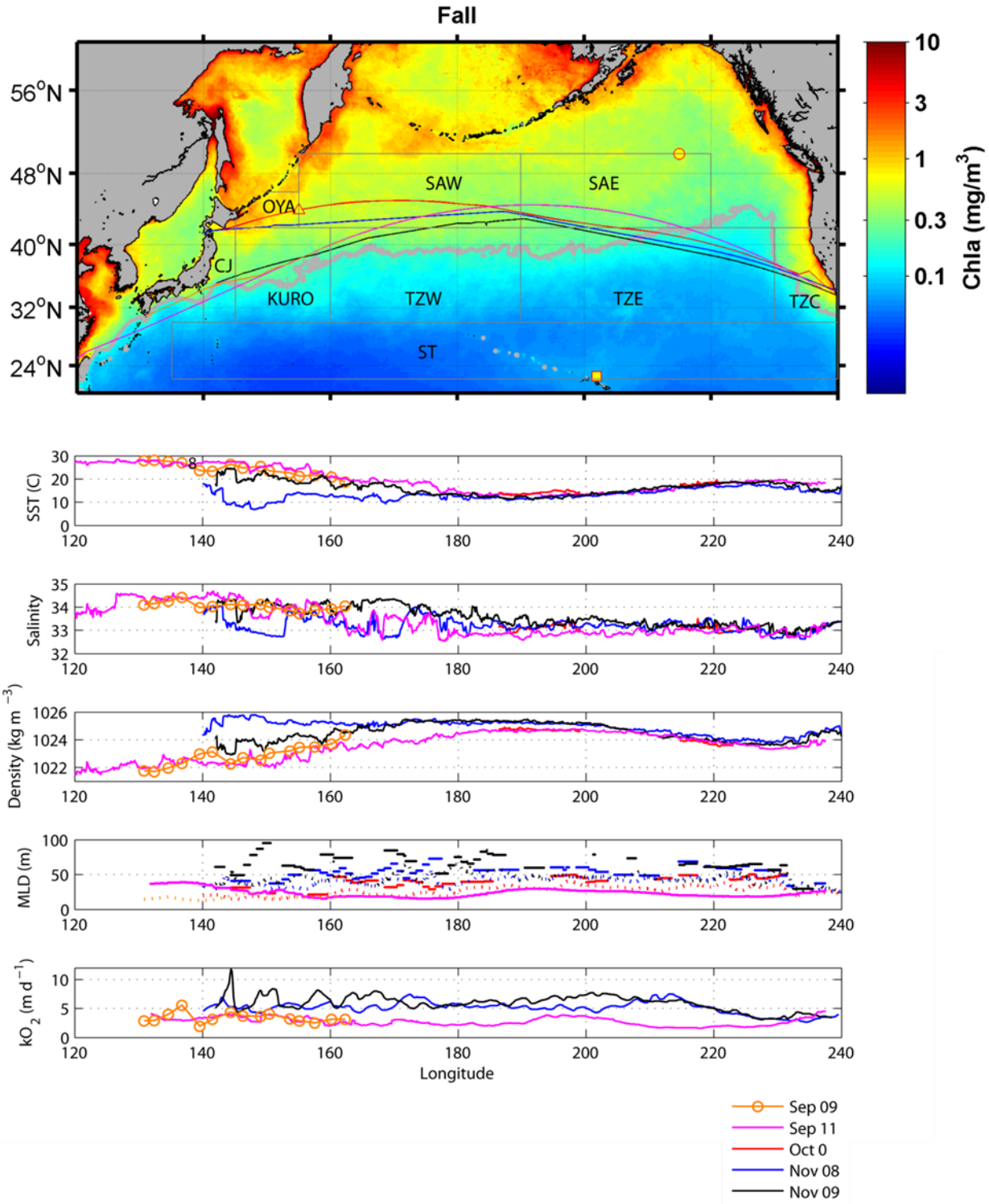

Figure 3.6: Top, fall cruise tracks overlain on climatological fall chl-a (MODIS 9-km). Below, SST, salinity, density, MLD, and k_{O2}. For MLD, solid line is from Jamstec (Argo-based) and dashed line is from FNMOC.

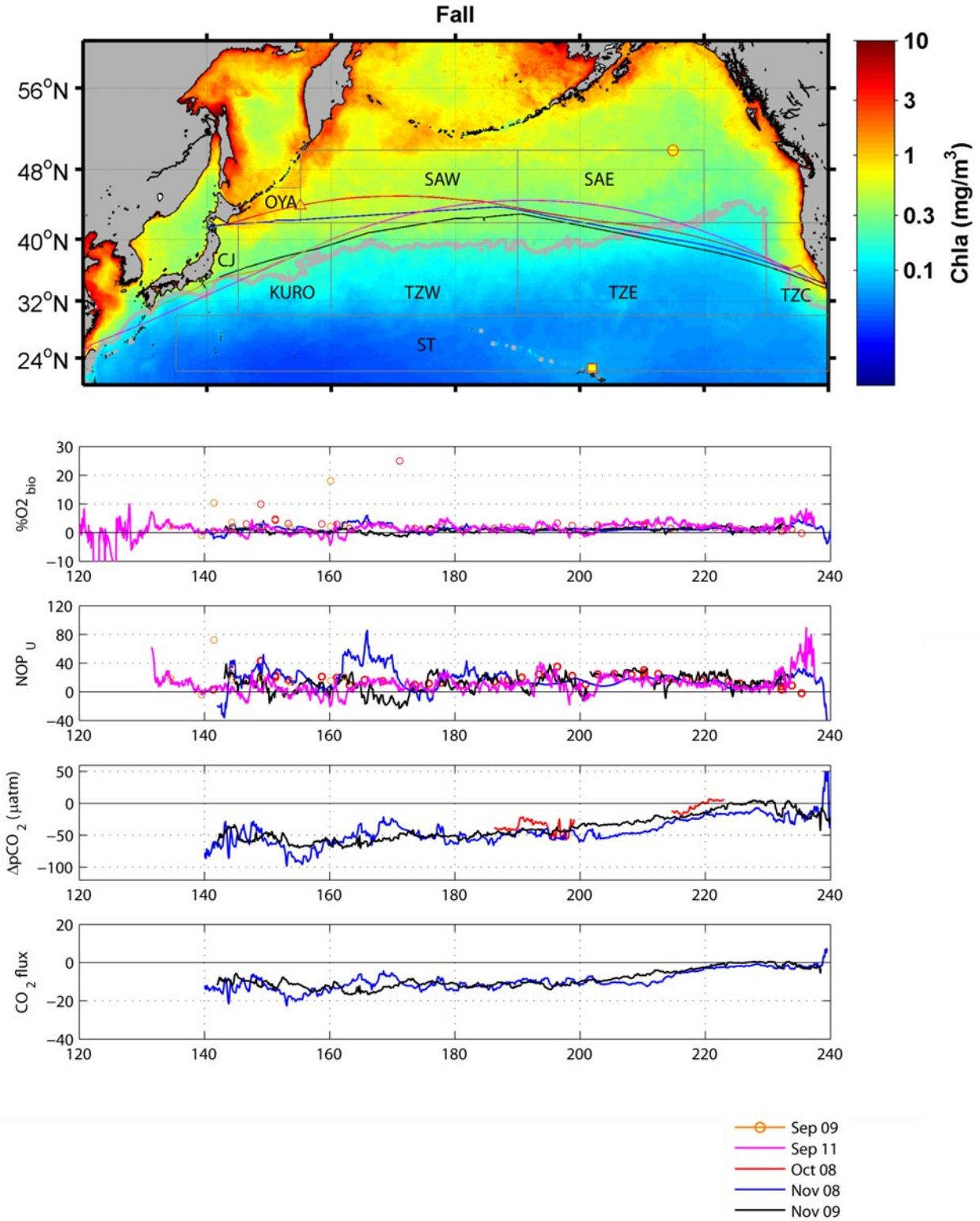

Figure 3.7: Top, Fall cruise tracks overlain on climatological fall chl-a (MODIS 9-km). Below, Fall $\%O_{2bio}$, uncorrected *NOP* (NOP_U, mmol O_2 m^{-2} d^{-1}), ΔpCO_2, and CO_2 flux (mmol C m^{-2} d^{-1}).

Table 3.3.3: Fall cruise results

Regional mean and s.d. of SST (°C), density (kg m^{-3}), MLD (m) from FNMOC (OSU) or gridded Argo data (Argo), k_{O2} (m d^{-1}), NOP_U (mmol O_2 m^{-2} d^{-1}), ΔpCO_2 (µatm), and CO_2 flux (mmol C m^{-2} d^{-1}; negative values indicate flux into the ocean).

Region	**CJ**		**OYA**		**SAW**		**SAE**		**KURO**		**TZW**		**TZE**		**TZC**	
Sept 2009	*mean*	*s.d.*	*mean*	*s.d.*	*mean*	*s.d.*	*mean*	*s.d.*	*mean*	*s.d.*	*mean*	*s.d.*	*mean*	*s.d.*	*mean*	*s.d.*
SST	25.4	1.8							22.9	1.6	19.9	1.2				
Salinity	34.1	0.0							33.9	0.1	34.0	0.1				
Density	1022.5	0.5							1023.1	0.4	1024.0	0.4				
MLD OSU	17	4							18	2	18	0				
MLD Argo																
k_{O2}	4.0	0.7							3.2	0.6	3.2	0.0				
$\%O_{2bio}$	5.3	4.5							2.2	0.4	7.7	9.0				
NOP_U	41	29							17	4	55	64				

	CJ		**OYA**		**SAW**		**SAE**		**KURO**		**TZW**		**TZE**		**TZC**	
Sept. 2011	*mean*	*s.d.*	*mean*	*s.d.*	*mean*	*s.d.*	*mean*	*s.d.*	*mean*	*s.d.*	*mean*	*s.d.*	*mean*	*s.d.*	*mean*	*s.d.*
SST	27.3	0.2			15.8	2.4	14.1	1.1	24.7	1.9	19.8	0.8	18.3	0.9	18.5	0.6
Salinity	34.5	0.1			33.0	0.3	32.9	0.1	33.9	0.3	33.3	0.4	33.0	0.1	32.9	0.2
Density	1022.3	0.1			1024.3	0.4	1024.5	0.2	1022.6	0.5	1023.5	0.2	1023.7	0.2	1023.6	0.2
MLD OSU																
MLD Argo	33	3			20	4	26	3	23	4	19	0	19	1	23	2
k_{O2}	3.7	0.2			2.4	0.3	2.8	0.8	3.3	0.5	2.4	0.2	1.9	0.2	3.3	0.7
$\%O_{2bio}$	0.5	0.4			1.6	1.2	2.2	1.6	0.1	1.3	0.6	2.1	1.9	0.9	3.9	2.0
NOP_U	4	3			9	6	14	11	1	9	3	11	8	4	33	20

	CJ		OYA		SAW		SAE		KURO		TZW		TZE		TZC	
Oct. 2008	*mean*	*s.d.*	*mean*	*s.d.*	*mean*	*s.d.*	*mean*	*s.d.*	*mean*	*s.d.*	*mean*	*s.d.*	*mean*	*s.d.*	*mean*	*s.d.*
SST	15.7	2.9	14.0	1.3	13.8	1.0	14.4	0.5					17.0	1.5	15.8	1.1
Salinity	33.4	0.8	32.8	0.4	32.8	0.3	33.1	0.1					33.0	0.2	33.0	0.2
Density	1024.6	0.0	1024.4	0.2	1024.5	0.2	1024.6	0.1					1024.0	0.3	1024.2	0.4
MLD OSU	19	2	16	1	25	5	33	3					32	3	25	4
MLD Argo	32	0	29	4	37	7	45	4					46	2	50	1
k_{O2}	2.2	0.6	1.9	0.1	2.8	0.5	3.8	0.2					4.2	0.5	2.9	0.4
$\%O_{2bio}$	0.5	0.0	4.9	2.3	3.9	6.7	2.3	0.7					1.9	0.6	1.1	0.8
NOP_U	3	0	23	9	26	43	23	8					20	6	8	6
ΔpCO_2					-40	1	-36	11					-4	8		

	CJ		OYA		SAW		SAE		KURO		TZW		TZE		TZC	
Nov. 2008	*mean*	*s.d.*	*mean*	*s.d.*	*mean*	*s.d.*	*mean*	*s.d.*	*mean*	*s.d.*	*mean*	*s.d.*	*mean*	*s.d.*	*mean*	*s.d.*
SST	13.7	3.3	10.2	2.3	12.3	1.0	12.2	0.6	8.6	0.9			15.7	1.5	15.1	0.9
Salinity	33.7	0.3	33.1	0.4	33.3	0.3	33.2	0.1	33.1	0.1			33.2	0.2	33.0	0.2
Density	1025.2	0.5	1025.4	0.2	1025.2	0.1	1025.2	0.0	1025.7	0.1			1024.4	0.4	1024.4	0.3
MLD OSU	37	5	33	2	40	5	47	2	38	3			44	2	32	5
MLD Argo	41	0	43	6	56	7	60	1	41	0			57	6	41	8
k_{O2}	5.5	0.6	5.1	0.6	5.6	0.7	5.1	0.2	5.1	0.4			5.2	1.3	3.2	0.3
$\%O_{2bio}$	-0.1	1.6	1.9	0.7	1.5	1.3	0.9	0.2	1.3	0.4			1.0	0.3	1.9	1.7
NOP_U	0	30	26	9	22	18	13	3	20	5			13	5	16	13
ΔpCO_2	-65	14	-64	16	-54	14	-49	6	-49	11			-31	15	-15	18
CO_2 **flux**	-14	2	-14	4	-12	3	-10	1	-11	3			-6	4	-2	2

	CJ		OYA		SAW		SAE		KURO		TZW		TZE		TZC	
Nov. 2009	*mean*	*s.d.*	*mean*	*s.d.*	*mean*	*s.d.*	*mean*	*s.d.*	*mean*	*s.d.*	*mean*	*s.d.*	*mean*	*s.d.*	*mean*	*s.d.*
SST	22.9	2.1			12.8	0.7	12.1	0.5	20.2	1.5	16.4	1.6	16.5	1.9	16.5	1.3
Salinity	34.2	0.3			33.6	0.2	33.3	0.1	34.0	0.2	34.1	0.2	33.3	0.2	33.1	0.2
Density	1023.3	0.4			1025.3	0.0	1025.3	0.1	1024.0	0.3	1024.9	0.3	1024.3	0.5	1024.1	0.4
MLD OSU	42	6			54	5	46	3	41	4	46	8	45	5	35	9
MLD Argo	58	5			70	11	60	0	69	14	77	5	64	5	41	15
k_{O2}	7.6	2.0			5.9	0.4	6.6	0.4	6.3	1.3	6.4	0.9	5.7	1.4	3.8	0.3
$\%O_{2bio}$	1.3	0.4			0.9	0.5	0.8	0.5	0.5	0.6	0.0	0.8	1.3	0.7	2.0	0.6
NOP_U	24	6			14	8	15	10	7	9	0	13	17	9	18	6
ΔpCO_2	-45	8			-50	3	-43	3	-58	7	-58	7	-20	14	-12	10
CO_2 flux	-10	1			-12	1	-11	1	-11	2	-13	2	-5	4	2	1

3.4.5 Seasonal cycle of NOP and influence of physical supply on O_2 and O_2/Ar budgets

To construct a seasonal cycle of *NOP* in each of the eight North Pacific provinces, we calculated regional mean NOP_U for the months of our cruises by averaging all of our estimates within each province. We then combined the results into a composite year by interpolating these monthly means over the annual cycle (Figure 3.8). To correct NOP_U for physical inputs ($F_{physO2/Ar}$), we calculated mean monthly $F_{physO2/Ar}$ in each province by averaging monthly results from our climatological O_2/Ar box model (described in section 3.3.4) for all grid cells within each region. We then interpolated monthly mean $F_{physO2/Ar}$ in each province over the annual cycle (Figure 3.8).

For both NOP_U and $F_{physO2/Ar}$, monthly data were interpolated to a daily time step using a piecewise cubic hermite interpolation polynomial (pchip command) in Matlab. We then subtracted the resulting $F_{physO2/Ar}$ curve from NOP_U to obtain corrected *NOP* (NOP_C; Figure 3.8). We examine the individual terms contributing to this correction and the uncertainty in NOP_C below.

The western boundary provinces influenced by the Kuroshio and Oyashio currents, CJ, OYA and KURO, had the largest seasonal amplitude of both NOP_U and $F_{physO2/Ar}$, with large negative values in winter and high summertime rates of NOP_U (Figure 3.8 and Table 3.4). In the other subarctic provinces, the seasonal amplitude of NOP_U and $F_{physO2/Ar}$ became smaller toward the east (OYA>SAW>SAE). SAW had negative NOP_U in winter that was generally explained by $F_{physO2/Ar}$ (resulting in near-zero wintertime NOP_C), and high NOP_U in summer with a secondary peak in fall. SAE had positive NOP_U throughout the year at relatively low rates, with peaks in summer and fall. In TZW, we observed relatively high rates of *NOP* in spring and negative *NOP* in winter (even after correction for $F_{physO2/Ar}$). In TZE and TZC, we found positive *NOP* at

relatively low rates during most of the year, and only one month with net heterotrophic conditions (March).

Although we used the climatological O_2/Ar model to correct NOP_U, we determined the relative importance of individual physical terms in both the O_2 and O_2/Ar models (described in section 3.3.4) by examining the seasonal means in each province (Figures 3.9–3.12 and Table 3.4). This allows us to clarify which physical terms are the most important sources of bias in NCP estimates based on the O_2 and O_2/Ar budgets.

The influence of physical supply on both the O_2 and O_2/Ar budgets was largest in winter (Figure 3.9). Vertical diffusive mixing dominated the O_2 and O_2/Ar physical budgets in the provinces influenced by the Kuroshio current and extension (CJ, KURO, and TZW) as a major loss term; entrainment made a smaller but significant negative contribution to the budgets in these provinces and in OYA. This yielded very negative mean net physical supply of O_2 (F_{physO2} of –72 to –22 mmol O_2 m^{-2} d^{-1}) and O_2/Ar ($F_{\mathrm{physO2/Ar}}$ of –92 to –45 mmol O_2 m^{-2} d^{-1}; Table 3.4) in these regions, explaining the very negative wintertime NOP_U we estimated there (Figures 3.3 and 3.9 and Table 3.4). These provinces have very deep MLDs and high wind speeds in winter (Figure 3.2), leading to entrainment and vertical diffusive mixing of deeper water undersaturated in O_2/Ar and rich in nutrients (Figure 3.3). In the rest of the basin, Ekman transport dominated the O_2 physical budget in winter, yielding negative F_{physO2} in the subarctic (–51 to –23 to mmol O_2 m^{-2} d^{-1}) and positive F_{physO2} in the eastern transition zone (9–17 mmol O_2 m^{-2} d^{-1}; Figure 3.9 and Table 3.4). In contrast, the O_2/Ar physical supply in the rest of the basin was smaller and dominated by entrainment, with more negative values in the western basin than in the east.

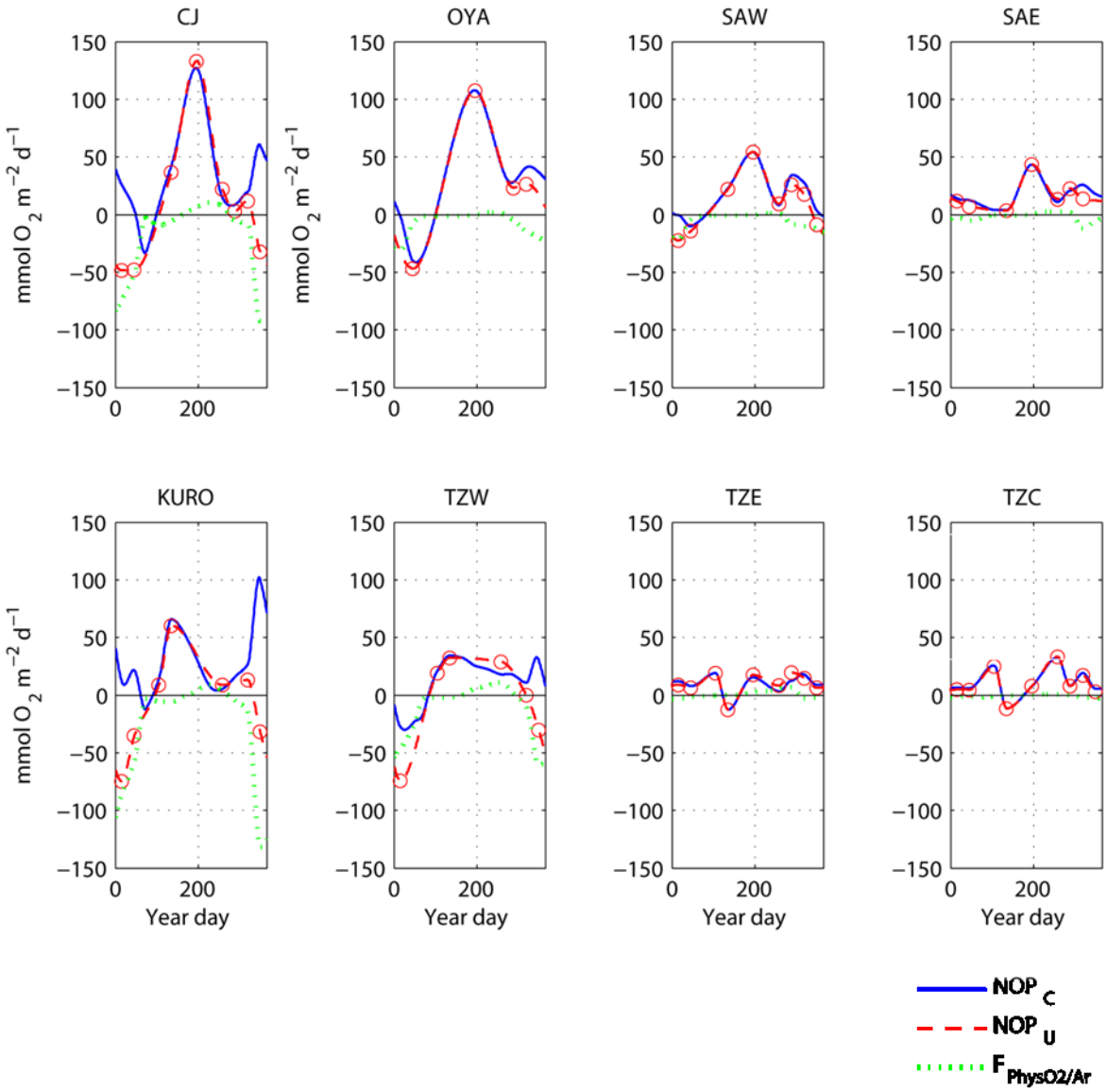

Figure 3.8: Composite annual cycle of NOP_U (circles, mean cruise results), $F_{physO2/Ar}$ (from climatological O_2/Ar model), and corrected NOP (NOP_C) in provinces. Units, mmol O_2 m^{-2} d^{-1}.

Table 3.4: Seasonal results of climatological O_2 and O_2/Ar box models and NOP_U, NOP_C, and NCP

Regional mean fluxes ± uncertainty in mmol O_2 m^{-2} d^{-1} (except for NCP rows, in mmol C m^{-2} d^{-1}). Correction (%) indicates the percentage correction made to NOP_U for $F_{physO2/Ar}$.

		Winter (DJF)		***Spring (MAM)***		***Summer (JJA)***		***Fall (SON)***	
Region	Term	O_2 budget	O_2/Ar budget	O_2 budget	O_2/Ar budget	O_2 budget	O_2/Ar budget	O_2 budget	O_2/Ar budget
CJ	Ekman	-17 ± 4	0	-8 ± 2	0	0	0	-2 ± 1	0
	Geostrophic	0 ± 0	0	0	0	-1 ± 0	0	-1 ± 0	0
	Entrainment	-4 ± 1	-6 ± 2	0	0	1 ± 0	0	1 ± 0	-3 ± 1
	Vertical diffusion	-38 ± 19	-55 ± 27	-4 ± 2	-6 ± 3	15 ± 7	5 ± 2	4 ± 2	1 ± 1
	F_{phys}	-68 ± 25	-73 ± 29	-12 ± 4	-6 ± 3	15 ± 8	6 ± 3	1 ± 3	-2 ± 1
	NOP_U		-42 ± 11		2 ± 1		102 ± 27		12 ± 3
	NOP_C		28 ± 40 [0]		9 ± 4		96 ± 29		17 ± 5
	NCP (mmol C m^{-2} d^{-1})		0		6 ± 2		66 ± 20		12 ± 3
	Correction (%)		169		336		–6		39
OYA	Ekman	-1 ± 0	0	-1 ± 0	0	0	0	4 ± 1	0
	Geostrophic	1 ± 0	0	1 ± 0	0	1 ± 0	0	1 ± 0	0
	Entrainment	-14 ± 3	-16 ± 4	0	0	1 ± 0	0	0	-5 ± 1
	Vertical diffusion	-2 ± 1	-2 ± 1	-1 ± 0	-1 ± 1	3 ± 2	0	1 ± 0	-1 ± 0
	F_{phys}	-15 ± 5	-19 ± 5	0 ± 1	-1 ± 1	5 ± 2	0	5 ± 2	-6 ± 2
	NOP_U		-20 ± 3		10 ± 2		93 ± 15		32 ± 5
	NOP_C		0 ± 8 [0]		11 ± 2		93 ± 15		38 ± 7
	NCP (mmol C m^{-2} d^{-1})		0		8 ± 1		64 ± 10		26 ± 5
	Correction (%)		98		12		0		20

SAW	Ekman	-39 ± 10	1 ± 0	-5 ± 1	0	-1 ± 0	0	6 ± 1	0
	Geostrophic	0	0	0	0	0	0	0	0
	Entrainment	-10 ± 2	-11 ± 2	0	0	1 ± 0	0	4 ± 1	-5 ± 1
	Vertical diffusion	-2 ± 1	-2 ± 1	-1 ± 0	-1 ± 0	1 ± 1	0	1 ± 0	-1 ± 0
	F_{phys}	-51 ± 12	-13 ± 3	-6 ± 2	-1 ± 1	1 ± 1	0	10 ± 3	-6 ± 1
	NOP_U		-15 ± 7		10 ± 5		42 ± 21		18 ± 9
	NOP_C		-2 ± 10 [0]		10 ± 5		42 ± 21		23 ± 10
	NCP (mmol C m^{-2} d^{-1})		0		7 ± 4		29 ± 14		16 ± 7
	Correction (%)		89		0		0		32
SAE	Ekman	-21 ± 5	0	-2 ± 1	0	1 ± 0	0	3 ± 1	0
	Geostrophic	0	0	0	0	0	0	0	0
	Entrainment	-2 ± 0	-3 ± 0	0	0	1 ± 0	0	7 ± 1	-2 ± 0
	Vertical diffusion	-1 ± 0	-1 ± 1	-1 ± 0	-1 ± 1	1 ± 1	0	2 ± 1	0
	F_{phys}	-23 ± 6	-4 ± 1	-3 ± 1	-1 ± 1	3 ± 1	1 ± 0	11 ± 2	-3 ± 0
	NOP_U		11 ± 3		5 ± 2		31 ± 10		17 ± 6
	NOP_C		15 ± 4		6 ± 2		31 ± 11		19 ± 6
	NCP (mmol C m^{-2} d^{-1})		10 ± 3		4 ± 1		21 ± 7		13 ± 4
	Correction (%)		43		25		3		15
KURO	Ekman	-5 ± 1	0	-2 ± 0	0	0	0	3 ± 1	0
	Geostrophic	0	0	0	0	0	0	0	0
	Entrainment	-9 ± 2	-12 ± 2	0	0	1 ± 0	0	-1 ± 0	-5 ± 1
	Vertical diffusion	-59 ± 29	-79 ± 40	-2 ± 1	-5 ± 2	13 ± 6	3 ± 2	3 ± 2	0
	F_{phys}	-72 ± 32	-92 ± 42	-4 ± 2	-5 ± 2	13 ± 7	4 ± 2	5 ± 3	-5 ± 1

	NOP_U		-46 ± 13		18 ± 5		34 ± 10		10 ± 3
	NOP_C		42 ± 55 [0]		24 ± 7		30 ± 11		19 ± 4
	NCP (mmol C m^{-2} d^{-1})		0		17 ± 5		21 ± 8		13 ± 3
	Correction (%)		191		32		–11		86
TZW	Ekman	9 ± 2	0	11 ± 3	0	2 ± 1	0	9 ± 2	0
	Geostrophic	0	0	0	0	0	0	0	0
	Entrainment	-5 ± 1	-8 ± 1	0 ± 0	0	1 ± 0	1 ± 0	4 ± 1	-1 ± 0
	Vertical diffusion	-26 ± 13	-37 ± 19	-1 ± 0	-2 ± 1	9 ± 5	4 ± 2	4 ± 2	2 ± 1
	F_{phys}	-22 ± 16	-45 ± 20	10 ± 3	-2 ± 1	13 ± 5	5 ± 2	16 ± 5	1 ± 1
	NOP_U		-52 ± 13		12 ± 3		32 ± 8		16 ± 4
	NOP_C		-8 ± 33 [0]		15 ± 4		27 ± 10		15 ± 5
	NCP (mmol C m^{-2} d^{-1})		0		10 ± 3		18 ± 7		10 ± 3
	Correction (%)		85		22		–16		–4
TZE	Ekman	17 ± 4	0	15 ± 4	0	5 ± 1	0	11 ± 3	0
	Geostrophic	0	0	0	0	0	0	0 ± 0	0
	Entrainment	0	-2 ± 0	0	0	1 ± 0	1 ± 0	9 ± 2	2 ± 0
	Vertical diffusion	0	-1 ± 0	0	0	2 ± 1	1 ± 1	2 ± 1	1 ± 0
	F_{phys}	17 ± 4	-2 ± 1	15 ± 4	0	9 ± 3	2 ± 1	22 ± 5	3 ± 1
	NOP_U		8 ± 2		6 ± 2		11 ± 3		14 ± 4
	NOP_C		10 ± 3		7 ± 2		9 ± 4		11 ± 5
	NCP (mmol C m^{-2} d^{-1})		7 ± 2		5 ± 1		6 ± 3		8 ± 3
	Correction (%)		29		3		–19		–22
TZC	Ekman	11 ± 3	0	15 ± 4	0	10 ± 2	0	8 ± 2	0
	Geostrophic	0	0	0	0	0	0	0 ± 0	0

Entrainment	-1 ± 0	-1 ± 0	0	0	0	0	1 ± 0	0
Vertical diffusion	-1 ± 0	-1 ± 1	0	-1 ± 0	0	0	0	0
F_{phys}	9 ± 3	-2 ± 1	14 ± 4	-1 ± 0	10 ± 3	0	10 ± 3	0
NOP_U		5 ± 2		9 ± 4		10 ± 4		19 ± 8
NOP_C		7 ± 3		10 ± 4		9 ± 4		19 ± 8
NCP (mmol C m^{-2} d^{-1})		5 ± 2		7 ± 3		6 ± 3		13 ± 5
Correction (%)		37		9		–3		0

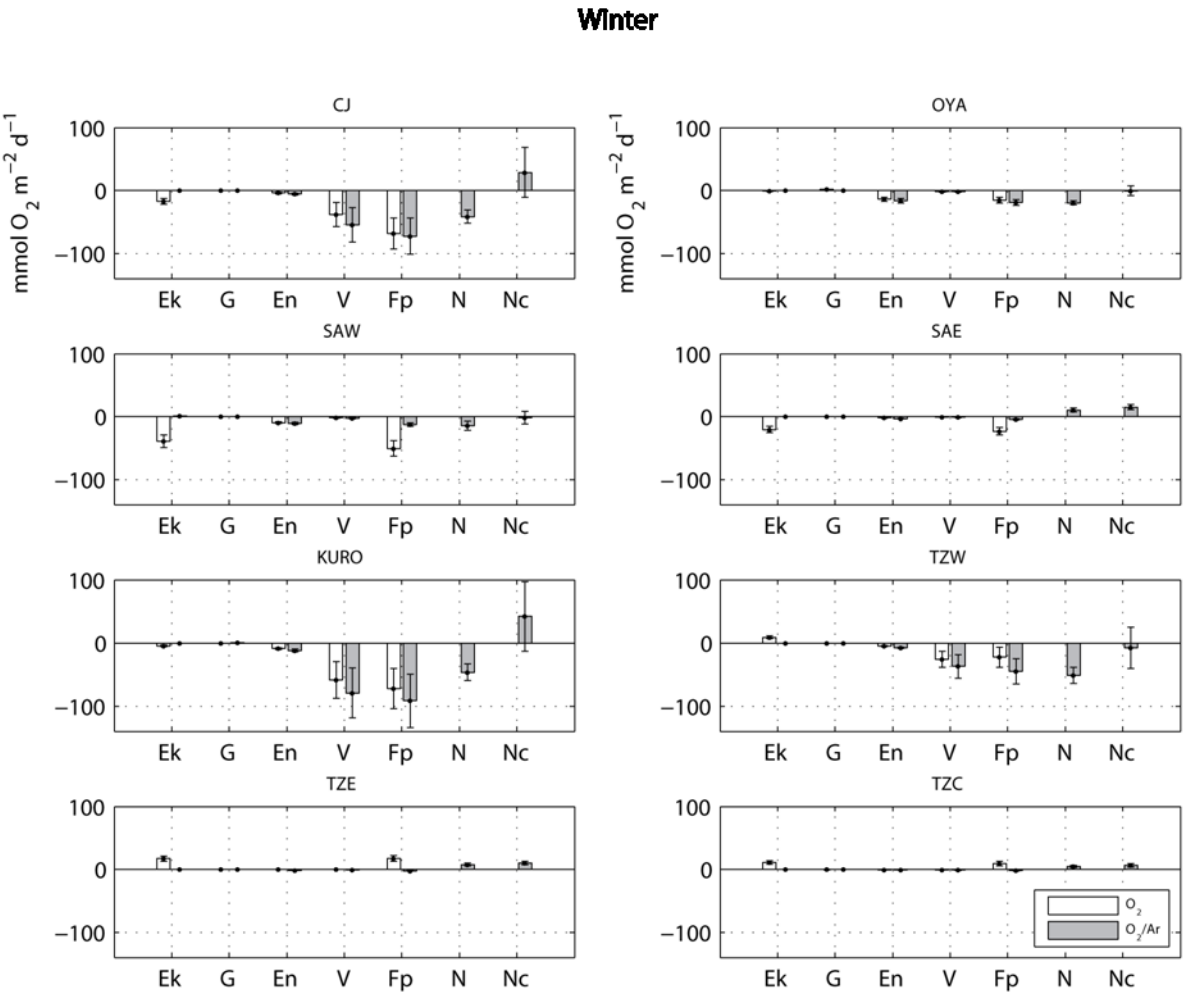

Figure 3.9: Winter results of climatological O_2 (white bars) and O_2/Ar (grey bars) physical budgets (fluxes are Ek, Ekman transport; G, geostrophic transport; En, entrainment; V, vertical diffusive mixing; and F_{phys} (Fp), the sum of these terms) and cruise-based estimates of NOP_U (N) and NOP_C (Nc). Error bars reflect 1 σ confidence intervals.

Because of the large uncertainty in the $F_{physO2/Ar}$ correction (dominated by the 50% error in vertical diffusive mixing), our wintertime NOP_C estimates are indistinguishable from zero in all the provinces in the western part of the basin (CJ, OYA, SAW, KURO and TZW; Figure 3.9 and Table 3.4); therefore we set wintertime *NCP* in these provinces to zero when calculating integrated annual *NCP* (see section 3.4.6 below). In the eastern provinces in winter, correcting

NOP_U for $F_{physO2/Ar}$ led to a mean increase of 29–37%, resulting in mean NOP_C of 7–15 mmol O_2 m^{-2} d^{-1} (Table 3.4).

In the spring and summer, physical processes had a small influence on both the O_2 and O_2/Ar budgets compared with *NOP* (Figures 3.10 and 3.11), as the mixed layer is shoaling and wind speed is generally low during these seasons. In the O_2 budget in spring and summer, Ekman transport and vertical diffusive mixing contributed to yield net F_{physO2} that was generally ~2x larger in the transition zone (~9–15 mmol O_2 m^{-2} d^{-1}) than in the subarctic (–3 to –6 mmol O_2 m^{-2} d^{-1} in spring and 1–5 mmol O_2 m^{-2} d^{-1} in summer; Figure 3.10 and Table 3.4). In comparison, for the O_2/Ar budget, $F_{physO2/Ar}$ was ≤6 mmol O_2 m^{-2} d^{-1} throughout the basin in spring and summer. In summer, the correction to NOP_U was <20% in all provinces (Table 3.4).

In fall, the O_2 physical budget was generally controlled by Ekman transport and entrainment (Figure 3.12 and Table 3.4). In most provinces, both terms were a source of O_2 to the mixed layer, leading to regional mean F_{physO2} supply of 1–22 mmol O_2 m^{-2} d^{-1}, with the highest values in TZW and TZE. In comparison, in the O_2/Ar budget, net physical supply ($F_{physO2/Ar}$) in fall was dominated by entrainment (Figure 3.12), which was a small source or sink in most provinces (≤6 mmol O_2 m^{-2} d^{-1}).

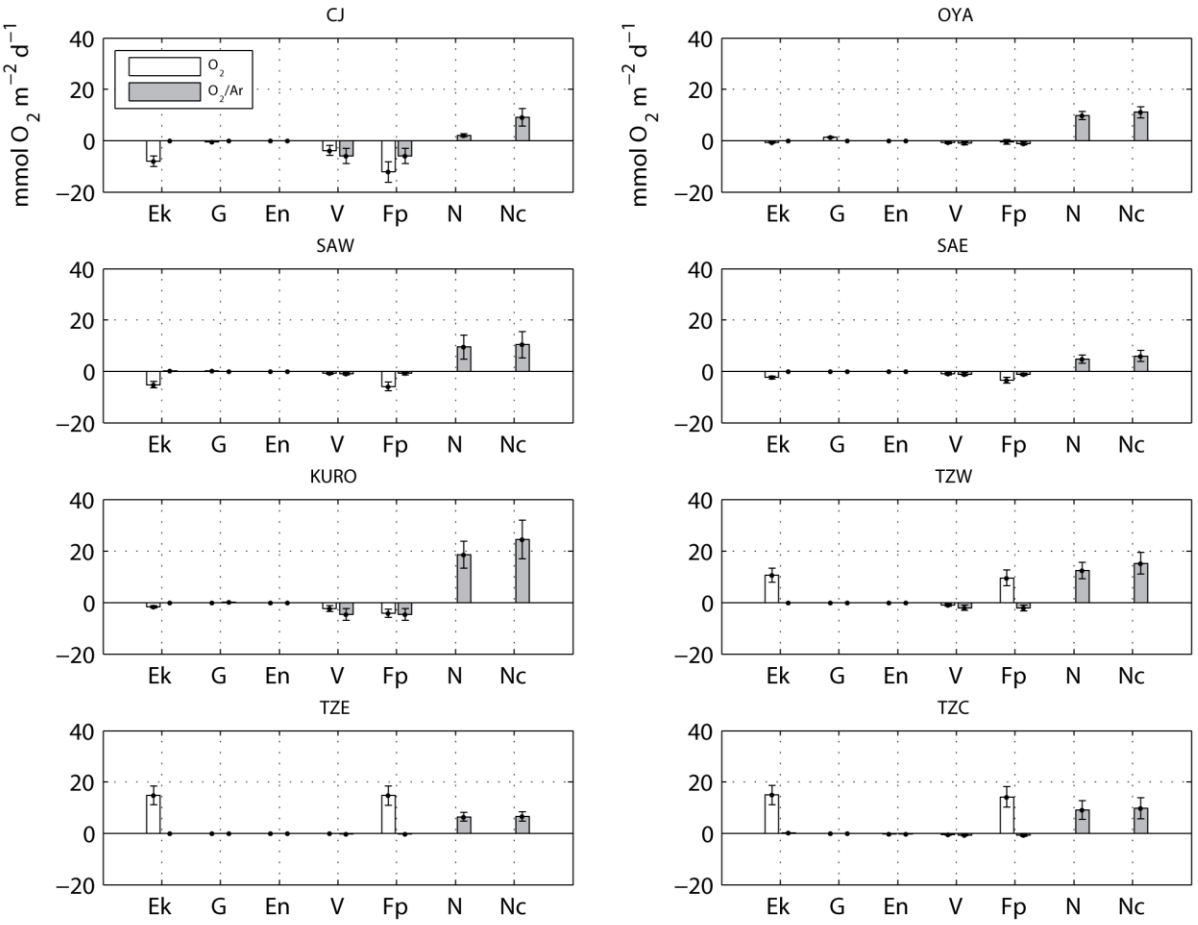

Figure 3.10: Spring results of climatological O_2 (white bars) and O_2/Ar (grey bars) physical budgets (fluxes are Ek, Ekman transport; G, geostrophic transport; En, entrainment; V, vertical diffusive mixing; and F_{phys} (Fp), the sum of these terms) and cruise-based estimates of NOP_U (N) and NOP_C (Nc). Error bars reflect 1 σ confidence intervals.

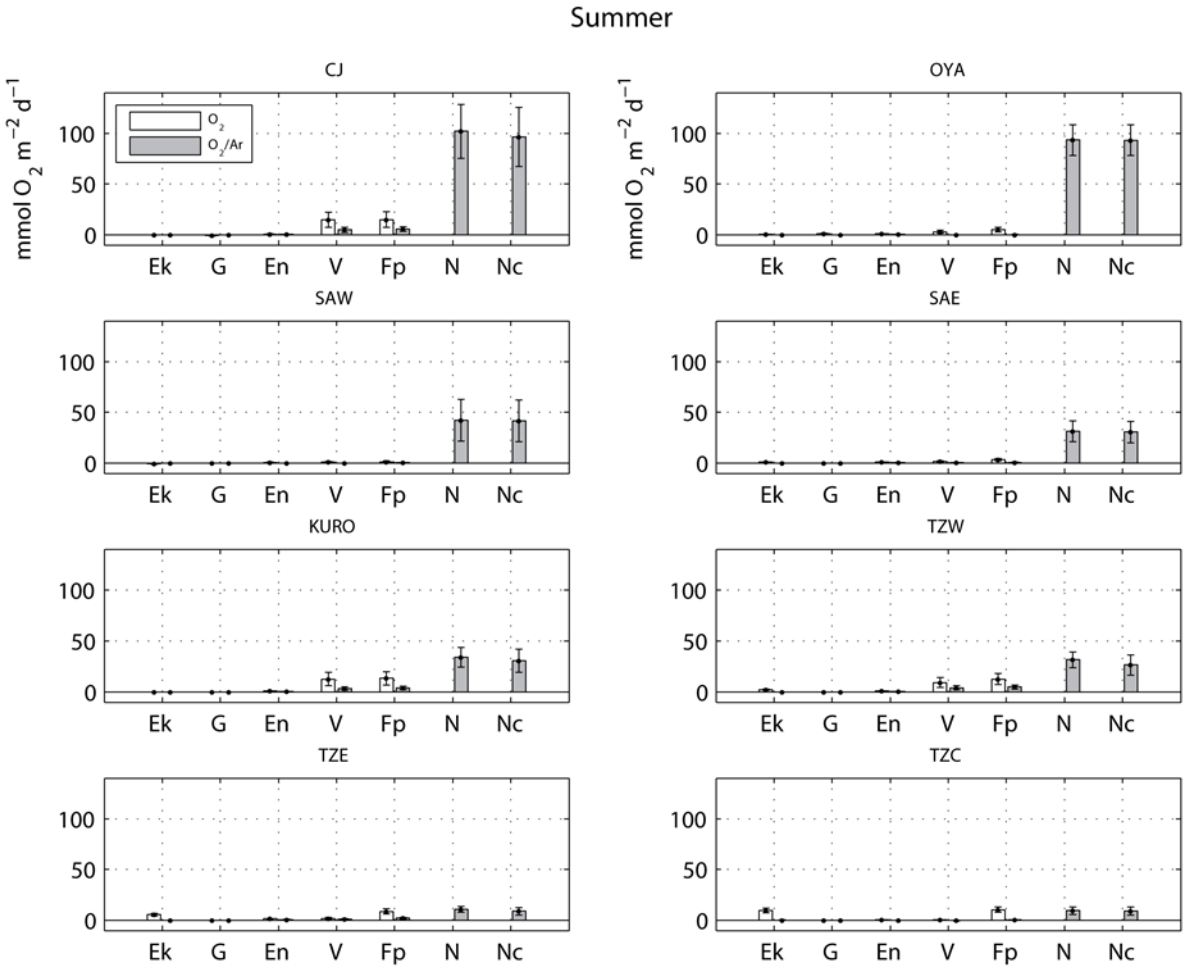

Figure 3.11: Summer results of climatological O_2 (white bars) and O_2/Ar (grey bars) physical budgets (fluxes are Ek, Ekman transport; G, geostrophic transport; En, entrainment; V, vertical diffusive mixing; and F_{phys} (Fp), the sum of these terms) and cruise-based estimates of NOP_U (N) and NOP_C (Nc). Error bars reflect 1 σ confidence intervals.

In fall, correcting NOP_U for physical supply ($F_{physO2/Ar}$) led to a substantial increase in CJ, SAW and KURO (32–85%), a smaller increase in OYA and SAE (15–20%), and a small decrease (4–22%) in TZW and TZE (Table 3.4). The resulting mean fall NOP_C was highest in OYA and lowest in TZE (38 and 11 mmol O_2 m^{-2} d^{-1}, respectively); the remaining provinces had similar mean NOP_C of 15–23 mmol O_2 m^{-2} d^{-1}.

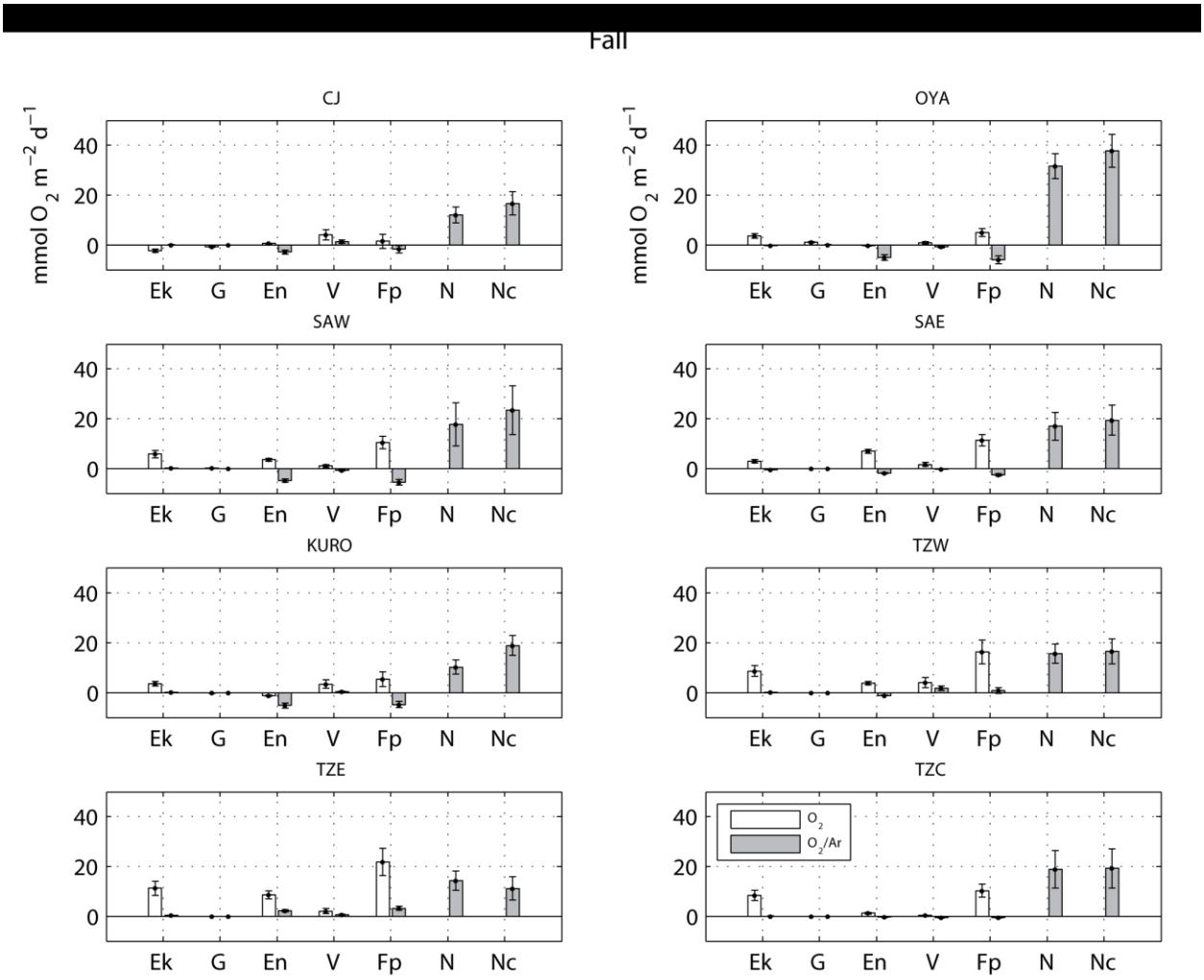

Figure 3.12: Fall results of climatological O_2 (white bars) and O_2/Ar (grey bars) physical budgets (fluxes are Ek, Ekman transport; G, geostrophic transport; En, entrainment; V, vertical diffusive mixing; and F_{phys} (Fp), the sum of these terms) and cruise-based estimates of NOP_U (N) and NOP_C (Nc). Error bars reflect 1 σ confidence intervals.

The integrated annual $F_{physO2/Ar}$ was largest in the western provinces (–1.7 to –9 mol O_2 m^{-2} yr^{-1}), which have a large seasonal amplitude in MLD and high winter wind speeds (Table 3.5). The largest values were in the provinces influenced by the Kuroshio current (CJ and KURO; –6.8 ± 3.4 and –9 ± 4.4 mol O_2 m^{-2} yr^{-1}, respectively). Integrated annual $F_{physO2/Ar}$ was much smaller in the eastern provinces at –0.3 to –0.7 mol O_2 m^{-2} yr^{-1}, where the seasonal amplitude in MLD is lower, as are wind speeds (Table 3.5).

By comparing the physical terms of the O_2 and O_2/Ar budgets, we found that the O_2/Ar budget is less subject to the bias of horizontal advection (Ekman transport) than the O_2 budget (Figures 3.9–3.12 and Table 3.4). This can be explained by the fact that the horizontal surface gradient in O_2, which is strongest meridionally, seems dominated by the temperature effect on solubility. Examining the O_2/Ar budget removes most of this effect due to the highly similar solubilities of the two gases. Because Ekman transport in the North Pacific subarctic and transition zone is strongest in the southward direction due to the westerlies, F_{Ek} is large in the O_2 budget, but much smaller in the O_2/Ar budget.

By measuring O_2/Ar, we shift the physical bias on our measurements during spring, summer and fall from a horizontal plane to a vertical one, limiting the large source of uncertainty due to horizontal advection that has been encountered in other studies of the North Pacific using a single tracer, such as DIC or NO_3, to estimate *NCP*. Wong *et al*. [2002] estimate that horizontal advection introduced an uncertainty of 60–110% in their nitrate-drawdown-based estimates of *NCP* in KURO, OYA, and the subarctic current and Alaska gyre regions. The largest terms in the O_2/Ar physical budget are vertical diffusive mixing and entrainment. They are generally loss terms in fall and winter when the mixed layer is deepening, entraining and mixing water with a respiration signature ($\Delta O_2/Ar < 0$), and negligible in spring and summer when the mixed layer is shoaling. This is an advantage of the O_2/Ar method, as it means there is little summertime bias on our O_2/Ar-based estimates of *NOP*, and we can generally better estimate the O_2/Ar gradient below the mixed layer (e.g., using Argo floats or CTD casts) than the horizontal gradient in O_2/Ar.

Table 3.5: Net annual fluxes of *NOP*, *NCP*, air-sea CO_2 flux and F_{phys} in North Pacific provinces

Positive fluxes contribute positively to mixed layer O_2 (for F_{NOPU}, $F_{physO2/Ar}$, and F_{NOPC}) or *DIC* ($F_{NCP(C)}$, $F_{CO2(in)}$, and $F_{physDIC}$).

Region	F_{NOPU}[a]	$F_{physO2/Ar}$	F_{NOPC}	$F_{NCP(C)}$	$F_{CO2(in)}$[b]	$F_{physDIC}$ (residual)	Ratio $F_{NCP(C)}$: $F_{CO2(in)}$
	(mol O_2 m^{-2} yr^{-1})			(mol C m^{-2} yr^{-1})			
CJ	6.9 ± 1.8	-6.8 ± 3.4	11 ± 5.2	-7.6 ± 3.6	2.1	5.5	-3.6
OYA	10.6 ± 1.7	-2.4 ± 0.8	13.2 ± 2.5	-9.1 ± 1.7	0.7	8.4	-13.0
SAW	5 ± 2.5	-1.7 ± 0.5	7 ± 3.0	-4.8 ± 2.1	0.6	4.2	-8.0
SAE	5.8 ± 1.9	-0.7 ± 0.3	6.5 ± 2.2	-4.5 ± 1.5	1.7	2.8	-2.6
KURO[c]	1.6 ± 0.4	-9 ± 4.4	6.5 ± 4.8	-4.5 ± 3.3	2.7	1.8	-1.7
TZW[c]	0.8 ± 0.2	-3.8 ± 2.3	5.3 ± 2.5	-3.7 ± 1.7	2.5	1.2	-1.5
TZE	3.6 ± 1.0	-0.3 ± 0.3	3.3 ± 1.3	-2.3 ± 0.9	1.4	0.9	-1.6
TZC	3.9 ± 1.6	-0.3 ± 0.3	4.1 ± 1.8	-2.8 ± 1.2	0.4	2.4	-7.1

[a]Percentage error in NOP_U by province: CJAP (26%), OYA (16%), SAW (49%), SAE (33%), EJAP (28%), TZW (25%), TZE (27%), TZC (40%).

[b]$F_{CO2(in)}$ is annual integrated mean sea-air CO_2 flux from climatology of Takahashi *et al*. [2009].

[c]These provinces have no summer cruise data; NCP may be underestimated.

3.4.6 Integrated annual NCP in North Pacific provinces

We integrated our NOP_C values over the year to determine annual *NOP* in each province (in mol O_2 m^{-2} yr^{-1}; Figure 3.8 and Table 3.5). We then divided NOP_C by a photosynthesis quotient of 1.45 to obtain annual *NCP* (in mol C m^{-2} yr^{-1}; Table 3.5). The coastal western boundary provinces, CJ and OYA, had the largest annual *NCP* among the provinces in our study (7.6 ± 3.6 and 9.1 ± 1.7 mol C m^{-2} yr^{-1}, respectively). In OYA, our mean *NCP* estimate is larger but within the ~±50% uncertainty of previous *NCP* estimates there (6.1–6.9 mol C m^{-2} yr^{-1}).

NCP was similar in the subarctic provinces, SAW and SAE, at 4.8 ± 2.1 and 4.5 ± 1.5 mol C m^{-2} yr^{-1}, respectively; Table 3.5). These rates are consistent with previous shipboard observations in the WSG (2.6–6.3 mol C m^{-2} yr^{-1}) but ~1.5–2x larger than those in the AG and eastern subarctic (1.9–3.1 mol C m^{-2} yr^{-1}; Table 3.1). The difference between our estimates and previous shipboard studies in the AG could be explained by the greater spatial resolution of our study, interannual variability, and/or slightly different regional coverage; most previous estimates of *NCP* in the AG are from OSP, and our cruise tracks passed substantially farther south of OSP and densely cover the subarctic front and subarctic current region (~42–45° N; Fig. 1). Wong *et al*. [2002] estimated *NCP* of 2.6 mol C m^{-2} yr^{-1} in this region, which they called the subarctic current province and did not divide longitudinally (~42–45° N, ~160° E–140° W). However, our results indicate that *NCP* in the western and eastern portions of the subarctic (SAW and SAE) may be more similar than results based on comparisons of stations KNOT and OSP suggest [Harrison *et al*., 2004].

In the transition zone, annual *NCP* was greater in the western part of the basin (4.5 ± 3.3 and 3.7 ± 1.7 mol C m^{-2} yr^{-1} in KURO and TZW, respectively) than in the east (2.3 ± 0.9 and 2.8 ± 1.2 mol C m^{-2} yr^{-1} in TZE and TZC, respectively). In KURO, *NCP* is is ~2x larger than

previous estimates in this region (1.9–2.7 mol C m^{-2} yr^{-1} ; Table 3.1) and similar to our *NCP* estimates for the subarctic. We have no summertime data in KURO or TZW, so annual *NCP* in these provinces may be underestimated. In the eastern transition zone, rates were similar to those previously found in this region (2.6–4 mol C m^{-2} yr^{-1}, Table 3.1) and at subtropical station ALOHA (2.7 ± 0.9 mol C m^{-2} yr^{-1}).

3.4.7 Influence of NCP on CO_2 flux

To determine the influence of *NCP* on annual CO_2 flux in the North Pacific provinces, we compared our estimated annual *NCP* with the net annual climatological CO_2 influx, $FCO_{2(in)}$, in each of these regions (Figure 3.13 and Table 3.5). $FCO_{2(in)}$ is calculated as $1/h*k\mathrm{CO_2}*k_\mathrm{H}(p\mathrm{CO_{2atm}} - p\mathrm{CO_{2SW}})$, with positive $FCO_{2(in)}$ defined as into the ocean (note this is the opposite of the sign convention in equation (3.3) and our results). Climatological $FCO_{2(in)}$ was calculated with monthly climatological $\Delta p\mathrm{CO_2}$, wind speed, temperature and salinity data [Takahashi *et al.*, 2009], using k_{CO2} calculated with the parameterization of Ho *et al*. [2006] for consistency with our cruise data. We interpolated monthly values to a daily time step. Our cruise estimates of $FCO_{2(in)}$, which are limited to fall and winter, compare well with this climatology in most provinces, but show greater influx in the western subarctic (OYA and SAW; Figure 3.13).

Climatological integrated annual $FCO_{2(in)}$ is greatest in the western transition zone (KURO and TZW) at 2.5–2.7 mol C m^{-2} yr^{-1} (Figure 3.13 and Table 3.5). In these provinces, $FCO_{2(in)}$ peaks in winter and shifts to near neutral in summer, due to the influence of temperature on the seasonal cycle of $p\mathrm{CO_2}$ [Takahashi *et al.*, 2002; Ayers and Lozier, 2012]. Annual $FCO_{2(in)}$ has intermediate values in the eastern subarctic and transition zone (SAE and TZE; 1.4–1.7 mol C m^{-2} yr^{-1}, Table 3.5), where the seasonal cycle is similar to that in the western transition zone

but with a smaller amplitude. Annual $FCO_{2(in)}$ is lowest in the OYA, SAW, and TZC provinces (0.4–0.7 mol C m^{-2} yr^{-1}, Table 3.5). OYA and SAW have a notably different seasonal cycle than the other North Pacific provinces, with CO_2 efflux in winter due to vertical entrainment and diffusive mixing of *DIC*-rich water, and CO_2 influx in spring and summer due to high rates of *NCP* in these provinces [Figure 3.13; Takahashi *et al*., 2002]. TZC has a similar seasonal cycle to that of other transition zone provinces, but with a much smaller amplitude, leading to low annual CO_2 influx.

To determine the relative influence of *NCP* and physical supply of *DIC* (F_{physDIC}) on the annual CO_2 flux, we calculated F_{physDIC} from a simplified *DIC* budget in the mixed layer:

$$\frac{dDIC}{dt} = FCO_{2\,(in)} + F_{\text{physDIC}} + F_{\text{NCP(C)}} \qquad (3.12)$$

where F_{physDIC} is the physical input of *DIC* due to advection, mixing and entrainment (with supply of *DIC* defined as positive and removal as negative), and $F_{\text{NCP(C)}}$ is the export of carbon due to *NCP* (with respiratory source of *DIC* defined as positive and biological uptake of *DIC* as negative). Assuming net annual $\partial DIC/\partial t = 0$, we used our cruise results of net annual *NCP* and the climatological net annual CO_2 flux in each province to solve for the residual term, F_{physDIC}.

Our estimated annual *DIC* removal by *NCP* exceeds annual *DIC* supply by CO_2 influx in all provinces (Table 3.5). In OYA and SAW, where we estimated high annual *NCP* (4.8–9.1 mol C m^{-2} yr^{-1}), the relatively low annual CO_2 influx (<1 mol C m^{-2} yr^{-1}) implies a high annual contribution of *DIC* from physical processes (~4–8 mol C m^{-2} yr^{-1}; Table 3.5). Several previous studies (see section 3.2.3) have found similar results in the western subarctic, showing that high rates of *NCP* and physical supply of *DIC* nearly balance one another annually, yielding low atmospheric CO_2 influx (*NCP*:CO_2 influx of –5:1, Chierici *et al*., 2006). Although the TZC has a much smaller seasonal amplitude in *NCP* and CO_2 flux, the small net annual CO_2 influx there

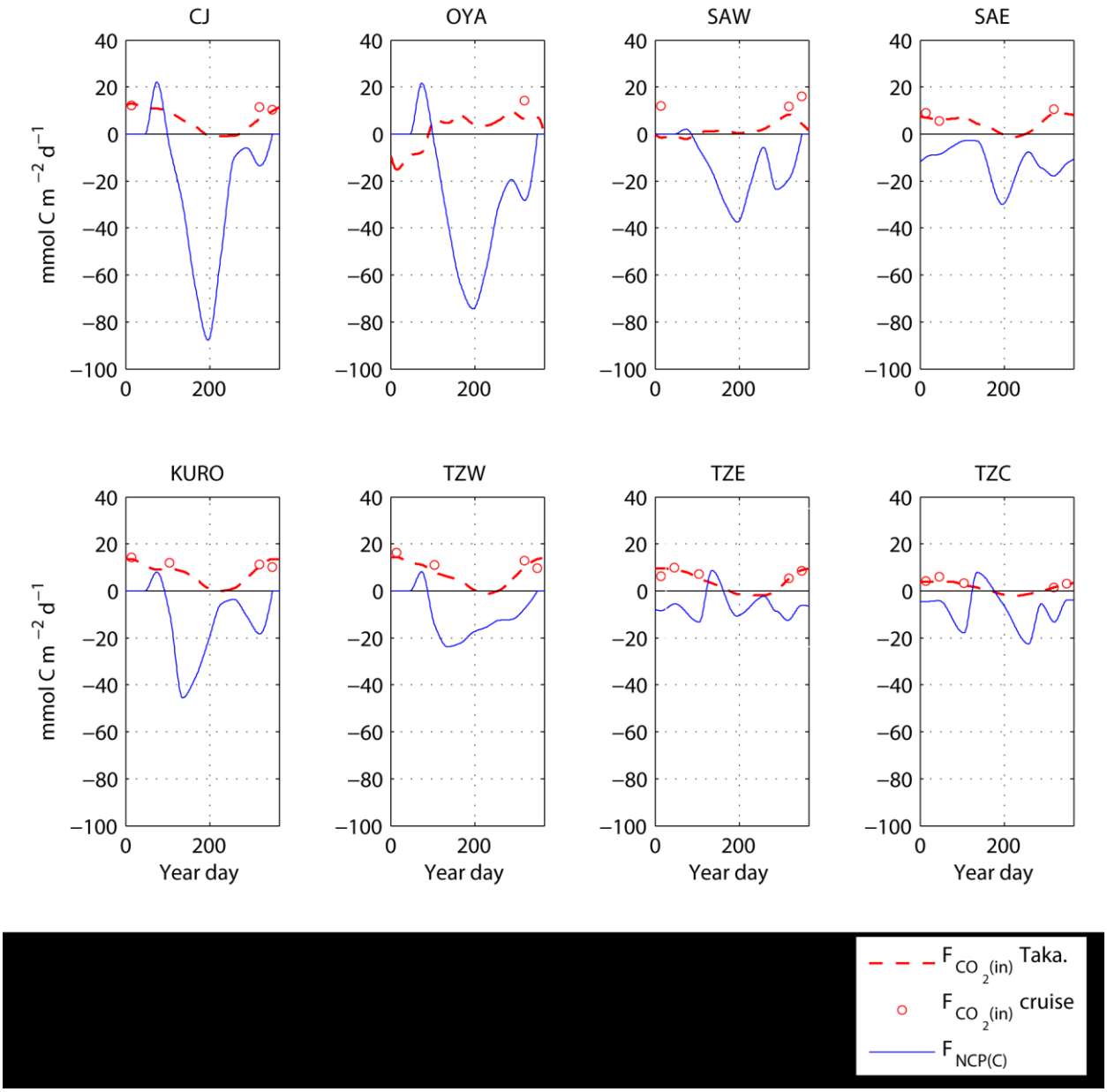

Figure 3.13: Mean annual cycle of climatological $F_{CO2(in)}$ (red dashed line; from Takahashi *et al*. [2009]), cruise-based estimates of $F_{CO2(in)}$ from this study (red circles), and corrected *NCP* (*NCP*$_C$, blue line) from this study in provinces. Units, mmol C m^{-2} d^{-1}.

also implies that *NCP* over the annual cycle is also nearly balanced by supply of $F_{physDIC}$ there.

In contrast, across the open ocean transition zone provinces (KURO, TZW, and TZE) and in the eastern subarctic (SAE), annual *NCP* was ~2–3x the rate of CO_2 influx (1.4–2.6 mol C m^{-2}

yr^{-1}), indicating that the supply of $F_{physDIC}$ offsets only one-third to half of annual *DIC* removal by *NCP* (Table 3.5). This greater imbalance between annual *NCP* and physical supply explains the high annual rates of CO_2 influx in the North Pacific transition zone. A recent *DIC* modeling study [Ayers and Lozier, 2012] found a similar ratio of *NCP*:CO_2 influx:$F_{physDIC}$ (–2:1:1) in the North Pacific transition zone area with highest annual CO_2 uptake (which, as they define it, includes our KURO, TZW, TZE, and SAE provinces). They noted that geostrophic divergence of *DIC* in this region is an annual *DIC* loss term equivalent to that of *NCP*, offsetting some of the *DIC* supply by entrainment and diffusive mixing. Thus the combination of relatively high annual *NCP* and lower $F_{physDIC}$ in the transition zone and eastern subarctic (compared with the western subarctic) may account for its high annual atmospheric CO_2 uptake.

3.4.8 Conclusions

Through continuous, ~4-km-scale measurements of O_2/Ar and pCO_2 on repeat volunteer observation ship crossings, we made basin-scale estimates of *NCP* and CO_2 flux in the North Pacific. These synoptic *NCP* estimates cover a wider spatial extent at greater resolution (~4 km) than any previous shipboard basin-scale estimates in the North Pacific, providing insights into the spatial and seasonal variability of carbon cycling in the basin and putting North Pacific time series studies in a regional context.

Based on our estimates of O_2/Ar-based *NCP* corrected for physical inputs using a climatological O_2/Ar mixed layer budget, we generally found a "west high, east low" pattern across the basin, with the greatest annual *NCP* in the western boundary provinces influenced by the Oyashio and Kuroshio currents (OYA and CJ, 9.1 ± 1.7 and 7.6 ± 3.6 mol C m^{-2} yr^{-1}, respectively) and higher *NCP* in the western transition zone (KURO and TZW, 4.5 ± 3.3 and 3.7

± 1.7 mol C m^{-2} yr^{-1}) than in the eastern transition zone (TZE and TZC, 2.3 ± 0.9 and 2.8 ± 1.2 mol C m^{-2} yr^{-1}). *NCP* had the largest seasonal amplitude in the western North Pacific provinces, with summer regional mean rates of 18–66 mmol C m^{-2} d^{-1} and negligible *NCP* in winter. In contrast, in the eastern transition zone, *NCP* was less seasonally variable and had lower mean rates year-round (5–13 mmol C m^{-2} d^{-1}). However, *NCP* was similar in the subarctic west and east provinces at 4.8 ± 2.1 and 4.5 ± 1.5 mol C m^{-2} yr^{-1}, respectively, in contrast with previous results showing higher NCP in the WSG (mainly based on comparison of data from KNOT and OSP).

In several provinces (OYA, KURO, TZW, and SAE), our *NCP* estimates are 1.5–2x greater than the mean of previous results in the respective regions. This may reflect the ability of our continuous O_2/Ar method to capture intermittent, high-productivity events that could have been missed by previous estimates, most of which are based on discrete snapshots with lower spatial resolution. However, results in the eastern transition zone (TZE and TZC; 2.2 and 2.6 mol C m^{-2} yr^{-1}, respectively), were similar to previous results in these regions and at subtropical station ALOHA (2.7 ± 0.9 mol C m^{-2} yr^{-1})..

We compared our annual *NCP* estimates with climatological net annual air-sea CO_2 flux and determined the residual net annual supply of *DIC* due to physical processes (F_{physDIC}) in each province. In the western subarctic (OYA and SAW) and the eastern coastal transition zone (TZC), removal of *DIC* by *NCP* over the annual cycle is nearly balanced by supply of F_{physDIC} (mainly in winter, most likely due to vertical diffusive mixing and entrainment). The balance of these two processes leads to a relatively small net annual CO_2 influx in these regions (0.4–0.7 mol C m^{-2} yr^{-1}). In contrast, in the transition zone (KURO, TZW, and TZE) and eastern subarctic (SAE), removal of *DIC* by annual *NCP* was 2–3x the rate of supply by F_{physDIC}, leading to

substantial CO_2 influx (1.4–2.6 mol C m^{-2} yr^{-1}). These results support the recent conclusion by Ayers and Lozier [2012] that the high CO_2 uptake in the North Pacific transition zone is controlled by a combination of high biological uptake and lower net physical supply of *DIC* than that in the subarctic. In conclusion, both biological uptake and physical supply of *DIC* exert significant control on annual atmospheric CO_2 uptake in the North Pacific. Therefore, to predict ocean feedbacks on future climate change, both biological and physical ocean dynamics must be accurately understood and modeled.

BIBLIOGRAPHY

Anderson, L.A. and Sarmiento, J.L. (1994) Redfield ratios of remineralization determined by nutrient data analysis. Global Biogeochemical Cycles, 8, 65-80, 1994.

Andreev, A. et al. Vertical fluxes of nutrients and carbon through the halocline in the western subarctic Gyre calculated by mass balance. Deep-Sea Research II 49 (2002) 5577–5593.

Ayers, J.M. and M.S. Lozier (2012). Unraveling dynamical controls on the North Pacific carbon sink. J. Geophys. Res., 117, C01017, doi:10.1029/2011JC007368.

Ayers, J.M., and M.S. Lozier (2010), Physical controls on the seasonal migration of the North Pacific transition zone chlorophyll front, J. Geophys. Res., 115, C05001, doi:10.1029/2009JC005596.

Behrenfeld, M.J., and Falkowski, P.G. (1997) Photosynthetic rates derived from satellite-based chlorophyll concentration. Limnol. and Oceanogr. 42, 1–20.

Behrenfeld, M.J., et al. (2005) Carbon-based ocean productivity and phytoplankton physiology from space. Glob. Biogeochem. Cycles 19, GB1006. doi:10.1029/2004GB002299.

Benitez-Nelson, C. et al. (2001), A time-series study of particulate matter export in the North Pacific Subtropical Gyre based on ^{234}Th : ^{238}U disequilibrium, Deep-Sea Res. I, 48, 2595–2611.

Berelson, W.M. 2001, The flux of particulate organic matter into the Ocean Interior: A

Comparison of Four U.S. JGOFS Regional Studies. Oceanography 14, 59-67.

Bograd. S.J. et al. (2004), On the seasonal and interannual migrations of the transition zone chlorophyll front. Geophys. Res. Lett., 31, L17204, doi:10.1029/2004GL020637.

Bopp, L. et al. (2001) Potential impact of climate change on marine export production. Glob Biogeochem Cyc, 15, 81-99.

Boyd, P.W. and T.W. Trull (2007), Understanding the export of biogenic particles in oceanic waters: Is there consensus?, Prog. in Oceanogr., 72, 276–312.

Boyd, P.W. et al. (1996), In vitro iron enrichment experiments in the NE subarctic Pacific, Mar. Ecol. Prog. Ser., 136, 179–193.

Boyd. P.W. et al. (2004), The decline and fate of an iron-induced subarctic phytoplankton bloom, Nature, 428, 549–553.

Broecker, W.S. and T.-H. Peng, Tracers in the Sea, Lamont-Doherty Geological Observatory (1982).

Carr, M.E. et al. A comparison of global estimates of marine primary production from ocean color. Deep-Sea Research II 53 (2006) 741–770.

Cassar, N. et al. (2009), Continuous high-frequency dissolved O_2/Ar measurements by equilibrator inlet mass spectrometry, Anal. Chem., 81, 1855–1864.

Cassar, N. et al. (2011), The influence of iron and light on net community production in the subantarctic and polar frontal zones. Biogeosciences, 8, 227–237.

Chai, F. et al. (2003) Interdecadal Variation of the Transition Zone Chlorophyll Front: A Physical-Biological Model Simulation between 1960 and 1990. Journal of Oceanography 59, 461-475.

Charette, M.A., S.B. Moran and J.K.B. Bishop (1999), ^{234}Th as a tracer of particulate organic carbon export in the subarctic northeast Pacific Ocean, Deep-Sea Res. II, 46, 2833–2861.

Chavez, F.P. et al. Marine Primary Production in Relation to Climate Variability and Change. Annu. Rev. Marine. Sci. 2011.3:227-260.

Chierici, M., A. Fransson, and Y. Nojiri (2006), Biogeochemical processes as drivers of surface fCO2 in contrasting provinces in the subarctic North Pacific Ocean, Global Biogeochem. Cycles 20, GB1009, doi:10.1029/2004GB002356.
Craig, H. and T. Hayward (1987), Oxygen supersaturation in the ocean: biological versus physical contributions. Science, 235(4785), 199–202.
Cronin, M.F. *et al*. Formation and erosion of the seasonal thermocline in the Kuroshio Extension Recirculation Gyre. Deep-Sea Research II 85 (2013) 62–74.
de Boyer Montégut, C., G. Madec, A. S. Fischer, A. Lazar, and D. Iudicone (2004), Mixed layer depth over the global ocean: an examination of profile data and a profile-based climatology, J. Geophys. Res., 109, C12003. doi:10.1029/2004JC002378.
de Boyer Montégut, C., J. Mignot, A. Lazar, and S. Cravatte (2007), Control of salinity on the mixed layer depth in the world ocean: 1. General description, J. Geophys. Res., 112, C06011. doi:10.1029/2006JC003953.
Denman, K.L. and A.E. Gargett (1995), Biological-physical interactions in the upper ocean: the role of vertical and small scale transport processes. Annu. Rev. Fluid Mech., 27, 225–255.
Doney, S.C. 2006, Plankton in a warmer world. Nature 444, 695-696.
Doney, S.C., V.J. Fabry, R.A. Feely, and J.A. Kleypas (2009), Ocean Acidification: The Other CO_2 Problem. Annu. Rev. Marine. Sci. 1:169-192.
Doney, S.C. et al. (2009a), Surface-ocean CO_2 variability and vulnerability. Deep-Sea Research II 56, 504–511.
Dore, J.E. et al. (2003) Climate-driven changes to the atmospheric CO_2 sink in the subtropical North Pacific Ocean. Nature 424, 754–757.
Duce, R.A. and Tindale, N.W. (1991) Atmospheric transport of iron and its deposition in the ocean. Limnol. Oceanogr., 36, 715-1726.
Ducklow, H.W. et al. Upper Ocean Carbon Export and the Biological Pump. Oceanography, 14, 50-58, 2001.
Dunne, J. P., R. A. Armstrong, A. Gnanadesikan, and J. L. Sarmiento (2005), Empirical and mechanistic models for the particle export ratio, Global Biogeochem. Cycles, 19, GB4026, doi:10.1029/2004GB002390.
Elskens, M. et al. (2008) Primary, new and export production in the NW Pacific subarctic gyre during the vertigo K2 experiments. Deep-Sea Research II 55, 1594– 1604.
Emerson, S. (1987), Seasonal oxygen cycles and biological new production in surface waters of the subarctic Pacific ocean, J. Geophys. Res., 92, 6535–6544.
Emerson, S. and C. Stump (2010), Net biological oxygen production in the ocean—II: Remote in situ measurements of O_2 and N_2 in subarctic Pacific surface waters, Deep-Sea Res. I, 57 1255–1265.
Emerson, S. et al. (1991), O_2, Ar, N_2, and Rn in surface waters of the subarctic ocean: net biological O_2 production, Glob. Biogeochem. Cycles, 5, 49–69.
Emerson, S. et al. (1995), Chemical tracers of productivity and respiration in the subtropical Pacific Ocean, J. Geophys. Res. 100, 15,873–15,887.
Emerson, S. et al. (1997), Experimental determination of the organic carbon flux from open-ocean surface waters, Nature 389, 951–954.
Emerson, S., C. Stump, and D. Nicholson (2008), Net biological oxygen production in the ocean: Remote in situ measurements of O_2 and N_2 in surface waters, Glob. Biogeochem. Cycles, 22, GB3023, doi:10.1029/2007GB003095.

Emerson, S.R. and J.I. Hedges (2008). Chemical Oceanography and the Marine Carbon Cycle, Cambridge Univ. Press, p. 375.
Eppley, R.W. and Peterson, B.J. (1979). Particulate organic matter flux and planktonic new production in the deep ocean. Nature 282, 677-680.
Falkowski, P.G. et al. Biogeochemical Controls and Feedbacks on Ocean Primary Production (1998) Science 281, 200-206.
Fabry, V.J. *et al.* (2008) Impacts of ocean acidification on marine fauna and ecosystem processes. *ICES J. Marine Sci.* 65, 414–432.
Feely, R.A. et al. (1998), A new automated underway system for making high precision pCO_2 measurements onboard research ships, Analytica Chim. Acta, 377, 185–191.
Feely, R.A. et al. (2004). Oxygen Utilization and Organic Carbon Remineralization in the Upper Water Column of the Pacific Ocean. Journal of Oceanography, Vol. 60, pp. 45 to 52.
Feely, R. *et al.* (2008) Evidence for upwelling of corrosive "acidified" water onto the continental shelf. *Science* 320, 1490-1492.
Franks, P.J.S. (1992), Sink or swim: accumulation of biomass at fronts, Mar. Ecol. Prog. Ser., 82, 1–12.
Garcia, H. E., R. A. Locarnini, T. P. Boyer, J. I. Antonov, O. K. Baranova, M. M. Zweng, and D. R. Johnson, 2010. World Ocean Atlas 2009, Volume 3: Dissolved Oxygen, Apparent Oxygen Utilization, and Oxygen Saturation. S. Levitus, Ed. NOAA Atlas NESDIS 70, U.S. Government Printing Office, Washington, D.C., 344 pp.
Garcia, H.E. and L.I. Gordon (1992), Oxygen solubility in seawater: Better fitting equations, Limnol. Oceanogr., 37, 1307–1312.
Glover, D.M. et al. (1994) Dynamics of the transition zone in coastal zone color scanner-sensed ocean color in the North Pacific during oceanographic spring. Journal of Geophysical Research 99, 7501-7511.
Goes, J.I. et al. (2004) The influence of large-scale environmental changes on carbon export in the North Pacific Ocean using satellite and shipboard data. Deep-Sea Research II 51, 247–279.
Goes, J.I. et al. (2004a) A Comparison of the Seasonality and Interannual Variability of Phytoplankton Biomass and Production in the Western and Eastern Gyres of the Subarctic Pacific Using Multi-Sensor Satellite Data. Journal of Oceanography, Vol. 60, pp. 75 to 91.
Gueguen, C. and P. Tortell (2008), High-resolution measurement of Southern Ocean CO_2 and O_2/Ar by membrane inlet mass spectrometry, Mar. Chem., 108, 184–194.
Hamme, R. and S. Emerson (2004), The solubility of neon, nitrogen and argon in distilled water and seawater, Deep-Sea Res. I, 51(11), 1517–1528.
Hamme, R. and S. Emerson (2006), Constraining bubble dynamics and mixing with dissolved gases: Implications for productivity measurements by oxygen mass balance, J. Mar. Res., 64, 73–95.
Hamme, R.C. et al. (2010), Volcanic ash fuels anomalous plankton bloom in subarctic northeast Pacific. Geophys. Res. Lett., 37, L19604, doi:10.1029/2010GL044629.
Harada, K. and Shibamoto, Y. (2002), Export fluxes of organic carbon in the Western North Pacific determined by drifting sediment trap experiments and 234Th profiles. in Fernandez J.M. (ed.), Fichez Renaud (ed.)., Environmental Changes and Radioactive Tracers, pp. 449-458.
Harrison, P. J., F.A. Whitney, A. Tsuda, H. Saito and K. Tadokoro (2004), Nutrient and plankton dynamics in the NE and NW gyres of the Subarctic Pacific Ocean, J. Ocean., 60, 93–117.

Harrison, P.J., P.W. Boyd, D.E. Varela, S. Takeda, A. Shiomoto and T. Odate (1999), Comparison of factors controlling phytoplankton productivity in the NE and NW subarctic Pacific gyres, Progr. Oceanogr., 43, 205–234.

Henson, S.A. et al. Detection of anthropogenic climate change in satellite records of ocean chlorophyll and productivity. Biogeosciences, 7, 621–640, 2010.

Ho, D. T., C. S. Law, M. J. Smith, P. Schlosser, M. Harvey, and P. Hill (2006), Measurements of air-sea gas exchange at high wind speeds in the Southern Ocean: Implications for global parameterizations, Geophys. Res. Lett., 33, L16611, doi:10.1029/2006GL026817.

Ho, D.T., R. Wanninkhof, P. Schlosser, D.S. Ullman, D. Hebert and K.F. Sullivan (2011), Toward a universal relationship between wind speed and gas exchange: Gas transfer velocities measured with $^3He/SF_6$ during the Southern Ocean Gas Exchange Experiment. J. Geophys. Res., 116, C00F04, doi:10.1029/2010JC006854.

Honda, M. (2003). Biological Pump in Northwestern North Pacific. Journal of Oceanography, Vol. 59, pp. 671 to 684, 2003.

Honda, M. et al. (2002). The biological pump in the northwestern North Pacific based on fluxes and major components of particulate matter obtained by sediment-trap experiments (1997 2000). Deep Sea Research Part II: Topical Studies in Oceanography, vol. 49, issue 24-25, pp. 5595-5625.

Hosoda, S. et al. (2010) Improved Description of Global Mixed-Layer Depth Using Argo Profiling Floats. Journal of Oceanography, Vol. 66, pp. 773 to 787.

Howard, E., S. Emerson, S. Bushinsky and C. Stump (2010), The role of net community production in air–sea carbon fluxes at the North Pacific subarctic–subtropical boundary region, Limnol. Oceanogr., 55(6), 2585–2596.

Imai, K. et al. (2002) Time series of seasonal variation of primary productivity at station KNOT (44 N, 155 E) in the sub-arctic western North Pacific. Deep-Sea Research II 49 5395–5408.

Isada, T. et al. (2009). Photosynthetic features and primary productivity of phytoplankton in the Oyashio and Kuroshio–Oyashio transition regions of the northwest Pacific. Journal of Plankton Research 31 1009–1025.

Juranek, L.W. "Assessment of Pacific Ocean Organic Carbon Production and Export Using Measurements of Dissolved Oxygen Isotopes and Oxygen/Argon Gas Ratios" (PhD dissertation, University of Washington, 2007).

Juranek, L.W. and P.D. Quay (2005), In vitro and in situ gross primary and net community production rates in the N. Pacific subtropical gyre using labeled and natural abundance isotopes of oxygen, Glob. Biogeochem. Cycles, 19, 10.1029/2004GB002384.

Juranek, L.W. and P.D. Quay (2005), In vitro and in situ gross primary and net community production rates in the N. Pacific subtropical gyre using labeled and natural abundance isotopes of oxygen, Glob. Biogeochem. Cycles, 19, 10.1029/2004GB002384.

Juranek, L.W. et al. (2012), Biological production in the NE Pacific and its influence on air-sea CO_2 flux: evidence from dissolved oxygen isotopes and O_2/Ar. J. Geophys. Res., 117, C05022, doi:10.1029/2011JC007450.

Kaiser, J. et al. (2005), Marine productivity estimates from continuous O_2/Ar ratio measurements by membrane inlet mass spectrometry. Geophys. Res. Lett. 32, L19605, doi:10.1029/2005GL023459.

Karl, D. et al. (1997), The role of nitrogen fixation in biogeochemical cycling in the subtropical North Pacific Ocean, Nature, 388, 533–538.

Karl, D., R.R. Bidigare and R.M. Letelier (2001), Long-term changes in plankton community structure and productivity in the North Pacific Subtropical Gyre: The domain shift hypothesis, Deep-Sea Res. II, 48, 1449–1470.
Karl, D.M. (1999), A sea of change: biogeochemical variability in the North Pacific Subtropical Gyre. Ecosystems, 2, 181–214.
Karl, D.M. et al. (2003) Temporal studies of biogeochemical processes determined from ocean time series observations during the JGOFS era. Ch. 10. p. 242–243 in Ocean Biogeochemistry. ed Fasham, M.J.R. Springer.
Kawakami, H. and Honda, M.C. (2007) Time-series observation of POC fluxes estimated from 234Th in the northwestern North Pacific. Deep-Sea Research I 54, 1070–1090.
Kawakami, H. et al. (2004). Particulate organic carbon fluxes estimated from 234Th deficiency in winters and springs in the northwestern North Pacific. Geochemical Journal, Vol. 38, pp. 581 to 592.
Kawakami, H. et al. (2007) Time-Series Observation of Dissolved Inorganic Carbon and Nutrients in the Northwestern North Pacific. Journal of Oceanography, Vol. 63, pp. 967 to 982.
Kawakami, H. et al. East-West Distribution of Nutrients and Dissolved Inorganic Carbon in the Northern North Pacific in Autumn. The Open Oceanography Journal, 2010, 4, 99-106.
Keeling, C.D., H. Brix, and N. Gruber (2004), Seasonal and long-term dynamics of the upper ocean carbon cycle at Station ALOHA near Hawaii, Global Biogeochem. Cycles, 18, GB4006, doi:10.1029/2004GB002227.
Khatiwala et al., 2009. Reconstruction of the history of anthropogenic CO_2 concentrations in the ocean. 462, 346-350, doi:10.1038/nature08526.
Körtzinger, A., U. Send, R.S. Lampitt, S. Hartman, D.W.R. Wallace, J. Karstensen, M.G. Villagarcia, O. Llinás, and M.D. DeGrandpre (2008). The seasonal pCO_2 cycle at 49_N/16.5_W in the northeastern Atlantic Ocean and what it tells us about biological productivity. J. Geophys. Res., 113, C04020, doi:10.1029/2007JC004347.
Kusakabe, M. et al. (2002) Effects of the Anticyclonic Eddies on Water Masses, Chemical Parameters and Chlorophyll Distributions in the Oyashio Current Region. Journal of Oceanography, Vol. 58, pp. 691 to 701.
Langmann, B., K. Zaksek, M. Hort, and S. Duggen (2010), Volcanic ash as fertiliser for the surface ocean. Atmos. Chem. Phys., 10, 3891–3899.
Laws, E.A. (1991). Photosynthetic quotients, new production and net community production in the open ocean. Deep Sea Res., 38, 143–167.
Laws, E.A., Paul G. Falkowski, Walker O. Smith Jr., Hugh Ducklow, James J. McCarthy (2000). Temperature effects on export production in the open ocean. Global Biogeochemical Cycles 14, 1231-1246.
Laws, E.A. et al., 2011, Simple equations to estimate ratios of new or export production to total production from satellite-derived estimates of sea surface temperature and primary production. Limnol. Oceanogr.: Methods 9, 593-601.
Lee, K. (2001), Global net community production estimated from the annual cycle of surface water total dissolved inorganic carbon, Limnol. Oceanogr., 46, 1287–1297.
Lee, K. et al. (2006), Global relationships of total alkalinity with salinity and temperature in surface waters of the world's oceans, Geophys. Res. Lett., 33, L19605, doi:10.1029/2006GL027207.

Leonard, C., R.R. Bidigare, M.P. Seki and J.J. Polovina (2001), Interannual mesoscale physical and biological variability in the North Pacific Central Gyre, Prog. Oceanogr., 49, 227–244.
Lewis, E., and D.W.R. Wallace (1998), Program developed for CO_2 system calculations, ORNL/CDIAC-105, 21 pp., Carbon Dioxide Inf. Anal. Cent., Oak Ridge Natl. Lab., Oak Ridge, Tenn.
Liu, H. et al. (2004) Community Structure and Dynamics of Phytoplankton in the Western Subarctic Pacific Ocean: A Synthesis. Journal of Oceanography, Vol. 60, pp. 119 to 137, 2004.
Lockwood, D., P. D. Quay, M. T. Kavanaugh, L. W. Juranek, and R. A. Feely (2012), High-resolution estimates of net community production and air-sea CO2 flux in the northeast Pacific, Global Biogeochem. Cycles, 26, GB4010, doi:10.1029/2012GB004380.
Longhurst, A. Ecological Geography of the Sea (2007) Academic Press.
Louanchi, F. and Najjar, R.G. (2000) A global monthly climatology of phosphate, nitrate, and silicate in the upper ocean: Spring-summer export production and shallow remineralization. Global Biogeochemical Cycles, 14, 957-977.
Mann, K.H. and Lazier, J.R.N. (2006), Dynamics of Marine Systems: Biological-Physical Interactions in the Oceans 3rd ed. Blackwell.
McClain, C.R. 2009, A Decade of Satellite Ocean Color Observations. Annu. Rev. Marine. Sci., 1:19-42.
McKinley, G. A., et al. (2006), North Pacific carbon cycle response to climate variability on seasonal to decadal timescales, J. Geophys. Res., 111, C07S06, doi:10.1029/2005JC003173.
Midorikawa, T. et al. Estimation of seasonal net community production and air–sea CO2 flux based on the carbon budget above the temperature minimum layer in the western subarctic North Pacific. Deep-Sea Research I 49 (2002) 339–362.
Midorikawa, T. et al. Seasonal Changes in Oceanic pCO2 in the Oyashio Region from Winter to Spring. Journal of Oceanography, Vol. 59, pp. 871 to 882, 2003.
Mignot, J., C. de Boyer Montégut, A. Lazar, and S. Cravatte (2007), Control of salinity on the mixed layer depth in the world ocean: 2. Tropical areas, J. Geophys. Res., 112, C10010. doi:10.1029/2006JC003954.
Monterey, G. and Levitus, S. (1997), Seasonal Variability of Mixed Layer Depth for the World Ocean. NOAA Atlas NESDIS 14, U.S. Gov. Printing Office, Wash., D.C., 96 pp. 87 figs.
Najjar, R.G. and Keeling, R.F. Mean annual cycle of the air-sea oxygen flux: A global view. Global Biogeochemical Cycles 14, 573-584, 2000.
Nemcek, N., Ianson, D. and Tortell, P.D. (2008), A high-resolution survey of DMS, CO2, and O2/Ar distributions in productive coastal waters. Glob. Biogeochem. Cycles, 22, GB2009, doi:10.1029/2006GB002879.
Nightingale, P.D., G. Malin, C.S. Law, A.J. Watson, P.S. Liss, M.I. Liddicoat, J. Boutin, and R.C. Upstill-Goddard (2000), In situ evaluation of air-sea exchange parameterizations using novel conservative and volatile tracers. Global Biogeochem. Cycles, 14(1), 373–387.
Ohno, Y. et al. (2009) Mixed Layer Depth Climatology of the North Pacific Based on Argo Observations. Journal of Oceanography, Vol. 65, pp. 1 to 16, 2009.
Olson, D.B. et al. (1994), Life on the edge: marine life and fronts, Oceanography 7(2), 52–60.
Passow, U. and Carlson, C.A. (2012), The biological pump in a high CO_2 world. Mar Ecol Prog Ser. Vol. 470: 249–271.

Pierrot, D. et al. (2009), Recommendations for autonomous underway pCO_2 measuring systems and data-reduction routines, Deep-Sea Res. II, 56, 512–522.
Polovina, J.J. et al. (2001), The transition zone chlorophyll front, a dynamic global feature defining migration and forage habitat for marine resources, Progr. in Oceanogr. 49, 469–483.
Quay, P. D., J. Stutsman, R.A. Feely, and L.W. Juranek (2009), Net community production rates across the subtropical and equatorial Pacific Ocean estimated from air-sea $\delta^{13}C$ disequilibrium, Global Biogeochem. Cycles, 23, GB2006, doi:10.1029/2008GB003193.
Quay, P.D. and Stutsman, J. (2003), Surface layer carbon budget for the subtropical N. Pacific: $\delta^{13}C$ constraints at station ALOHA, Deep-Sea Res. I, 50, 1045–1061.
Quay, P.D., C. Peacock, K. Björkman and D.M. Karl (2010), Measuring primary production rates in the ocean: Enigmatic results between incubation and nonincubation methods at Station ALOHA, Glob. Biogeochem. Cycles, 24, doi:10.1029/2009GB003665.
Raven, J.A. and P.G. Falkowski (1999), Oceanic sinks for atmospheric CO_2. Plant, Cell and Environment 22, 741–755.
Reuer, M.K. et al. (2007), New estimates of Southern Ocean biological production rates from O_2/Ar ratios and the triple isotope composition of O_2, Deep-Sea Res. I, 54, 951–974.
Risien, C.M., and D.B. Chelton, 2008: A Global Climatology of Surface Wind and Wind Stress Fields from Eight Years of QuikSCAT Scatterometer Data. J. Phys. Oceanogr., 38, 2379-2413.
Roden, G.I. Subarctic-subtropical transition zone of the North Pacific: large-scale aspects and mesoscale structure. pp 1–38. In Biology, Oceanography, and Fisheries of the North Pacific Transition Zone and Subarctic Frontal Zone, NOAA Technical Report NMFS 105 December 1991, ed. J.A. Wetherall.
Sabine, C.L. et al. The Oceanic Sink for Anthropogenic CO_2. *Science* 305, 367 (2004).
Sasai, Y. and Ikeda, M. A model study for the carbon cycle in the upper layer of the North Pacific. Marine Chemistry 81 (2003) 71– 88.
Schlitzer, R. (2000), Applying the adjoint method for global biogeochemical modeling: export of particulate organic matter in the world ocean. In: Kasibhatla, P., Heimann, M., Hartley, D., Mahowald, N., Prinn., R., Raynor, P. (Eds.), Inverse Methods in Global Biogeochemical Cycles. AGU Geophysical Monograph Series, Washington, DC, pp. 107–124.
Schlitzer, R. (2004), Export production in the equatorial and north Pacific derived from dissolved oxygen, nutrient and carbon data, J. Oceanography, 60, 53–62.
Stanley, R. H. R., W. J. Jenkins, D. E. Lott III, and S. C. Doney (2009), Noble gas constraints on air-sea gas exchange and bubble fluxes, J. Geophys. Res., 114, C11020, doi:10.1029/2009JC005396.
Stanley, R.H.R., J.B. Kirkpatrick, N. Cassar, B.A. Barnett and M.B. Bender (2010), Net community production and gross primary production rates in the western equatorial Pacific, Global Biogeochem. Cycles, 24, GB4001, doi:10.1029/2009GB003651.
Strass, V.H. (1992), Chlorophyll patchiness caused by mesoscale upwelling at fronts, Deep-Sea Research, 39(1), 75–96.
Strickland, J.D.H. and T. R. Parsons (1972), A practical handbook of seawater analysis. Second Edition, Bulletin 167. Fisheries Research Board of Canada, Ottawa.
Stumm, W. and Morgan, J.J. Aquatic Chemistry, 3rd edn. (Wiley, 1996).

Sugiura, K. and Tsunogai, S. (2005) Spatial and Temporal Variation of Surface xCO2 Providing Net Biological Productivities in the Western North Pacific in June Journal of Oceanography, Vol. 61, pp. 435 to 445.
Suzuki, K. et al. (2002) East-West Gradients in the Photosynthetic Potential of Phytoplankton and Iron Concentration in the Subarctic Pacific Ocean during Early Summer. Limnology and Oceanography, Vol. 47, No. 6 (Nov., 2002), pp. 1581-1594.
Sweeney, C., E. Gloor, A.R. Jacobson, R.M. Key, G. McKinley, J.L. Sarmiento, and R. Wanninkhof (2007), Constraining global air-sea gas exchange for CO_2 with recent bomb 14C measurements, Global Biogeochem. Cycles, 21, GB2015, doi:10.1029/2006GB002784.
Takahashi, T. et al. (2002), Global sea-air CO_2 flux based on climatological surface ocean pCO_2, and seasonal biological and temperature effects, Deep-Sea Res. II, 49, 1601–1622.
Takahashi, T. et al. (2009), Climatological mean and decadal change in surface ocean pCO_2, and net sea–air CO_2 flux over the global oceans, Deep-Sea Res. II, 56, 554–577.
Tortell, P.D. (2005), Dissolved gas measurements in oceanic waters made by membrane inlet mass spectrometry, Limnol. Oceanogr. Methods, 3, 24–37.
Tsuda, A., H. Kasai and H. Saito (2002): Seasonal variability of nutrients, chlorophyll and new production in the Oyashio time-series observation. In Extended Abstract of Oceanographic Society of Japan 2002 Spring Meeting, p. 350 (in Japanese).
Tsurushima, N. et al. Seasonal variations of carbon dioxide system and nutrients in the surface mixed layer at station KNOT (44º N, 155º E) in the subarctic western North Pacific. Deep-Sea Research II 49 (2002) 5377–5394.
UNESCO (1994), Protocols for the Joint Global Ocean Flux Study (JGOFS) Core Measurements IOC Manual and Guides 29.
Wannninkhof, R. (1992), Relationship between wind speed and gas exchange over the ocean. J. Geophys. Res. 97, 7373–7382.
Westberry, T. K., P. J. le. B. Williams, and M. J. Behrenfeld (2012), Global net community production and the putative net heterotrophy of the oligotrophic oceans, Global Biogeochem. Cycles, 26, GB4019, doi:10.1029/2011GB004094.
Westberry, T.K. et al. 2008. Carbon-based primary productivity modeling with vertically resolved photophysiology. Glob. Biogeochem. Cycles 22, GB2024. doi:10.1029/2007GB003078.
Wheeler, P.A. (1993), New production in the subarctic Pacific Ocean: Net changes in nitrate concentrations, rates of nitrate assimilation and accumulation of particulate nitrogen. Prog. Oceanog., 32, 137–161.
Wilson, C. (2003), Late summer chlorophyll blooms in the oligotrophic North Pacific Subtropical Gyre, Geophys. Res. Lett., 30, doi:10.1029/2003GL017770.
Wilson, C. et al. (2008), Biological and physical forcings of late summer chlorophyll blooms at 30°N in the oligotrophic Pacific, J. Mar. Syst. 69, 164–176.
Wong, C.S. et al. (2002), Seasonal cycles of nutrients and dissolved inorganic carbon at high and mid latitudes in the North Pacific Ocean during the Skaugran cruises: determination of new production and nutrient uptake ratios. Deep-Sea Res. II, 49, 5317–5338.
Wong, C.S. et al. (2002a), Time-series study of the biogeochemistry of the North East subarctic Pacific: reconciliation of the Corg/N remineralization and uptake ratios with the Redfield ratios, Deep-Sea Res. II, 49, 5717–5738.

Yao, X. and Schlitzer, R. 2013, Assimilating water column and satellite data for marine export production estimation. Geosci. Model Dev. Discuss., 6, 2045–2085.
Yasuda, I. (2003) Hydrographic Structure and Variability in the Kuroshio-Oyashio Transition Area. Journal of Oceanography, Vol. 59, pp. 389 to 402.
Yoo, S. et al. (2008) Seasonal, interannual and event scale variation in North Pacific ecosystems. Progress in Oceanography 77, 155–181.
Yuan, X. and Talley, L.D. (1996), Characteristics of frontal structure from climatological data and synoptic surveys, J. Geophys. Res., 101, 16491–16508.